University of Alberta

A Fundamental Study of Bubble-Particle Interactions through
Zeta-Potential Distribution Analysis

by

Chendi Wu

A thesis submitted to the Faculty of Graduate Studies and Research
in partial fulfillment of the requirements for the degree of

Master of Science

in

Chemical Engineering

Department of Chemical and Materials Engineering

EXAMINING COMMITTEE

Zhenghe Xu, Chemical and Materials Engineering

Qingxia Liu, Chemical and Materials Engineering

Jozef Szymanski, Civil and Environmental Engineering

TO MY PARENTS AND MY SISTER

ABSTRACT

Understanding the mechanism of bubble-particle interactions plays a critical role in advancing flotation technology. In this study, submicron size bubbles with an average diameter less than 1 μm and a life time of at least several hours were generated using a novel hydrodynamic cavitation method. Effect of mechanical force and water chemistry on generation and stability of submicron size bubbles is investigated.

With recent development in measuring zeta potential distributions of colloidal systems, interactions of bubbles and fine solid particles in various electrolyte, surfactant and frother solutions as well as in industrial process water were studied using the stable submicron size bubbles generated by hydrodynamic cavitation. The outcome of this study provides not only a better understanding of bubble-particle attachment mechanism and its role in flotation, but also a direct evidence of armour-coating of bubbles and enhanced bubble-particle interactions by *in situ* gas nucleation.

ACKNOWLEDGEMENT

Finally, I am forever grateful for the everlasting love of my parents and my sister. Their trust and confidence in me are my greatest impetus in everything I do.

TABLE OF CONTENTS

LIST OF TABLES

LIST OF FIGURES

NOMENCLATURE

ABBREVIATIONS

AFM	Atomic force microscopy
CCC, ccc	Critical coalescence concentration
CCD	Closed circuit display
CF	Centrifuged fines
CMC, cmc	Critical micelle concentration
DAH	Dodecylamine hydrochloride
DF250	Dowfroth 250
DLS	Dynamic light scattering
DLVO Theory	Derjaguin-Landau-Verwey-Overbeek Theory
ELS	Electrophoretic light scattering
FF	Froth fines
FPW	Filtered process water
HIA	High intensity agitation
HWEP	Hot water extraction process
IEP, iep	Isoelectric point
kcps	Kilo counts per second
LB Technique	Langmuir – Blodgett Technique
MIBC	Methyl isobutyl carbinol
OCWE	OSLO cold water extraction
PALS	Phase analysis light scattering
PCS	Photon correlation spectroscopy

ppm	Parts per million
PZC, pzc	Point of zero charge
SDS	Sodium dodecyl sulphate
SFA	Surface force apparatus
SF	Settled fines
XDLVO Theory	Extended Derjaguin-Landau-Verwey-Overbeek Theory

SYMBOLS

A	Hamaker constant, J
a	Particle radius, m
A_{131}	Hamaker constant of two identical phases 1 through a medium 3, J
A_{132}	Hamaker constant of phase 1 and phase 2 through a medium 3, J
C	Electrolyte concentration, M
$d(H)$	Hydrodynamic diameter of the particle, m
D	Diffusion coefficient, $m^2\ s^{-1}$
e	Elementary electron charge, 1.602×10^{-19} C
E	Interaction energy, J
E_∞	Interaction energy in bulk solution, J
F_A	London – Van der Waals force, N
F_E	Electrostatic double layer force, N
F_H	Hydrophobic force, N
F_{HD}	Hydration force, N
F_S	Steric force, N
F_T	Total force, N

h	Separation distance between two surfaces, m
k_B	Boltzmann's constant, 1.38×10^{-23} J K^{-1}
K_{HD}	Hydration force constant, N m^{-1}
K_H	Hydrophobic force constant, J
K_{131}	Hydrophobic force constant of two identical phases 1 in a medium 3, J
K_{132}	Hydrophobic force constant of phase 1 and phase 2 in a medium 3, J
K^*	Hydrophobic force constant in water, N m^{-1}
L	Macromolecular layer thickness, m
M	Mass, kg
n	Refractive index
n_i	Number density of ions i in the solution, m^{-3}
$n_i(\infty)$	Number density of ions i in the bulk solution, m^{-3}
N	Number of particles in the solution
N_B	Number of monomer units per chain
P	Local pressure, N m^{-2} or Pa
R	Particle radius, m
s	Average spacing between two grafted points of the molecules, m
T	Absolute temperature, K
U	Fluid flow velocity, m s^{-1}
V	Volume, m^3
V_A	London – Van der Waals energy, J m^{-2}
V_E	Electrostatic double layer energy, J m^{-2}
V_{eo}	Maximum velocity of fluid, m s^{-1}

V_H Hydrophobic energy, J m^{-2}

V_{HD} Hydration energy, J m^{-2}

V_S Steric Energy, J m^{-2}

V_T Total energy, J m^{-2}

z Valence of ion

z_i Valence of ion i in solution

Γ Decay constant, s^{-1}

γ Surface tension, N m^{-1}

ε Dielectric permittivity, equals to $\varepsilon_0\,\varepsilon_r$

ε_0 Permittivity of vacuum, 8.854×10^{-12} F m^{-1}

ε_r Dielectric constant of the solution, F m^{-1}

ζ Zeta-potential, V

η Electrophoretic mobility, m^2 V^{-1} s^{-1}

θ Scattering angle

κ Debye constant, m^{-1}

$1/\kappa$ Debye length, m

λ Decay length, m

$\lambda*$ Wave length of the laser in vacuum, m

μ Viscosity of solution, mN m^{-1}

ρ Volume charge density, C m^{-3}

ρ Liquid density, kg m^{-3}

σ_S Surface charge, C

x_ζ Distance from the particle surface to the shear plane, m

ψ	Potential in an electrical double layer, V
ψ_δ	Stern potential, V
ψ_0	Surface potential, V
∇^2	Laplacian operator, m^{-2}

Chapter 1 Introduction

1.1 The Canadian Oil Sands Industry

World demand for oil has become one of the major concerns in the recent history of human civilization. The prosperity of the world today has led to an unprecedented increase in oil consumption. In order to meet the swiftly accelerating demand for oil, exploitation of accessible new unconventional oil sources has found its critically important role. Oil sands deposit is considered to be a most promising alternative.

Deposits of oil sands are distributed mainly in eight countries: Canada, Venezuela, USA, Trinidad, Madagascar, Albania, Russia and Romania[1]. Canada alone possesses 95 % of the known in-place oil volume. With an EIA (Energy Information Administration) estimated 174.4 billion bbls of oil reserves from oil sands alone, in comparison to the 4.5 billion bbls from the conventional reserves, Canada now ranked the second, only to Saudi Arabia, in total proven oil reserves[1-4]. Oil sands in Canada are mostly located in Athabasca, Cold Lake and Peace River of Northern Alberta (Figure 1-1). The three oil sands deposits cover a total area of 141,000 square kilometres and possess a current oil production capacity of about 1.7 million bbl/d, representing almost 1/2 of the total Canadian crude oil production of 3.4 million bbl/d[2-4]. According to EIA, the daily production of oil sands is looking at 2.2 million bbls by 2025.

The research of Canadian oil sands goes all the way back to 1920's. After going through numerous investigations and explorations, the oil sands operation

1

was finally brought to a real commercial scale by the Great Canadian Oil Sands (now known as Suncor Energy Inc.) in 1967. Syncrude Canada Ltd. started their development in the oil sands operation in the late 1970's. Later in 2003 and 2008, Albian Sands Energy Inc. and CNRL came into commercial operations. With the oil sands becoming a mainstay of the Canadian economy, the oil sands industry draws interest of many more potential investigators[5].

Bitumen, the carbon-rich heavy crude, is the direct product from oil sands. Of all the current mineable oil sands operators, the oil sands operation process (as shown in Figure 1-1) generally includes the basic units of Mining, Utilities, Extraction, Froth treatment, Water management and Upgrading, during which both inorganic and organic chemical additives are added for the sake of better crude oil production. Below is a brief summary of oil sands operations.
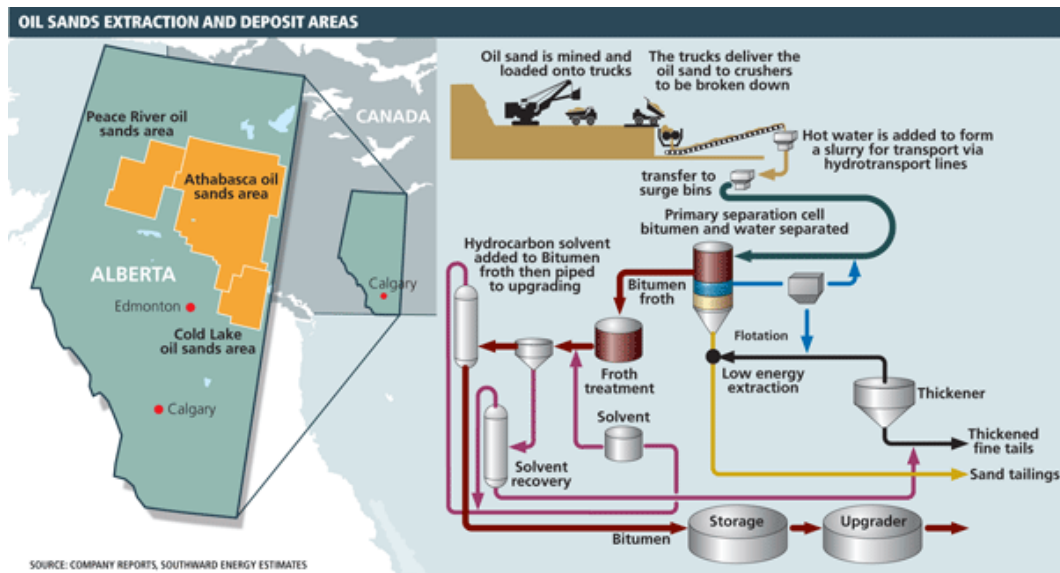
Figure 1-1: General scheme of an oil sands operation system[3].

1.1.1 Athabasca Oil Sands

The Athabasca oil sands deposit is the single largest oil sands deposit not only in Canada but also in the world, extending from the surface to a depth of 750 m[6-9]. The Athabasca oil sands, unlike oil sands from other regions, are highly processable with a water-based extraction process, featuring a commercial bitumen recovery of approximately 88 ~ 95 %. The reason for such success in the commercialization of the Athabasca oil sands operations rests on the unique character of bitumen-covered sand grains. The sand grains of the Athabasca oil sands themselves are hydrophilic. A thin layer of water film, predicted about 10 nm is speculated to be present between the sand grains and bitumen preventing the direct contact of the two substances[5, 10-14]. It is believed that if it was not for this water affinity of the sand grains, the process of separating the bitumen from the oil sands would not have been possible[15].

A typical oil sand ore contains about 75 wt% inorganic matter, 10 wt% bitumen, 10 wt% silt and clay, and 5 wt% water. Based on the bitumen content, oil sands ores can be classified into three categories as low-grade or poor ores, average-grade or medium ores and high-grade or rich ores, with corresponding bitumen content of 6 ~ 8 %, 8 ~ 10 % and 10 ~ 16 % by weight, respectively. Even though the majority of oil sands seems to be the solid fraction—coarse sand, silt and clay, the composition of solid varies from ore to ore. Silt and clays of sizes < 44 μm are referred to as fines whereas the rest of solids, mainly quartz of sizes larger than 44 μm are known as coarse sands. Due to their small sizes, the fines are much more problematic than the coarse sands and may cause

3

considerable reduction in bitumen recovery by slime-coating on the bitumen droplets. The poor oil sands ore can have a fines content up to 40 % and a low bitumen recovery of < 70 %[3, 16, 17].

1.1.2 Bitumen Extraction

Despite the fact that the bitumen extraction process has been extensively studied over the past century by numerous researchers, the hot water extraction process (HWEP) is the only one commercially operational for bitumen extraction, although there are variations in detail among different oil sands operators. HWEP was developed from the series of bench-scale and field-scale separation tests by Clark in the 1920's. The process mainly involves mixing the oil sands with hot water (80 °C) under caustic condition (pH 8.5 ~ 9)[5, 7, 12]. In responding to the global advocacy of energy efficiency, further advancements were made and new technologies were developed based on the conventional HWEP, making it less energy intensive and more economically profitable. The OSLO cold water extraction process (OCWE), or the low energy extraction process[5, 18, 19], is a representative example of such energy-saving technology.

In HWEP, bitumen is first liberated from hydrophilic sand grains. The liberated bitumen becomes aerated by attaching to (at low temperature) and engulfing (at high temperature) flotation bubbles. The aerated bitumen, in the form of bitumen-bubble aggregates, floats to the top of a separation vessel or flotation cell under the buoyancy to form a bitumen rich froth which usually contains 60 % bitumen, 30 % water and 10 % solids. The bitumen-rich froth is then de-aerated and diluted with organic solvents. The solids and water in the

4

diluted froth are removed by using inclined plate settlers, cyclones and/or centrifuges. After recovery of diluting solvent for recycle, the "clean" bitumen is finally upgraded to produce synthetic crude oil[5].

Through a century's effort of many groups of researchers and engineers, great achievements were made, not only improving bitumen recovery and process efficiency but also providing in-depth understanding of the underlying fundamentals of the extraction process by the application of the most recently developed investigation techniques such as atomic force microscope (AFM) and surface force apparatus (SFA). However, the bitumen extraction process is a complex system of complicated physical, chemical, interfacial and hydrodynamic conditions and many of its mechanisms are still not fully comprehensible. Among all the aspects that have been studied regarding the process, the interactions of bitumen, solid and bubbles remains the focus of interest and recognized by many researchers[20-26] as of predominate importance. Such interactions or interfacial behaviours form the basis of the whole bitumen extraction process. Studies of interfacial phenomena in a bitumen extraction system have been fruitful and further investigations are still anticipated.

1.2   Object of This Work

For the fact that the interactions among bitumen droplets, solids and bubbles are critically important, understanding their interaction mechanism is therefore of great scientific and technological importance. This study aims at achieving a more comprehensive understanding of bubble-solid interactions in a colloidal system for the concern of slime-coating (of fines) on flotation bubbles in

the bitumen extraction process by the recent technology of zeta-potential distribution analysis. Researchers have been successful in finding direct evidence of slime-coating or armour-coating on surface of bitumen droplets through novel use of the technique[23-29]. However, due to strict requirements of the method on the size, stability, amount as well as mobility of the material in the vertical direction, the difficulty of adopting the technique for bubble-solid interactions is apparent. It has long been suggested that bubbles of very small sizes, such as nano bubbles or submicron size bubbles, have negligible buoyancy and would remain well suspended in aqueous solutions for as long as months[30-34]. Thus by generating submicron size bubbles, there is a good chance to apply the zeta-potential distribution analysis technique to studying bubble-solid interactions. To achieve the mentioned purpose, the experiments are designed accordingly with the following goals:

1) Generate submicron size bubbles (<1 μm) via high intensity agitation (HIA);

2) Investigate effect of operating parameters such as agitation speed, time, and temperature on generation of submicron size bubbles;

3) Examine the physicochemical properties of the submicron size bubbles as well as their physical characters such as stability, size and amount as a function of time;

4) Establish fundamentals for the bubble-solid interaction mechanism by studying the interactions of submicron size bubbles with model silica, alumina and carbon black particles in electrolyte and surfactant/frother solutions using the zeta-potential distribution analysis technique;

5) Determine armour-coating of air bubbles and their role in air-bitumen interactions by extending the zeta-potential distribution analysis experiments to an industrial oilsands production environment.

Chapter 2 Literature Review

2.1   Bitumen Aeration: The Relationship of Bitumen, Bubbles and Solids

Bitumen aeration is a crucial step in the bitumen extraction process where air is introduced into the system[35-37], making it a ternary aqueous mixture of liberated bitumen droplets, bubbles—the inducted larger flotation bubbles and the already existing gas nuclei, and solid particles of coarse and fine sizes. The goal of bitumen aeration is to separate bitumen from the majority of water and solid particles by floating them to the top of the slurry with air bubbles and forming a thick bitumen froth. Therefore, bitumen aeration can also be seen as a competitive attachment process among the bitumen droplets, bubbles and solid particles of which bitumen-bubble attachment is favoured while bitumen-solid and/or solid-bubble attachment is disfavoured as both of them tend to reduce the bitumen recovery by either hindering the attachment of bitumen to bubbles and/or reducing bitumen froth quality by bringing in unwanted impurities to the froth. It is therefore quite clear that understanding the interaction mechanism of the substances in a bitumen extraction process is of great practical importance for both establishing the scientific foundation of the oil sands processing technology and continuously improving its production efficiency.

The mechanism of bitumen/bubble/solid interactions involves basic knowledge of relevant hydrodynamics and surface chemistry[21, 23, 24, 26, 27, 38-44]. When dealing with computational or experimental force analysis, the classic or extended DLVO (Derjaguin-Landau-Verwey-Overbeek) theory is more than

likely to be applied[37, 45-50]. Over the past few decades, massive effort has been devoted to the field and some of them will be discussed in details in the upcoming sections.

2.1.1 Bitumen and Solids

Under the high temperature condition of bitumen extraction, bitumen in the oilsands lumps is liberated from hydrophilic sand grains when exposed to certain shear force. Since both the sand grain and the naturally occurring fine solids are hydrophilic, theoretically, they should not experience adhesive interaction with hydrophobic bitumen droplets after bitumen liberation[51]. However, due to the complexity of the bitumen extraction system, which contains at least natural surfactants and extremely high concentration of electrolytes, bitumen-solid interactions has to be considered[16, 23-25, 27-29]. Among the many assumed explanations for this hetero-coagulation of bitumen and solids, some of them have been extensively studied and directly proven[23-25, 28, 29].

Slime-coating of bitumen is where the surface of a free bitumen droplet is covered by a layer of fine solids which prevents the attachment of the bitumen droplets to air bubbles. Slime-coating has been suggested as the cause of the poor processability of a poor oil sands ore[23, 24, 37]. Such phenomenon was strongly supported by the results of Liu *et al.*[23, 24, 37], who applied a more recently developed technique of zeta-potential distribution analysis to the observation. It was found in their study that in the presence of 1 mM Ca^{2+}, montmorillonite clays strongly attached to the bitumen surface in 1 mM KCl solutions (pH 8), which resulted in a full layer of clay shelter, derived from a single zeta-potential

distribution peak standing in the position of the clay's zeta-potential distribution when measured individually for a 1:1 ratio bitumen and clay mixture[23, 37]. However, without Ca^{2+} addition or when 1000 ppm of bicarbonates was added to the solution, the attachment of montmorillonite clays to the bitumen droplets was hardly detectable[29]. The explanation for the bitumen-clay attachment here is that Ca^{2+} bonds to both the bitumen and clay surfaces acting as a bridge assisting the hetero-coagulation[25, 29]. Similar zeta-potential distribution results were found in experiments where the montmorillonite clays were replaced by the weathered illite clays, while no attachment of kaolinite clays at bitumen surface was found under all conditions[25, 52]. For the case of a real oil sands system where the bitumen and clays were extracted from an oil sands ore and examined under the chemical environment of the corresponding process water, Liu *et al*. (2004, 2005) discovered that hetero-coagulation was obvious in the system of a poor oil sands ore where both the fines and divalent ions content was high while the bitumen-clay attachment was minimal in a good processing ore system of which the concentration of fines and divalent ions were relatively lower. They also found out that the zeta-potential distribution of froth from a poor processing ore was almost identical to that of the individually measured clays, confirming the argument that slime-coating is the reason for the large amount of fine solids in the froth of the poor processing ore causing the low bitumen recovery[23, 24, 37].

The findings of the zeta-potential distribution analysis were assured by the results of direct force measurements using AFM[23, 24, 37]. At pH around 8, the AFM results showed a stronger adhesion force for bitumen-montmorillonite clays

than bitumen-kaolinite clays with Ca^{2+} addition. The interaction forces between

bitumen and fines of a good processing ore were clearly repulsive while that

between bitumen and fines of a poor processing ore were attractive at small

separation distance. The normalized interaction forces measured by AFM further

confirmed that the hetero-coagulation of bitumen and solid particles such as clays

and silica were highly dependent on pH and Ca^{2+} concentration. An increase in

pH led to a reduction in bitumen-silica attachment while an increase in Ca^{2+}

concentration resulted in a stronger bitumen-silica and bitumen-clay

attachment[23, 37]. It was found by film flotation that fines of good processing ores

were hydrophilic while fines of poor processing ore were to some extend

hydrophobic[24]. Zhao *et al.* (2006) also performed a series of experiment on

bitumen-silica interactions with both AFM and zeta-potential distribution analysis

and found that not only was divalent ion concentration important in controlling

bitumen-silica interactions, but also were surfactants such as SDS[53]. It was

concluded from these earlier studies that the electrostatic force was dominant in

the systems of bitumen-silica, bitumen-clays and bitumen-fines of a good

processing ore, whereas both the electrostatic force and hydrophobic force was in

charge of the attachment of bitumen with fines of a poor processing ore.

2.1.2   *Bitumen and Bubbles*

It is believed that even before extra air was introduced into a bitumen

extraction system, some gas nuclei already existed[5, 7, 54, 55]. The tiny gas nuclei

were formed by release of the entrained gas within the oil sands matrix during oil

sands conditioning and would attach to the bitumen droplets. Even though it was

proven that the presence of such gas nuclei was insufficient in floating the bitumen to the froth[36], the importance of these small gas nuclei should not be disregarded. In order to achieve a reasonable commercial bitumen recovery from oil sands, additional air was needed. The role of induced air in affecting the bitumen recovery was demonstrated by Bichard in 1987.

The effect of bubble size on bitumen-bubble attachment is evident. Earlier studies agreed that small bubbles were in general more likely to attach to bitumen droplets[12, 21]. Moran *et al*. (2000) found in their study that for a flotation bubble with a size within the millimetre range, a bitumen droplet of 3 orders of magnitude smaller in size was much more difficult to attach. The phenomenon was further studied by Yang *et al*. (2000) and Gu *et al*. (2004) using different apparatus. By measuring the induction time, which is the minimum time required for the water film in between the bitumen droplet and bubble to thin to a critical thickness so that a stable three-phase contact could be established[56, 57], Gu *et al*. (2004) were able to confirm that smaller size bubbles resulted in a shorter induction time and thus better bitumen-bubble attachment. Moreover, when the bubble size exceeded a certain limit, no attachment was observed[21].One other interesting fact which they found during their observation was that under the circumstance where tiny gas nuclei were present, the size range for bubbles to attach to bitumen surface was for some reason, greatly broadened, i.e. larger bubbles were also able to attach[21]. The degassing experiments of the gas nuclei from solution reassured that it was the gas nuclei that contributed to the bitumen-bubble attachment. The possible hypothesis is that gas nuclei acting as a linkage

12

between the two substances[42, 58-60]. Many other mechanisms were also proposed. Wang *et al.* (2005) demonstrated the effect of surface properties on bitumen-bubble interactions by recording and analyzing the attachment of bubbles to bitumen droplets in aqueous solutions. They found that the hydrophobicity of the bitumen surface was a prerequisite for the attachment to take place. Nevertheless, no simple conclusion can be given to as what is affecting bitumen-bubble interactions. Various studies had suggested that temperature, the gases type of formed bubbles and the water chemistry were all important factors. In short, higher temperature is in favour of bitumen-bubble attachment while surfactant addition was unfavourable. Hydrogen bubbles had a shorter induction time than oxygen bubbles[21, 22, 28].

Different attachment behaviour was found for good processing ore and bad processing ore[61, 62]. It was observed by the researchers that attachment of bubbles to bitumen from the good processing ore was so strong that when attempting to pull them apart, the bubble itself broke into two parts instead of breaking the bitumen-bubble contact. For the case of bitumen from the poor processing ore, although the contact of bitumen and bubble was also established, the bubbles detached completely from the bitumen upon separation[61, 62]. Such results were in good agreement with those of bitumen-bubble aggregation, bitumen loading on an air bubble and gas hold up of corresponding process water. Larger aggregates and higher bitumen loading were seen in the system of good processing ores, while smaller aggregate size and lower bitumen loading were measured for poor processing ores, both at 50 ºC. In addition, the gas hold up of

13

process water from the poor processing ores was much higher than that of process water from good processing ores under the same aeration conditions[63, 64]. The photographs of bitumen loading by Malysa *et al.* (1999) were another robust evidence that bubbles can be easily loaded with bitumen of good processing ore but not with bitumen of poor processing ore. Clearly, bitumen-bubble attachment of different ore is also a reason for the difference in their bitumen recovery.

2.1.3   *Bubbles and Solids*

In addition to bitumen-solid attachment which depresses the bitumen recovery, there is also a possibility of bubble-solid attachment which may prevent bitumen-bubble attachment and hence hamper bitumen flotation efficiency. Bubble is a most important working element in all flotation systems, and thus was intensively studied during the history of flotation, especially in mineral flotation and coal flotation[38, 44, 65-69]. The previous researchers have shown that the size of a bubble significantly influences the flotation process and bubbles of micron size tend to improve the flotation recovery of smaller particles[58, 66, 70]. It was also established that bubbles or gas nuclei of sub micron size (or nano size) assist the flotation of fine particles (< 5 μm) which otherwise could not be successfully floated by conventional flotation bubbles[70, 71].

2.1.3.1 Interactions between Bubbles and Hydrophobic Particles

Induction time study of interactions between air bubbles and hydrophobic silica particles in 5×10^{-4} M KCl solutions indicated that increasing bubble size would cause an increase in induction time. This size effect was shown to be more

14

pronounced when the size of silica particles was also larger[22]. It was also shown

by the study that the addition of cation surfactant such as dodecylamine

hydrochloride (DAH) enhanced the attachment of bubbles to untreated silica

sphere, which is hydrophilic. However the attachment was relatively weaker

compared to the attachment between bubbles and hydrophobic silica particles.

The reason for bubble-silica attachment was inevitably related to the

hydrophobicity of the silica particles: the more hydrophobic, the silica surface, the

larger, the contact area and the shorter the induction time, leading to a stronger

attachment[22]. Untreated silica remains hydrophilic unless contamination occurred

at the surface[72]. When a hydrophilic silica particle was placed in an aqueous

environment with DAH addition, the positively charged surfactant tends to adsorb

on negatively charged silica surface, leaving their hydrophobic hydrocarbon tail

exposed to the bulk solution and therefore rendering the surface to some

hydrophobicity, which is still less than that of the hydrophobic silica[22].

Nevertheless, hydrophobicity was not the only factor to make a difference in

bubble-hydrophobic particle interaction. Yang *et al*. (2000) discovered by their

impinging jet system that even with attractive hydrophobic force between two

hydrophobic surfaces, the attachment of bubbles on methylated (hydrophobic)

glass surface was significantly influenced by electrostatic double layer force due

to the surface charge of the substances. The electrostatic double layer force is

strongly influenced by changes of pH, simple electrolyte concentration and

multivalent ion addition. The general trend found in the study was that higher pH

resulted in a reduction in the amount of bubbles attached to the glass surface,

whereas a higher electrolyte concentration led to a better attachment of the

bubbles with the effect being proportional to the charge of the metal ions[73].

Researchers speculated that the influence of the above parameter was directly

related to their impact on the electrical double layer and zeta-potential (which is a

parameter used for approximately describing the surface potential by

electrokinetic measurements and will be discussed in details later) of the bubbles

and hydrophobic glass surfaces, which in turn, altered the electrostatic force.

Simple electrolyte such as Na^+ tends to compress the electrical double layer and

decrease the magnitude of zeta-potential, while the multivalent ions such like Ca^{2+}

and Al^{3+} are capable not only of reducing the absolute zeta-potential values but

also somewhat reversing their signs. Both effects can make the electrostatic force

less repulsive or even attractive. Higher pH, which would bring in higher OH^-

concentration, on the other hand, has the tendency of making the bubbles and

glass surface more negatively charged, thereby inducing a more repulsive

electrostatic force[25, 29, 74-78].

2.1.3.2 Interactions between Bubbles and Hydrophilic Particles

Both the silica particles and bubbles are negatively charged in water or

simple electrolyte solution when the pH exceeds 3[31, 32, 41, 79-85]. Due to their same

signs in zeta-potential and lack of hydrophobic force, the repulsive electrostatic

double layer force dominates the bubble-silica interactions, accounting for the

overall repulsive interaction force, or in other words, non attachment of the two

objects[73, 86-90]. However, both the zeta-potential and hydrophobicity of a surface

can be easily impaired or even reversed with simple changes in the chemical

condition of the interaction system[31, 32, 41, 78-81, 83-85, 91, 92], making the interaction

similar to that of bubbles and hydrophobic particles. In addition, some researchers

even suggested that hydrophilic silica would attach to bubbles under an entirely

different mechanism of hydrogen bonding between the OH^- groups at the bubble

surface and the $\equiv Si–O–Si\equiv$ on the silica surface when the two are able to

approach considerably close to each other in aqueous solutions[93, 94]. It was also

suggested by Fan *et al*. (2004) that bubble-hydrophilic silica attachment would be

enhanced under alkaline condition as the bubbles tend to be softer and the

deformation the soft bubbles would result in a larger contact area for the hydrogen

bonding.

2.1.3.3 Interactions between Bubbles and Clay Particles

The investigation of partitioning of fine clays at an air-water interface in

NaCl solutions of different pH and different ion concentration indicated that

different clays exhibit a variation in their affinity towards the air-water interface[95].

Results show that, unlike bitumen-clay interactions, kaolinite clays and illite

clays both prefer the air-water interface at lower pH (< pH 7) with kaolinite being

the most inclined, while Na-montmorillonite clays and bentonite clays were found

to be exclusive from air-water interface regardless of the pH value and electrolyte

concentration[95]. Such results suggest that under the high pH (> pH 8) condition

free of surfactants and multivalent cations, it is unlikely that clays would coat on

the bubble surface and hinder bitumen flotation. However, an alkaline simple

electrolyte solution is never the situation of a HWEP, as the system contains

inevitably different multivalent ions and natural surfactants. Hence, it would be

17

careless to completely apply the conclusions from Wang and Tokunaga's study to the bitumen extraction system without further investigation. The term armour-coating was defined in mineral and coal flotation as fine clay particles covering the surface of a flotation bubble. Bubble armour-coating by fine ashes has been suspected as a cause for depressed coal flotation[38, 96]. Researchers have shown that fine clay particles or slimes increased froth stability and prevented coarse particles from attaching to the bubble surfaces by armour-coating. Bentonite clays with larger surface area and larger amount of charged sites are most possible to armour-coat the bubble surfaces and dramatically depress coal flotation[38, 96].

All in all, studying the attachment of bubbles to solid particles is of great significance to the oil sands industry, as inefficient bubble-solid attachment would have direct impact on bitumen recovery. The complexity of a bitumen extraction system increases the likeliness of slime-coating on bubbles. It is our final goal to investigate the occurrence of such phenomena and gain comprehension of the inherent fundamentals.

2.2   Bubbles in General

Bubbles, in spite of their variation in size and type of gases, are key factors in a diversity of fields, for example, paper making, waste water treatment, froth flotation, yeast industry, hydrodynamic power recovery systems and more recently, human physiology, biopharmaceutical products, bioreactors, drug delivery and bimolecular separation[58, 59, 97-102].For this reason, bubbles have not only attracted great attention from industry but also stood in the spot light of

18

academia. For most applications that involve bubbles, the process is most likely related to bubble-particle interactions, especially in the flotation process[38, 44, 65, 67, 69, 103]. Over the last few decades, numerous studies[31, 32, 70, 91, 104-110] have been carried out to study gas bubble generation kinetics, bubble dynamics and bubble physicochemical properties including bubble size, surface charge and hydrophobicity, which are recognized as the three most dominant factors affecting bubble-particle attachment. Although micron size bubbles have already been proven to be commercially beneficial in many ways such as improving transport efficiency and flotation of fine particles[66, 70], the higher specific surface area of even smaller bubbles and their ability to increase gas dissolution make the smaller bubbles increasingly attractive. From the academic prospective, the limitation of micron size bubbles appears to be more noticeable. The high rising velocity of micron size bubbles is known as a restriction in studying the properties of bubbles by electrophoretic mobility measurement, a common technique used to determine bubble surface charge characteristics[32]. Former researchers have shown that the rising velocity of bubbles decreased with reducing bubble sizes[111]. As a consequence, generating bubbles of even smaller size (less than the micron scale) is of academic interest.

2.2.1   Nano Bubbles (Submicron Size Bubbles)

Submicron size bubbles or nano bubbles are smaller gas bubbles of several hundred nanometres in size[31-34, 112], usually a mixture of water vapour and naturally or intentionally dissolved gases[105, 112, 113]. It has been reported that such bubbles have negligible buoyancy and would remain suspended in solutions for

up to several months[30-34]. Such stable bubbles of negligible bubble rising velocity would make the electrophoretic mobility measurement of bubbles reliable and convenient[32]. In our case, it fits our purpose of determining zeta-potential distribution perfectly.

The existence and stability of nano bubbles or submicron size bubbles in solutions under normal atmospheric conditions have long been a subject of speculations. One of the major debates is that bubbles of such small size could not be thermodynamically possible[30-32, 60, 114-117]. Theoretically, calculation by Laplace – Young equation $P_{in} = P_{out} + \frac{2\gamma}{R}$ (where γ is the surface tension and R is the radius) would result in an internal pressure of a nano bubble dramatically larger than the atmospheric pressure. Thus, nano bubbles should not be in equilibrium state and would dissolve into its surrounding environment instantly[60, 117-119]. However, the existence of nano bubbles both on solid surface and in aqueous solutions are confirmed experimentally[31, 32, 60, 114, 120, 121]. There are usually three hypothesises in explaining the discrepancy between Laplace – Young equation and experimental results: 1) instead of being in equilibrium state, the nano bubbles are in kinetic equilibrium state of extremely long equilibration time[122]; 2) the nano bubbles are in equilibrium state but within a supersaturated solution providing the self-reformation of the nano bubbles and their uniform size under the same experiment condition[122]; 3) the Laplace – Young equation is not applicable in case of nano bubbles as the surface tension γ in such situation is greatly affected by the interface curvature and internal gas pressure which are

20

intercalated i.e. the surface tension changes with the curvature of gas-liquid interface[60, 117, 123, 124].

2.1.1.1 Generation of Nano Bubbles (Submicron Size Bubbles)

Presence of nano bubbles has been witnessed during many experimental studies. Although existence of nano bubbles has always been somewhat doubtful, and even proven to be a mistake caused by contamination for its irregular shape[60, 125], the facticity of nano bubbles was nevertheless testified by other researchers to be true through observation of their time-dependent stability, gas concentration-influenced generation and disappearance under vacuum[60, 114, 117, 126-129]. Nano bubbles are more commonly found in forms of gas envelopes and hemi-spheres at solid surfaces than suspended spherical gas bubbles in bulk solutions. But all in all, generation of freely suspended nano bubbles can take place under given circumstances: the homogenous liquid phase undergoes a phase change caused by a sudden pressure reduction below a certain critical value (or known as cavitation)[31, 70, 130]; a chemical reaction such as electrolysis which is largely dependent on the solutions ionic strength and temperature[121, 131]; or a autogenous generation process due to gas desorption of a supersaturated solution[32, 115, 120, 132, 133]. Based on different bubble generation mechanisms, many researchers[31, 32, 117, 131] have successfully generated nano bubbles and were able to achieve better understanding of both the bubble generation process and the properties of the nano bubbles.

Cavitation is one of the most widely applied methods in generating nano bubbles. According to its origin; it can be classified into four groups:

hydrodynamic cavitation (cavitation caused by a fluid flow); acoustic cavitation (cavitation orientated from an acoustic field, of which mostly commonly ultrasonic cavitation); optical cavitation (cavitation as a result of local energy deposit such as photons of laser) and particle cavitation (cavitation evoked by elementary particles)[130]. Cho *et al*. (2005) were able to generate bubbles of several hundred nanometres via ultrasonication using palladium-coated electrodes. Xu's group (2006) successfully generated tiny bubbles through hydrodynamic cavitation which was caused by high intensity agitation (HIA).

Parameters related to nano bubble generation are complicated and not fully understood. Parameters such as temperature, electrolyte concentration, surfactant or frother concentration and dissolved gas content in a solution were all reported to have significant impact on bubble generation and subsequent propensities of the generated bubbles such as their size distribution, zeta-potential and hydrophobicity[31, 32, 70, 85, 104-106, 109, 115, 117, 130, 134-137]. The type of gas and solution used for bubble generation were also know as dominate factors in controlling generation and properties of nano bubbles: O_2, CO_2 and H_2 were found to have better bubble generation efficiency than air, i.e. being able to generate larger amount of bubbles with better stability, which is likely the result of better gas dissolubility. Many researchers also believe that the water structure plays an important role in bubble generation[60, 116, 117, 122, 133, 138]. Literature has also shown that hydrophobic solid particles with rough surface tend to promote bubble generation while the role of hydrophilic particle is more debatable[51, 60, 130, 137, 139-141].

2.1.1.2 Properties of Nano Bubbles (Submicron Size Bubbles)

Nano bubbles and submicron size bubbles are usually negatively charged in water and simple electrolyte solutions at most pHs[32, 130, 131, 138, 142, 142-144]. Zeta-potential values of bubbles are usually used in experimental studies as an approximation of the bubble surface charge. The reason of the negative zeta-potential of gas bubbles is said to be related to the preferential adsorption of OH⁻ at water-gas interface due to the enthalpy difference of hydration for OH⁻ and H⁺ ions[32, 85, 145-147]. As a result, zeta-potential of bubbles are highly dependent of pH. The most commonly studied properties of nano bubbles are their sizes, surface chemistry and stability of which one is often connect to another. Thus any parameter affecting the three characters may change the properties of the bubbles entirely. Parameters such as temperature, dissolved gas content and type of gas and solution also have considerable impact on nano bubble generation.[31, 32, 70, 85, 104-106, 109, 115, 117, 130, 134-136]. Table 2-1 provides some reported zeta-potential and size values of air bubbles in different solutions.

Table 2-1: Reported zeta-potential values of nano bubbles.

Gas	Solution	pH	Bubble Size (nm)	Bubble ζ-potential (mV)	Reference
Air	water	not adjusted	140 ~ 350	≈ -20	Ushikubo *et al.*, 2010
Air	0.01M NaCl	6.5	≈ 290	≈ -20	Najafi *et al.*,2007
Air	water	6.0	750 ~800	≈ -20	Cho *et al.*, 2005

As mentioned previously, the life time of nano bubbles has been known to be extremely long regardless of theoretical contradictions. Najafi *et al.* (2007)

were able to generate nano bubbles which remained stable for several minutes while Ushikubo *et al*. (2010) reported air bubbles and O_2 bubbles being stable for 1 hr and 15 days, correspondently. Other studies also claimed existence of bubbles being stable in aqueous solutions for as long as a few months[33]. The extreme stability of nano bubbles is their most abnormal character when considering conventional thermodynamics. After many years of investigation, researchers have come up with many explanations for existence and stability of nano/submicron size bubbles in an aqueous solution. Nevertheless, the three classical explanations are: Harvey nuclei—bubbles existing in crevices of very small contamination particles or other achievable macroscopic surfaces[51, 112, 148]; continuous formation of gas nuclei by cosmic radiation[112]; and finally, the concept of an "organic skin"[112, 149], which is similar to the concept of "contamination"[137, 150, 151]. More recently, Ohgaki *et al*. (2010) suggested that the stability of nano bubbles should be strongly related to hydrogen bonding at water-gas interface and Bunkin *et al*. (2007, 2008) indicated that adsorption of ions on bubble surface accounts for the stability of nano bubbles. Ushikubo and co-workers (2010) discovered that bubbles with larger absolute zeta-potential values (> 30 mV) were much more stable than those with absolute zeta-potential values less than 30 mV. They suggested that the stability of nano bubbles is probably a result of repulsion caused by overlapping of the electrical double layer of the neighbouring bubbles.

2.2.2   *Surfactant/Frother and Bubbles*

Frother and surfactant are a group of polymer like surface-active molecules which are widely used in flotation[85, 152-154]. A general structure of a

frother or surfactant is composed of a hydrocarbon chain as the hydrophobic tail and a hydrophilic head, which is usually –OH or alkoxy ($O-C_nH_{n+1}$) in the case frother and ions such as Na^+ and NH_4^+ in the case of surfactant. This mixed polarity accounts for their ability of adsorbing at the gas-water interface[154]. Due to their unique character, frother and surfactant were found to be closely related to bubbles generation in aqueous solutions.

Frother and surfactant are known to reduce the bubbles size and improve their stability[31, 85, 135, 136, 154-157]. Even though frother and surfactant are known to reduce surface tension, their effect on bubble size and stability does not seem directly relevant[154, 158, 159]. A "breakup" mechanism for frother promoted bubbles in a conventional flotation tank was recently proposed by Finch and co-workers (2008). They suggest that surface active molecules (frother and surfactant) at gas-water interface arouse a force in direction away from their point of insertion, and together with the opposing force provided by the adjacent water molecules, a bulge is formed at the bubble surface. Due to the low surface tension caused by the surface active molecules at the neck of the bulge, the bulge eventually breaks away from the original bubble resulting in smaller bubbles[154]. This mechanism can also be used to explain formation of smaller bubble in solutions with high electrolyte concentration. However, Finch *et al*. (2008) also state that this "breakup" mechanism of reduced bubble size does not work alone as it is possibly assisted by turbulence at the impeller-stator region in a flotation tank[154]. The other commonly accepted explanation for the effect of frother and surfactant on bubble size is related to their prevention of bubble coalescence[31, 160], of which the

mechanism is not thoroughly established. By combing both the "breakup" and coalescence theories, a more comprehensive explanation for influence of frother and surfactant on bubbles could be achieved.

Absorption of frother and surfactant at bubble surface has also been reported to impact the bubble surface charge[85, 91, 145, 161]. Former results show that, although frother is considered to be non-ionic, it is still capable of modifying zeta-potential of bubbles by changing the thickness of electrical double layer of the bubbles[85, 162, 163]. The type and concentration of frother and surfactant both influence the zeta-potential of bubbles. A previous study showed that, frother at very low concentration hardly had an effect on zeta-potential of bubbles, but with an increase in concentration, the effect became more obvious—either continuously lowering or increasing the magnitude of zeta-potential[85]. The reason for surfactants controlling the bubble zeta-potential is much easier to understand as for their ionic character. Surfactant, which adsorbs at gas-water interface, would bring along a corresponding charge to the surface of the bubbles and change the original charge of the bubbles. Cationic surfactant is shown to make the negatively charged bubbles less negative and even to reverse the sign with increasing surfactant concentration; the anionic surfactant tends to further decrease the negative zeta-potential, making it more negative with increased surfactant concentration. However, when the concentration reaches the critical micelle concentration (CMC) of the surfactant, the zeta-potential of the bubble seems to have reached a peak value and starts to level off[31, 32]. According the

influence of frother and surfactant on the properties of the bubbles, their role in bubble-particle interactions is also critically important.

2.3   Colloidal Systems and Colloidal Interaction Forces

2.3.1   Colloidal Systems

Colloidal systems are essential to daily life. Some of the examples are aerosols, cement, ink, cosmetics, emulsions, soil, body fluids as well as intercellular fluids[76] where industrial processes like flotation and water treatment also rely on them heavily.

A colloidal system is an intimate mixture that consists of a dispersed phase and a continuous phase. The dispersed phase is uniformly distributed in a microscopically divided state through the continuous phase. Both the dispersed phase and continuous phase can be solids, liquids or gas, making the colloidal system usually a free combination of the three substances. Although the dispersed phase of a colloidal system is usually particles, droplets or bubbles with a diameter from several to several hundred nanometres, often making them invisible to optical microscopes[164], there is no obvious distinction between a colloidal system and a non-colloidal one[76]. Based on their thermodynamic stability, colloidal systems can be organized into three groups: colloidal dispersions which are thermodynamically unstable; true solutions of macromolecular material which are thermodynamically stable but reversible; and association colloids which are thermodynamically stable[76].

The stability of a colloidal system is a major concern in colloidal science. Knowledge of establishing and destroying a colloidal system appears to be

equally important[76]. It is well understood that the stability of a colloidal system is the result of the colloidal interaction forces. Therefore, understanding of colloidal systems is basically the understanding of interacting colloidal forces which are namely Van der Waals forces, electrostatic double layer force, hydration force, hydrophobic force and steric force. Such forces will be discussed in details in the following sections.

2.3.2   Electrical Double Layer

Bubbles and solid particles develop an electrical surface charge at their surfaces when in contact with electrolyte solutions according to various mechanisms. Some of the most important mechanisms resulting in such phenomenon include adsorption and desorption of ions at surfaces; ionization or dissociation of surface groups; isomorphous substitution in the lattice of solids; charged crystal surfaces and polarization of interface due to external potential[74, 165]. The surface charge of bubbles and particles leads to rearrangement of free ions distribution in the solution and gives rise to what is know as the electrical double layer—the stern layer and the diffuse layer[165]. The term of electrical double layer was first brought up by Helmholtz in 1879, who described it as a "molecular condenser". In the 1900s, by Gouy and Chapman, the diffused double layer theory was developed, of which a modification was made later on by Stern (1924) and Grahame (1947)[165].

Within a system of suspended particles in electrolyte solution, ions in the solution can be sorted into three categories according to their interaction with the charged surface. Potential determining ions are ions capable of transferring

28

between phases and always interact with the surface; specific adsorbing ions are

ions that interact with the surface by specific mechanisms such as Van der Waals

forces and hydrophobic bonding; indifferent ions (simple electrolyte) have no

interaction with the surface at all[77, 166]. Nevertheless, all three types of ions have

an impact on zeta-potential which will be discussed shortly in the following

paragraphs. Counterions refer to ions baring charge opposing that of the particle

surface, they account for the overall electroneutrality of the system. Counterions

are attracted toward the particle surfaces by coulomb force. Counterions that are

in immediate contact with the surface forms the surface-bonded stern layer while

the diffused layer, on the other hand, is defined as a loosely associate cloud of

ions distributed by thermal force[77, 166]. The thickness of the double layer is

measured by the Debye constant κ which is the ratio of Coulomb force to thermal

energy,

$$\kappa = \left\{ \frac{e^2 \sum n_i(\infty) z_i^{\,2}}{\varepsilon_r \varepsilon_0 k_B T} \right\}^{1/2} \tag{2.1}$$

The summation in Eq. (2.1) is the over all electrolyte ions within the solution,

while e is the charge of electron. $n_i(\infty)$ is the number per unit volume of

electrolyte ions of type i with valence z_i in the bulk solution far away from the

surface, k_B is the Boltzmann's constant with a value of 1.38×10^{-23} J/K, T is the

absolute temperature, ε_0 is the permittivity of vacuum and ε_r is the relative

permittivity (or the dielectric constant) of the solution. The reciprocal of Debye

constant—$1/\kappa$, has a unit of length and is therefore referred as the Debye length.

The non-linear Poisson – Boltzmann equation is a combination of the

Boltzmann equation $n_i = n_i(\infty)\exp\left\{-\dfrac{ez_i\psi}{k_BT}\right\}$ (a description of the ion

concentration around a charged surface), the Poisson equation $\nabla^2 = -\dfrac{\rho}{\varepsilon_r\varepsilon_0}$ and

equation $\rho = \Sigma\, ez_i n_i$ (volume density of charge) when the solution permittivity is

constant. Such equation describes the electrostatic potential ψ around a surface in

electrolyte solution as

$$\varepsilon_r\varepsilon_0\nabla^2\psi = -e\Sigma\, z_i n_i(\infty)\exp\left\{-\frac{ez_i\psi}{k_BT}\right\} \tag{2.2}$$

Eq. (2.2) is based on the Gouy – Chapman model of electrical double layer where

the solvent is considered as a structureless continuum, and ions as point charges.

However, certain limitations and boundary conditions apply to Eq. (2.2). More

specifics could be found in Masliyah and Bhattacharjee (2006).

2.3.2.1 Zeta-Potential

Even though the system is in general electronically neutral, as counterions

are attracted towards the surface and coions (ions with the same charge as the

particle surface) are repelled towards the bulk solution. In this way there will be a

non-uniform ionic distribution around the surface, and for this reason, potential

differences occur within the electrical double layer[77, 165]. The potential at particle

surface is the surface potential ψ_0, which changes into stern potential ψ_δ in the

stern layer and gradually decays to zero in the far-out bulk solution.

Improvements in determining the electrical double layer were made by the Stern

electrical double layer model (Figure 2-1). Instead of seeing ions as point charges, ions are hereby considered with finite size which better estimates the reality. The stern layer in the Stern model is defined as the gap between the surface and the stern plane which is an inner boundary given by approximately the radius of one hydrated ion. The diffuse layer in such model is described as a mobile part located behind the stern layer. A distance about the radii of one to two ions exists between the stern plane and the diffuse layer, the boundary of which is defined as the shear plane and potential of which as zeta-potential (ζ)[77, 165].

Zeta-potential values could be directly measured through electrokinetic measurements by instruments such as Zetaphoremeter (CAD instrument) or ZetaPALS (Malvern Instrument). Although such value is somewhat different from the surface potential ψ_0, yet it is often used as a fair substation in calculations relating interactions of electrical double layer where ψ_0 is needed[76, 77, 165]. The extrapolation of surface potential from zeta-potential by Laplace operator for flat surfaces is shown as[77]

$$\psi_0 = \frac{4k_B T}{ez} a \tanh\left[\tanh\left(\frac{ez\varsigma}{4k_B T}\right)\exp(\kappa\chi_\varsigma)\right] \tag{2.3}$$

where x_ζ is the distance from the particle surface to the shear plane.

There are several solutions for calculating the zeta-potential (ζ). Hückel (1924) solutions for electrophoretic velocity when $\kappa a \ll 1$ is written as[77, 165]

$$\eta = \frac{U}{E_\infty} = \frac{2}{3}\frac{\varepsilon\varsigma}{\mu} \qquad\qquad (2.4)$$

where $\eta = \dfrac{U}{E_\infty}$ is the electrophoretic mobility with a unit of (m²/V/s), ε is the

dielectric permittivity which equals to $\varepsilon_r\varepsilon_0$, ς is the zeta-potential and μ is the

viscosity of the solution. When $\kappa a \gg 1$ and $ze\varsigma/k_B T < 1$, the electrophoretic

mobility is expressed in Helmholtz – Smoluchowski equation[165]

$$\eta = \frac{U}{E_\infty} = \frac{\varepsilon\varsigma}{\mu} \qquad\qquad (2.5)$$

For intermediate values of κa in between the extreme conditions of $\kappa a \gg 1$ and

$\kappa a \ll 1$, Henry's solution was applied. Henry's approach is based on the

assumption that the total potential within the double layer is a linear combination

of the electrical double layer potential, the potential due to external electric field

and Debye – Hückel approximation for low surface potential. The electrophoretic

mobility by Henry's solution is written as[165]

$$\eta = \frac{U}{E} = \left[\frac{2\varepsilon\varsigma}{3\mu}\right] f(\kappa a) \qquad\qquad (2.6)$$

The most important term in Eq. (2.6) is the $f(\kappa a)$, known as Henry's function[165]

$$f(\kappa a) = 1 + \frac{1}{16}(\kappa a)^2 - \frac{5}{48}(\kappa a)^3 - \frac{1}{96}(\kappa a)^4 + \frac{1}{96}(\kappa a)^5 + \frac{1}{8}(\kappa a)^4 e^{\kappa a}\left(1 - \frac{(\kappa a)^2}{12}\right)\int_{\kappa a}^{\infty}\left(\frac{e^{-t}}{t}\right)dt$$

$$(2.7)$$

However, Eq. (2.7) is an exponential integral which requires specifically designed

numerical integration schemes or asymptotic series expansions, thus an

approximate for $f(\kappa a)$ by fitting the original curve of Eq. (2.7) is given as

$$f(\kappa a) = \frac{3}{2} - \frac{1}{2\left[1 + a_1 (\kappa a)^{a_2}\right]} \tag{2.8}$$

where $a_1 = 0.072$ and $a_2 = 1.13$[165].

    As shown, both the Hückel and the Helmholtz – Smoluchowski equations provide results independent of particle size, while Henry's solution is a function of particle radius. Thus, Henry's solution would better apply to situation where obvious changes in particle size are seen during experimental procedures.
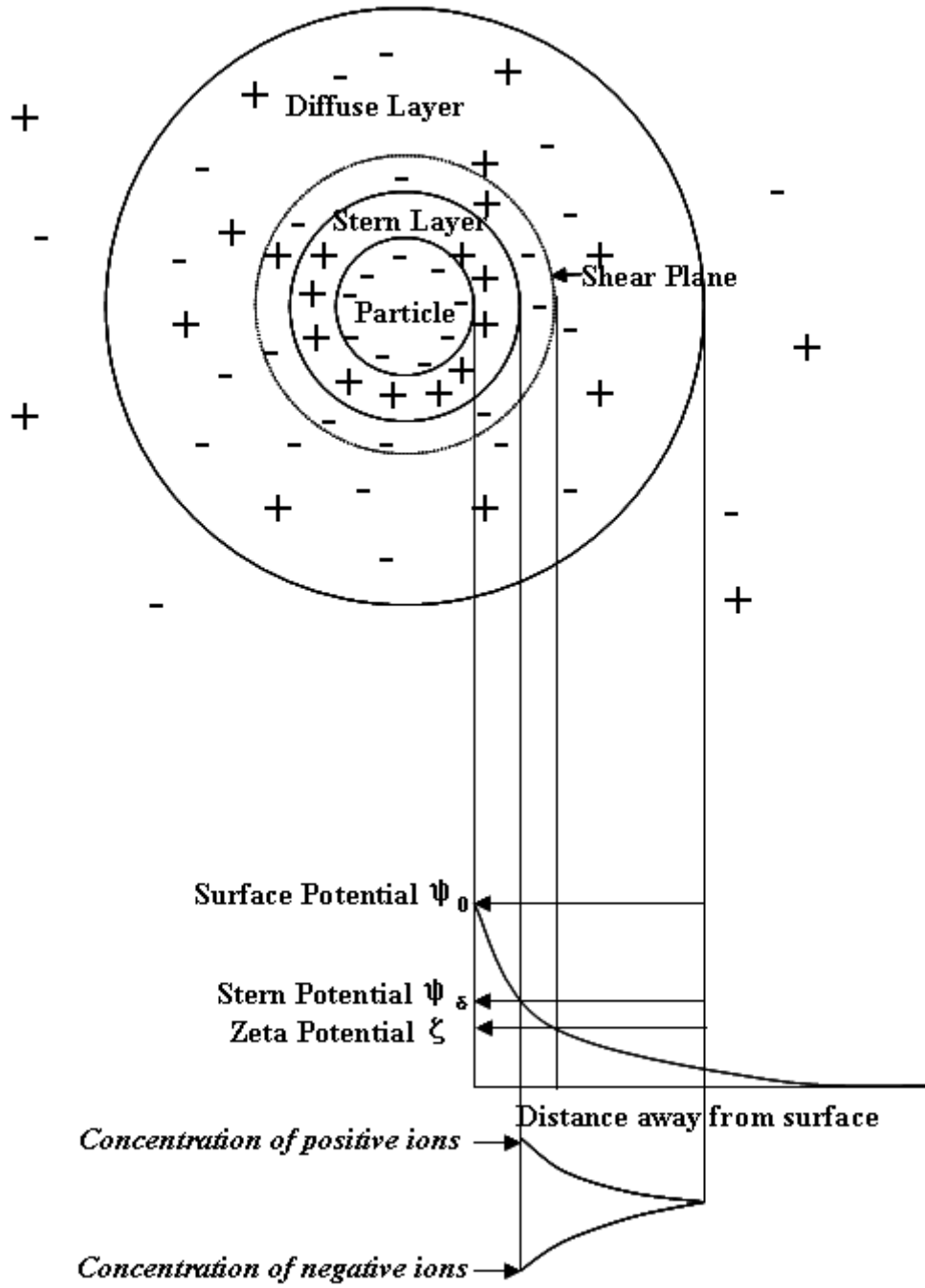
Figure 2-1: Schematic demonstration of an electrical double layer (modified from Nguyen and Schulze, 2003)

2.3.2.2 Point of Zero Charge (PZC) and Isoelectric Point (IEP)

Another important character of particles with an electrical double layer is the point of zero charge (PZC) where the surface charge of the particles σ_s becomes zero due to effect of potential determining ions. Different particles have different PZC in different solutions, but in general, PZC is usually (not always) determined by pH values [74]. This pH value at which the zeta-potential of a particle is measured to be 0 mV is referred as the isoelectric point (IEP). Some reported values of IEP are shown in Table 2-2.

Table 2-2: IEP of selected materials in KCl or NaCl solutions.

Material	IEP	Reference
Silica	pH ≈ 2 or pH < 1.5	Kosmulski,1998; Chernoberezhskii *et al.*,1983
Alumina	pH ≈ 9	Gulicovski *et al.*,2008; Hackley *et al.*,2002
Air Bubble	pH 1.5 ~ 2.5	Li and Somasundaran, 1991; Najafi *et al.*,2007

The importance of PZC and IEP is that they have a major impact on adsorption of ions in the solution, especially that of counterions. At IEP, the particle zeta-potential is 0 mV, exceeding which the zeta-potential of particles starts to reverse and the surface properties start to change. Such changes in zeta-potential or surface charge lead to changes in the corresponding electrostatic double layer force, and thus, variations in particle-particle interactions. IEP is used in this work as a reference in monitoring the surface charge of the selected particle to study the effect of electrostatic double layer force in colloidal interactions.

2.3.3   DLVO Forces (Energies)

A most important property of a colloidal system is its stability defined by the tendency of the particles to aggregate. Aggregation of colloidal particles is a result of colloidal forces and was described independently by Deryagin and Landau and Verwey and Overbeek in their DLVO theory [77]. The DLVO theory involves two major terms: the London – Van der Waals force/energy based on inter-particle distance and the electrostatic double layer force/energy aroused by overlapping of electrical double layer. The total interaction energy in the DLVO theory is the summation of the two forces/energies[76, 77, 165]:

$$V_T = V_A + V_E \tag{2.9}$$

V_A here stands for London – Van der Waals energy which is usually attractive and V_E stands for the electrostatic double layer energy. An energy profile based on the DLVO theory clarifies inter-particle interactions.

2.3.3.1 Van der Waals Forces (Energies)

Van der Waals Forces are short range forces (< 10 nm) which originated form the well known Van der Waals equation of state for non-ideal gases. Such forces are result of three types of electrical interactions: a) the Keesom (orientation) interaction between two randomly oriented dipoles; b) the Debye (induction) interaction between a randomly oriented dipole and an induced dipole; and c) the London (dispersion) interaction between a fluctuating dipole and an induced dipole. With the exception of highly polarized materials, London interaction force (London – Van der Waals force) can explain for most Van der Waals attraction[76, 77]. The London – Van der Waals force only affects over an

extremely short range of distance and decays rapidly as the interaction distance exceeds 10 nm due to electromagnetic retardation.

The Van der Waals forces are usually expressed in terms of energies where the relationship between energy and force is shown as

$$F_A = -\frac{dE}{dh} \tag{2.10}$$

h in Eq. (2.10) is the film thickness between two surfaces.

The London – Van der Waals energy can be calculated using either the Hamaker (microscopic) approach or the Lifshitz (macroscopic or continuum) approach. However, for many practical systems, a combination of the approaches yields results with better accuracy[77]. The Lifshitz approach is computationally inconvenient, thus only the more commonly used Hamaker approach would be illustrated in this section. For two spherical particles of radii R_1 and R_2, and a shortest inter-center distance of h, the London – Van der Waals energy V_A is expressed as,

$$V_A = -\frac{A}{6}\left\{ \frac{2R_1 R_2}{h^2 - (R_1 + R_2)^2} + \frac{2R_1 R_2}{h^2 - (R_1 - R_2)^2} + \ln\frac{h^2 - (R_1 + R_2)^2}{h^2 - (R_1 - R_2)^2} \right\} \tag{2.11}$$

For interaction systems where $h \ll R$, Eq. (2.11) can be asymptotically reduced to,

$$V_A = -\frac{A}{6}\frac{R_1 R_2}{R_1 + R_2} \tag{2.12}$$

which is greatly dependent of the size of the smaller particle. The A in both Eq. (2.11) and Eq. (2.12) is known as the Hamaker constant. The methods in predicting the Hamaker constant by the Hamaker approach and Lifshitz approach are very different. For the Hamaker approach, Hamaker constant is usually

37

experimentally approached. The combining rules are often used here to approximate an unknown Hamaker constant in expression of those that are already known. The Hamaker constant A_{12} of materials 1 and 2 in vacuum is given as,

$$A_{12} = \sqrt{A_{11}A_{22}} \qquad (2.13)$$

A_{11} and A_{22} here are the relative Hamaker constants of symmetrical vacuum systems of materials 1 and 2. And for a system of the two materials (1 and 2) immersed in a medium 3, the effective Hamaker constant is presented in the following way,

$$A_{132} = A_{12} + A_{33} - A_{13} - A_{23} = \left(\sqrt{A_{11}} - \sqrt{A_{33}}\right)\left(\sqrt{A_{22}} - \sqrt{A_{33}}\right) \qquad (2.14)$$

When materials 1 and 2 appear to be the same, Eq. (2.14) simplifies to,

$$A_{131} = \left(\sqrt{A_{11}} - \sqrt{A_{33}}\right)^2 \qquad (2.15)$$

A_{132} (usually with a magnitude around $10^{-19} \sim 10^{-20}$ J) in Eq. (2.15) usually has a positive value where A_{11} and $A_{22} >$ or $< A_{33}$. Therefore, the London – Van der Waals force is attractive. For the more rare cases where $A_{11} > A_{33} > A_{22}$ or $A_{11} < A_{33} < A_{22}$, A_{132} can become negative resulting in a repulsive force[76, 77, 165].

2.3.3.2 Electrostatic Double Layer Force (Energy)

Overlapping of the diffuse layer of two spherical particles submerged in solution results in the electrostatic double layer force (F_E) or energy (V_E). The electrostatic double layer force F_E dependent greatly on the origins of surface charge which are known as: a) constant potential where surface charge is due to adsorption of potential determining ions and the surface potential remains

38

constant while the surface charge density changes accordingly as the two surfaces

approach each other; b) constant charges is the opposite case of constant potential,

and surface charge here is caused by ionization and is the exact opposite case of

constant potential. But for real cases, most systems lie somewhere in

between[76, 167, 168].

The calculation of electrostatic force is based on various approximations

and boundary conditions, and is also presented in forms of interaction energy V_E.

Among the three approximations used: a) Debye – Hückel approximation for low

surface potential ($\dfrac{ze\psi}{k_B T} << 1$) over all separation distances, b) Derjaguin

approximation for inter-center distance smaller than the radii of the spherical

particles, and c) the superposition approximation for particles significantly distant,

the Debye – Hückel approximation is more commonly used. For the case of two

spherical particles 1 and 2, according to Debye – Hückel approximation, Healy

and co-workers successfully expressed the electrostatic double layer energy V_E for

both situations of constant potential (V_E^ψ) and constant charge (V_E^σ) basing on

Poisson – Boltzmann equation[76, 169]:

$$V_E^\psi = \frac{\varepsilon R_1 R_2}{4(R_1 + R_2)}\left\{2\psi_1\psi_2\left[\ln\frac{1+\exp(-\kappa h)}{1-\exp(-\kappa h)}\right] + \left(\psi_1^2 + \psi_2^2\right)\ln\left[1-\exp(-2\kappa h)\right]\right\} \quad (2.16)$$

$$V_E^\sigma = \frac{\varepsilon R_1 R_2}{4(R_1 + R_2)}\left\{2\psi_1\psi_2\left[\ln\frac{1+\exp(-\kappa h)}{1-\exp(-\kappa h)}\right] - \left(\psi_1^2 + \psi_2^2\right)\ln\left[1-\exp(-2\kappa h)\right]\right\} \quad (2.17)$$

The R_1 and R_2, ψ_1 and ψ_2 in Eq. (2.16) and Eq. (2.17) correspondingly stand for

the radii and surface potential of the two interacting particles. κ is the Debye

constant, h is the shortest separation distance and ε is the permittivity of the dispersion medium ($\varepsilon_r\varepsilon_0$). Since the surface potential of a particle is not directly measurable, the zeta-potential are usually applied for calculation purposes. Constant potential and constant charge are somewhat two limits where the more practical case lies somewhere in between. Equation of the mixed case was developed by Kar *et al*. (1973), and it will be discussed later during calculations in Appendix II.

Based on their charged mechanisms, the differences between the cases of constant potential and constant charge are not only a matter of mathematical expression, the energy profiles of the two cases reveal their different impact on two approaching surfaces. For the case of constant potential, F_E of two surfaces is attractive at all separation distances if the surfaces obtain potentials of opposite signs; if the surfaces have potentials of same signs, for values of equal magnitude, F_E is repulsive at all distances, and for values of unequal magnitude, F_E is repulsive at further distance but attractive at the closer distance. When it comes to the case of constant charge, the interaction between two surfaces of like signs is always repulsive despite the separation distance; for two surfaces with opposing signs, F_E is attractive at large separation and repulsive when they come closer, but if the surface charges are of similar magnitude, the surfaces remain attracted to each other even at small separation[77].

2.3.4   *Non-DLVO Forces*

During the past few decades, numerous studies have focused on surface force measurements of two surfaces. However, such studies revealed a

discrepancy between the experimental data and results anticipated by the classic DLVO theory[45, 170-173]. Such findings suggest that other forces besides the DLVO forces are involved in the interactions. Hereby, the extended DLVO theory was introduced which takes account of the repulsive hydration forces F_{HD} for hydrophilic surfaces, attractive hydrophobic forces F_H for hydrophobic surfaces and the repulsive steric force F_S due to adsorption of macromolecules such as surfactants, in addition to London – Van der Waals force F_A and electrostatic double layer force F_E. The extended DLVO gives:

$$F_T = F_A + F_E + F_{HD} + F_H + F_S \tag{2.18}$$

2.3.4.1 Hydration Force

Hydration force was experimentally proved to be a strong short-range repulsive force which arose from the affinity of the hydrophilic surfaces towards water[76]. Water molecules tend to bind strongly to a hydrophilic surface, so if two hydrophilic surfaces want to come close to one another, additional forces was required to remove water molecules from the surface, which is the repulsive hydration force. The hydration force was first found among clay surfaces, where many studies were carried out on clay, silica and mica surfaces[174-179]. One attempt to express hydration force is given by Eq. (2.19) in a single exponential form:

$$F_{HD} = 2\pi \frac{R_1 R_2}{R_1 + R_2} K_{HD} \exp\left(-\frac{h}{\lambda}\right) \hspace{3cm} (2.19)$$

λ in Eq. (2.19) is the decay length while K_{HD} is known as the hydration force constant with a unit of N/m. λ and K values can be obtained through experiments, and are usually about 1 nm and $10^{-2} \sim 10^{-3}$ N/m, respectively. Introduction of hydration force makes the interaction between two surfaces more complicated.

2.3.4.2 Hydrophobic Force

On the contrary of repulsive hydration force, the attractive hydrophobic force is a long-range (>10 nm) interaction force caused by two hydrophobic surfaces trying to eliminate the water between them. Hydrophobic interaction force was found to be much stronger than Van der Waals forces at large separation, and it increases as the surface becomes more hydrophobic. The actual cause of hydrophobic force is still undefined but it is usually believed as a result of attraction by re-orientated H-bonds of water molecule near the surface area to reduce entropy[180].

The hydrophobic force was first experimentally determined and explained in 1982[181], after which several other illustrations have been suggested[182-185]. Most of the studies in determining the hydrophobic force involve direct force measurements such as Langmuir – Blodgett (LB) technique, Surface Force Apparatus (SFA) or Atomic Force Microscope (AFM), and fitting of experimental data with computational or numerical expressions. A double exponential function of two decay lengths is usually applied to provide the best fit for experimental data regarding hydrophobic force,

$$\frac{F_H}{R} = K_H \exp\left(-\frac{h}{\lambda}\right) + K_H * \exp\left(-\frac{h}{\lambda *}\right) \tag{2.20}$$

K_H shown here refers to the hydrophobic constant at decay length $\lambda = 1.2$ nm and

K_H* refers to the hydrophobic constant at $\lambda* = 5.5$ nm (in water), h is the shortest

separation distance, and for bubble-particle interactions, R is the harmonic mean

of the bubble and particle radii, $\dfrac{R_1 R_2}{R_1 + R_2}$. The hydrophobic force could also be

given by a power law which is in similar form as the Van der Waals forces,

$$\frac{F_H}{R} = \frac{K}{h^2} \tag{2.21}$$

One of the most complicated steps in determining the hydrophobic force is the

determination of the hydrophobic constant K, several approaches were made and

further details will be discussed in Appendix II.

2.3.4.3 Steric Force

Steric Force is generally described as a short-range force caused by

adsorption of macromolecules at a surface which affects on a separation range

comparable to twice the contour length of the hydrophobic chains of the

macromolecules.

Depending on the concentration of the macromolecules and character of

the solvent, the steric force would lead to either bridging flocculation or steric

stabilization. Bridging flocculation is an adhesive interaction effect which is a

result of the strong adsorption of macromolecules at low concentration in poor

solvent where the macromolecules likely adsorb to more than one surface thus

pulling them together. Steric stabilization is mainly a repulsive effect due to

coverage of a dense layer of macromolecules on the surface. The two mechanisms of steric stabilization can be concluded as the volume restriction effect (difficulty of compressing the macromolecule layer without penetration of hydrophobic chain) and the interpenetration or osmotic pressure effect (osmotic pressure change due to mixing of the hydrophobic chain). Both mechanisms are related to changes in entropy.

Calculation of steric force involves parameters such as the macromolecular layer thickness L and the average spacing between two grafted points of the molecules s. For a plate-sphere interaction with uncharged macromolecular layer, the expression of steric force by *de Gennes* (1987) is given as[77]

$$\frac{F_S}{R} = \frac{16\pi kTL}{35s^3} \left[7\left(\frac{h}{2L}\right)^{-\frac{5}{4}} + 5\left(\frac{h}{2L}\right)^{\frac{7}{4}} - 12 \right] \text{ for } h < 2L \tag{2.22}$$

Steric force caused by charged macromolecular layer is described by Pincus (1991) as

$$\frac{F_S}{R} = \frac{4\pi kTN_B^2}{Cs^4} \left[\frac{1}{h} - \frac{1}{2L} \right] \text{ for } h < 2L \tag{2.23}$$

C in Eq. (2.23) stands for the electrolyte concentration and N_B stands for the number of monomer units per chain

Chapter 3 Experimentals

3.1   Materials

Unless otherwise stated, Milli-Q water (Millipore) with a resistivity of

18.2 MΩ was used in preparation of all solutions and subsequent suspensions in

this study. To avoid potential contamination of fine particles and microorganisms,

the aqueous solutions were further filtered with Milli-pore filters (Millipore) of

0.1μm pore sizes prior to their use. Reagent grade KCl (Fisher Scientific) was

used as background electrolytes in all solutions and suspensions, reagent grade

$CaCl_2$ (Fisher Scientific) was used as source of divalent cations and reagent grade

HCl (Fisher Scientific) and NaOH (Aldrich) were used as pH modifiers. Sodium

dodecyl sulphate (SDS, Sigma-Aldrich), dodecylamine hydrochloride (DAH,

Acros Organics), methyl isobutyl carbinol or methyl amyl alcohol (MIBC,

Aldrich) and DF250 (Dow Chemical Canada. Inc) were used in support of

submicron size gas bubble generation as well as for adjusting zeta-potentials of

the suspended gas bubbles and fine particles. To study bubble-particle interactions,

nano size Al_2O_3 and SiO_2 powder (claimed to be 15nm), both purchased from

MKnano (Ontario,Canada), mesoporous carbon black nanopowder (Aldrich) and

micron size Al_2O_3 (Fisher Scientific) and SiO_2 (U.S. Silica) particles were used as

received.

Process water (PW), that is Aurora process water I (September 2008,

Syncrude) and Aurora process water II (July 2009, Syncrude), relevantly

simplified as A-I and A-II process water in latter paragraphs, with original pHs of

8.3 and 8.1 were used to relate the laboratorial model systems to the real world oil sands production system. A-I process water was used as the continuous phase of colloidal suspensions for submicron size bubble generation and in zeta-potential measurements. A-II process water was used to perform Denver Cell flotation tests with Posyn ore (Syncrude) of high fines content. The corresponding tailings water, referred to as tailings water, was collected for bubble generation, and later on, as the aqueous phase for zeta-potential measurements. The fines from both the tailings and froth (namely, CF fines-fines collected after centrifuging tailing water, SF fines-fines collected from tailings water after 3 days of sedimentation, and FF fines-fines collected from froth after Dean Stark Extraction) were gathered to study bubble-fines interactions. The electrolyte compositions of A-I and A-II process water are given in Table 3-1 while component analysis of Posyn ore is given in Table 3-2.

Table 3-1: Electrolyte concentration in Aurora process water (mg/L).

Ions Samples	Ca^{2+}	Mg^{2+}	K^+	Na^+	Cl^-	NO_3^-	SO_4^{2-}	HCO_3^-
A-I Process water	26.2	17.5	21.9	550.4	339.6	1.5	117.8	609.0
A-II Process water	32.2	18.1	22.9	527.4	334.9	33.1	320.4	N/A

Table 3-2: Composition of Posyn ore.

Phase Content (wt%)				Electrolyte Content (ppm)			
Bitumen	Water	Solids	Fines	Ca	Mg	Na	K
5.5	5.7	85.9	37.21	33	10.95	109.9	15.5

3.2 Experimental Principles and Apparatus

3.2.1 Experimental Principles

3.2.1.1 Hydrodynamic Cavitation

Hydrodynamic cavitation is produced by a pressure variation due to velocity differences in flowing fluid system. When the pressure of the liquid falls below its vapour pressure or the dissolved gas exceeds its supersaturation level, gas nucleation or precipitation is induced, which is the case of HIA (High Intensity Agitation)[70, 112, 130]. Hydrodynamic cavitation is described by Bernoulli's equation:

$$P + \frac{1}{2}\rho U^2 = C \ \ \text{(constant)} \tag{3.1}$$

where P is the local pressure, ρ is the liquid density and U is the fluid flow velocity. By rearranging the above equation, it is easy to see that when the fluid flow velocity exceeds $\sqrt{\frac{2C}{P}}$, the local pressure will become lower than atmospheric pressure or in other words, negative.

3.2.1.2 Dynamic Light Scattering

Light scattering is a phenomenon inducing periodic oscillations of the electron clouds of the atoms on the irradiated particles when a beam of light (electromagnetic wave) is directed towards a colloidal suspension. The particles appear in the form of scattered light. Depending on the properties of particles, light scattering can be divided into three classes: Rayleigh scattering, Debye scattering and Mie scattering. Techniques for characterizing colloidal systems

47

based on light scattering have been developed and advanced greatly over the past few decades. One of the most popular techniques is know as dynamic light scattering (DLS) or photon correlation spectroscopy (PCS), which uses the laser as the source of illumination.

DLS is a convenient technique for estimating the size/diameter of a colloidal particle and have thus been applied to many commercial instruments such as ZetaPALS (Brookhaven instrument) and NanoZS (Malvern Instrument). The detection of DLS is based on the Brownian motion of the suspended colloidal particles, which is detected as a time-dependent fluctuation in light scattering intensity. This intensity fluctuation of light offers information about the movement of the particles with time, i.e. how rapid the movement of the particles is. The larger, the particle, the slower, the movement, and the smoother, the fluctuation curve appears. The size of the particle is related to the movement of the particles, mathematically following the diffusion coefficient according to Stokes – Einstein equation,

$$d(H) = \frac{k_B T}{3\pi\mu D} \tag{3.2}$$

where $d(H)$ is the hydrodynamic diameter of the particle, D is the diffusion coefficient, k_B is Boltzmann's constant, T is the absolute temperature and μ is the dynamic viscosity of the dispersant. A DLS experiment determines the normalized intensity autocorrelation function $G(\tau)$ which is related to the decay constant Γ by the electric field autocorrelation function $g(\tau)$. The relationship between Γ and D is given by,

$$\Gamma = Dq^2 \tag{3.3}$$

while $q = \dfrac{4\pi n \sin\left(\theta/2\right)}{\lambda *}$ (3.4)

The n, θ and $\lambda*$ in Eq. (3.4) stands for the refractive index of the dispersant, the scattering angle and the wave length of the laser in vacuum respectively. Both θ and $\lambda*$ are the fixed parameters of the instruments. Eventually, the particle size is determined by Eq. (3.2).

3.2.1.3 Electrokinetic Phenomena and Zeta-Potential Measurements

Electrokinetic phenomena are in general related to the mutual transformation effect between electric field and relative motion between charged phases and electrolytes. Among the many types of phenomena that are associated with electrokinetics, the four most commonly referred to electrokinetic phenomena can be summarized as: electroosmosis, streaming potential, electrophoresis and sedimentation potential.

Electroosmosis (Figure 3-1) is the movement of an electrolyte solution relative to a charged stationary surface under an applied electric field, which is likely to occur in a capillary tube. For a negatively charged capillary tube, when an electric field is applied, the excess positive ions near the surface tend to move towards the cathode dragging along the electrolyte solution which results in a movement of the fluid body, known as electroosmosis. The pressure needed for counterbalancing the electroosmotic flow is referred to as the electroosmotic pressure. This phenomenon is critical to many zeta-potential measurement methods.

49

Anode **+** — Electric Field → Cathode **-**   Anode **+** — Electric Field → Cathode **-**

Electroosmosis   **Electrophoresis**

Electric Field →

Counter Pressure →

Stationary Planes

$3/\kappa$

V_{eo}
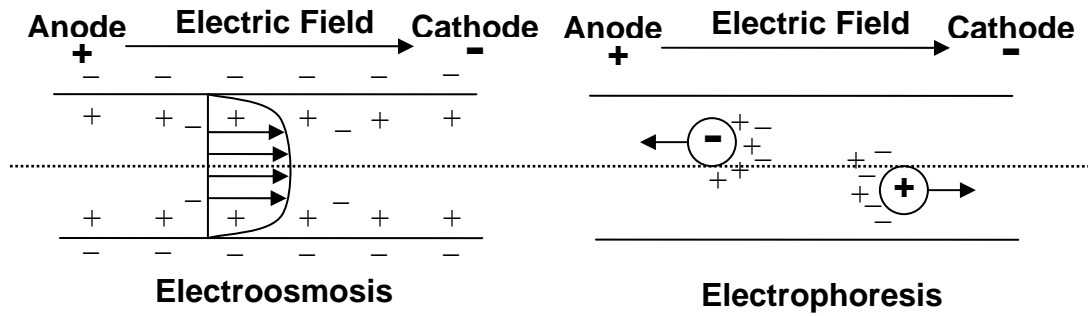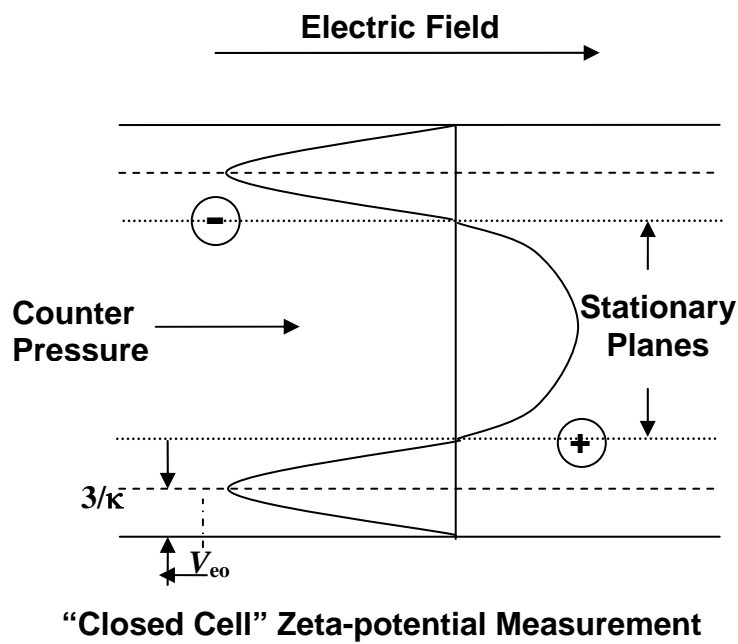
"Closed Cell" Zeta-potential Measurement

Figure 3-1: Schematic demonstration of electroosmosis and electrophoresis, and velocity profile during a "closed cell" zeta-potential measurement (modified from Hunter, 2001)

Streaming Potential refers to a phenomenon where an electric field is generated by the flow of electrolyte solution against charged stationary surfaces driven by applied pressure gradient, e.g. electrolyte solution pumped through a stationary charged tube. This process is usually known as the counterpart of electroosmosis.

Electrophoresis (Figure 3-1) describes the movement of a charged substance, such as a colloidal particle, relative to a stationary fluid body under an external electric field. When an external electric field is applied on a volume of stable colloidal suspension, the charged colloidal particles are forced to move toward the anode or cathode depending on the sign of their surface charge. The negatively charged particles move towards the anode and positively charge ones towards the cathode. Such a phenomenon forms the basis of most zeta-potential measuring techniques.

Sedimentation potential is the electric field created during the movement of charged particles due to gravitational or centrifugal fields. It is sometimes called the Dorn effect or the migration potential. Sedimentation potential is studied far less than the other three electrokinetic phenomena.

Most zeta-potential measuring techniques such as Zetaphoremeter are based on principles of electrophoresis. By using Zetaphoremeter, the zeta-potential of charged particles suspended in an electrolyte solution is measured and calculated as a result of electrophoresis which requires the fluid body to be stationary. However as the zeta-potential measurement in this technique takes place in a quartz capillary (or electrophoresis cell), the electroosmotic pressure is thus unavoidable. In order to solve such a problem, the zeta-potential measurements were preformed under a "closed cell" condition where both ends of the electrophoresis cell are sealed. Under such a condition, the electroosmotic pressure or the maximum velocity of fluid V_{eo} (achieved at about $3/\kappa$ away from the cell surface) is counterbalanced by a counter-pressure in the

51

middle of the cell[186].In this case two planes, known as the stationary planes, are established in the cell where the fluid remains stationary with an absolute velocity of zero. In most cases, the zeta-potential of a material is measured at one of these two planes so that the effect of fluid movement can be minimized. The velocity profile in a "closed" electrophoresis cell is presented in Figure 3-1.

3.2.1.4 Zeta-Potential Distribution Analysis

Zeta-potential is one of the most important parameters in defining the physicochemical properties of a colloidal particle, and thus have been extensively studied by researchers[78, 83-85, 144, 187, 188]. In many zeta-potential measuring techniques, the zeta-potential is often given as an average value. Such techniques work exceedingly well for a lot of cases, especially single component systems. When it comes to a binary mixture, however, the single average value provided by such techniques might be confusing and even misleading as it does not represent the real system. In this case, it is extremely important to have zeta-potential distribution analysis technique.

The one most unique feature of the zeta-potential distribution analysis is to provide zeta-potential distributions illustrating the pool of zeta-potential values of the material being measured. Each individual material has its own zeta-potential distribution. When two materials with different zeta-potential distributions are mixed in a binary system, the shift or change in the zeta-potential distribution of the resulting mixture will provide information relating to the interactions between the participating materials. Figure 3-2 is a schematic demonstration of how the zeta-potential distribution analysis technique is capable

of explaining an interaction which took place in a binary mixture. As shown in the figure, colloidal suspension of particles A and B each gives a zeta-potential distribution of their own with corresponding peak values at ζ_A and ζ_B when measured separately. As the two materials are mixed together, four representational results can be anticipated. The first likely case (Figure 3-2 B) of the mixture distribution is two individual zeta-potential distributions peaked at almost identical values to the individually measured A and B zeta-potential distributions, indicating no attachment between the materials. The particles A and B remain well suspended within the system due to certain repulsive mechanisms. The second expected case is shown in Figure 3-2 C, with a single distribution peak located at almost the same peak values as one of the two material's distributions (in this case, material B), indicating the surface of one material is fully covered by the second material, in other words, a very strong attractive interaction. The third case one may encounter also suggests strong attachment between the two materials: one of the materials—B, tends to attach to the surface of the other material—A. However in this situation, the A surface is only partially covered by B, resulting in a unimodel zeta-potential distribution of the mixture with a new peak value $\zeta_{A/B}$ in between the peaks of individual materials A and B (Figure 3-2 D). Such results are likely caused by an insufficient number of particle B to fully cover A, even though they attach to each other strongly. The last case is when adhesion between the two materials is relatively weak, where both A-B aggregates and A, B individual particles are seen. The distribution of the mixture here could be either tri-modal as shown in Figure 3-2 E, or unimodal but

flat and widely spread as shown in Figure 3-2 F. It is important to note here that, a

previous study[25] indicates that for the reason of hydrodynamic interaction of

moving particles at different electrophoretic mobility or known as electrokinetic

retardation and enhancement effect, distributions of cases shown in Figure 3-2 B

and C may shift a little towards each other from their original positions. When the

technique is applied to real systems, the results could be far more complicated

than what is provided in Figure 3-2, as more factors need to be taken into

consideration.

It has been proven in many studies that the zeta-potential distribution

analysis has huge potential in indentifying interaction behaviour and mechanism

of mixed systems[23, 24, 26, 37, 52, 53]. It has been successfully applied to the oil sands

field to determine the role of divalent cations in affecting bitumen-clay

interactions, and explain bitumen-clay interactions where clays were collected

from oil sands ore of different grades[23-26, 29, 52, 53].
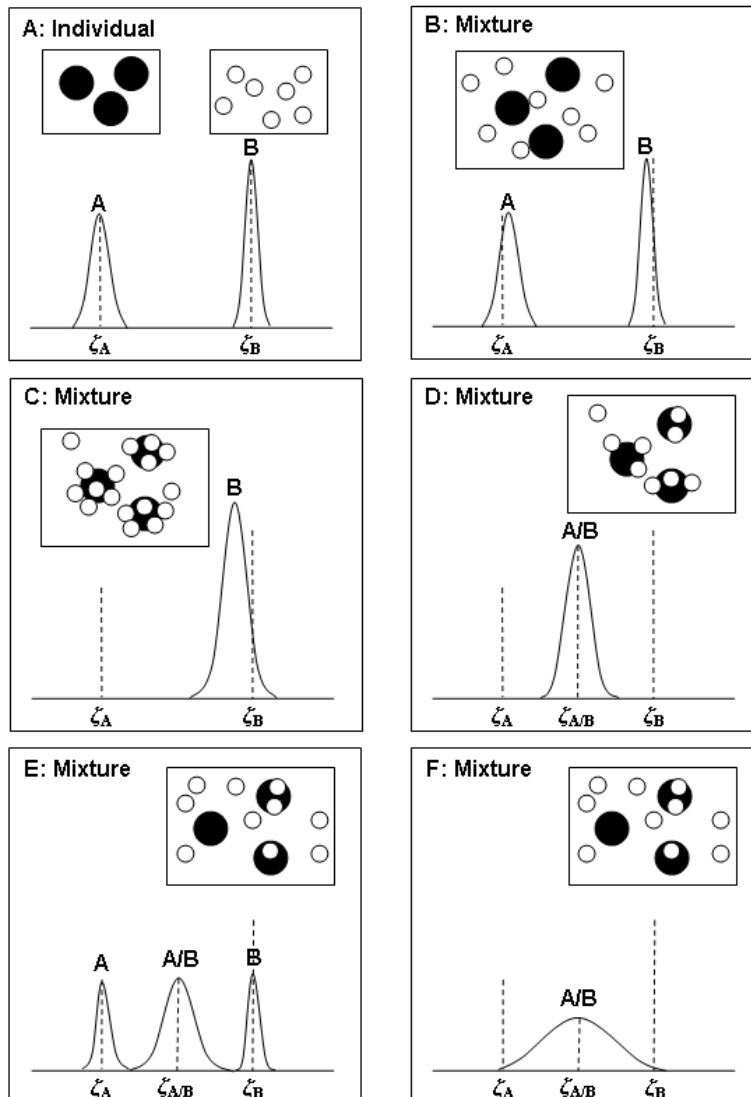
Figure 3-2: Schematic zeta-potential distributions for studying colloidal interactions in a binary mixture. A. Individual zeta-potential distributions of particles A and particles *B*; B. Binary mixture of the two colloidal suspensions without attachment; C. Strong attachment in a mixed system where particle *A* is fully coated by material *B*; D. Strong attachment in a mixed system where particle *B* is insufficient to covered particle *A*; E. & F. Weak attachment in a mixed system where only a small portion of *A* and *B* are attached to each other while a considerable amount of *A* and *B* remains freely suspended.

55

3.2.2   Experimental Apparatus

3.2.2.1 High Intensity Agitator

A high speed agitator (Ross corp., Model 100DLC) was used in this study
to create hydrodynamic cavitation by high intensity agitation (HIA) in a custom-
designed high intensity agitation cell (HIA cell). The high speed agitator has a
variable speed control from 500 ~ 10,000 rpm, and a power lift mechanism which
allows the position of the impeller to be adjusted vertically. The impeller used in
this study is a Rushton 2-blade impeller with a diameter of 5.7 cm and a blade
width of 1.2 cm, fabricated in the machine shop of Department of Chemical and
Materials Engineering.

3.2.2.3 High Intensity Agitation Cell

The custom-designed, vertically oriented cylindrical HIA cell has an inner
diameter of 7.6 cm, a wall thickness of 0.8 cm and 350 ml of capacity. It is made
of Plexiglas. Two "standard baffles", each with 9 symmetrically distributed pairs
of pores, are located axisymmetrically along the straight side of the inner cell wall
to prevent swirl and enhance the shear, providing desired mixing effect. The HIA
cell also has two sampling ports, one on the top, and the other near the bottom,
which could be connected to the zeta-potential measuring equipment with tubings
and a pump to improve sample transfer of the generated submicron size gas
bubbles suspensions for zeta-potential distribution measurements. Finally, the
most important part of the HIA cell is the lid designed in such a way that
entrainment of gas is minimized by filling up the cell without leaving any air gap.
Illustration of the high speed agitator and HIA cell is given in Figure 3-3.
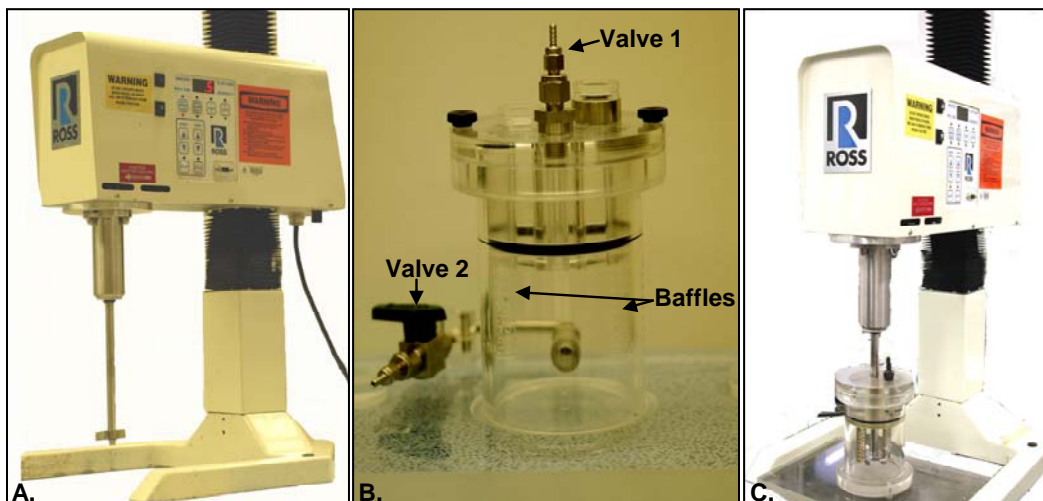
Figure 3-3: A. High speed agitator; B. HIA cell; C. Complete setup of submicron size gas bubble generation system.

3.2.2.2 ZetaPALS

ZetaPALS, a commercial instrument by Brookhaven Instruments Co. (NY, USA) is capable of accurately measuring size distributions of bubbles by its dynamic light scattering method[31]. And with its phase analysis light scattering (PALS) technique which has much greater sensitivity than conventional electrophoretic light scattering (ELS), ZetaPALS is not only feasible of measuring the zeta-potential of the more common colloidal systems, i.e. a solid or organic phase dispersed in an aqueous or organic phase, but it has also been successfully applied to zeta-potential measurements of nano size bubbles[31, 32]. Therefore ZetaPALS is used in this study to measure both the zeta-potential and size of submicron size bubbles.

3.2.2.3 Zetaphoremeter
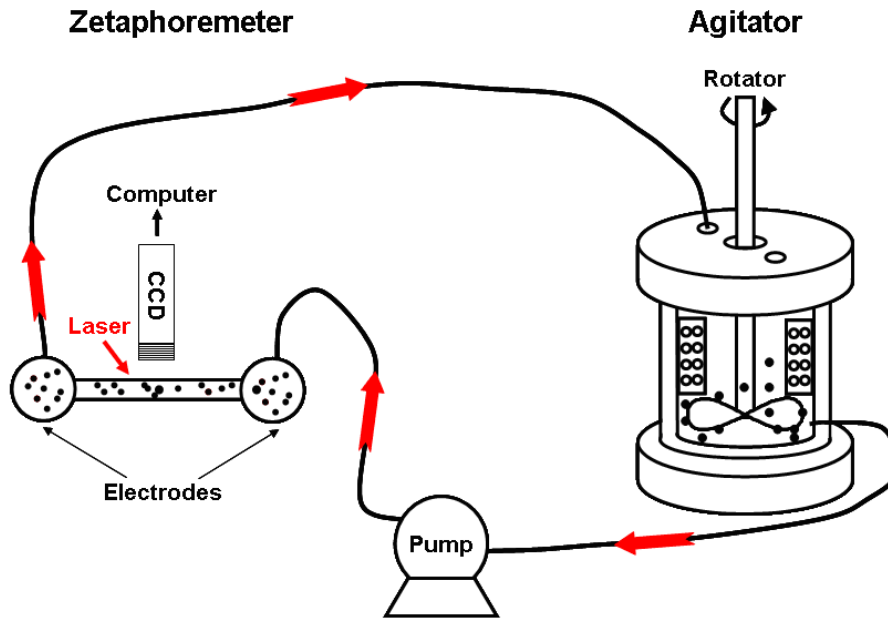
Figure 3-4: Schematic layout of connections between Zetaphoremeter, high speed agitator and HIA cell.

In this study, bubble-solid interactions are analyzed by Zetaphoremeter (CAD Instrumentation, Z3110) via its distinct zeta-potential distribution function. The operation principle of Zetaphoremeter is based on micro-electrophoresis— sample particles in a suspension move in a micro-electrophoresis cell under applied electric field. The particle/bubble movements are simultaneously captured by a CCD camera that is attached to the microscope, and analyzed by vendor-provided imaging analysis software on the computer connected to the instrument. In order to optimize the efficiency and operability of zeta-potential measurements of submicron size gas bubbles, Zetaphoremeter is connected to the submicron size bubble generation system through a peristaltic pump. To describe how each of the associated parts functions more clearly, the components and their role in the

experimental operation will be discussed in the experimental procedure section

(Section 3.3.4). A schematic layout of the connected system (Zetaphoremeter –

high speed agitator – HIA cell) is shown in Figure 3-4.

3.2.2.4 Denver Cell Laboratory Flotation

Denver cell is a batch processing unit for laboratory scale bitumen

extraction. Denver cell uses the corners of the cell as baffles while an agitator

with air supply is used to provide mechanical mixing and aeration to the oil sands

slurry. The aerated bitumen and hydrophobic fines are therefore carried by air

bubbles to the top of the cell leaving the unaerated solids and fugitive bitumen in

the cell. Figure 3-5 shows a schematic of Denver Cell flotation unit.
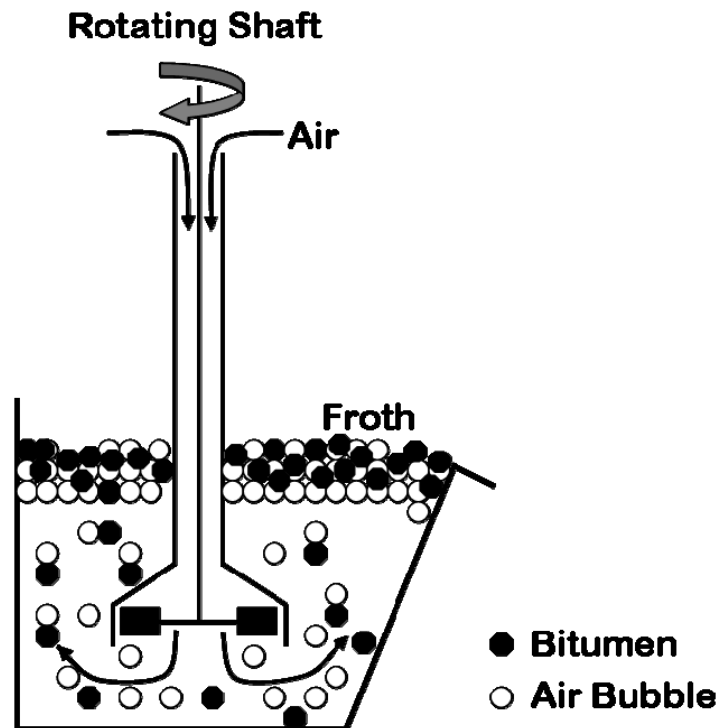
Figure 3-5: Denver Cell flotation unit.

3.3   Experimental Procedures

3.3.1   Submicron Size Gas Bubble Generation

Submicron size gas bubbles are generated in an aqueous environment with different water chemistry as a result of hydrodynamic cavitation caused by intensive agitation. The gas bubbles exist in the form of the dispersed phase in the colloidal suspension. Aqueous solutions with required chemical concentrations were prepared in such a way that contamination of fine particles such as dust and microorganisms were minimized (details provided in Section 3.1 and the following paragraph). The solutions used for submicron size bubble generation are shown in Table 3-3, where with the exception of the filtered process water (FPW), all other solutions were made on the basis of 1mM KCl which was used as supply of back ground electrolytes.

Table 3-3: Solutions tested for submicron size bubble generation.

Concentration (mM)	KCl	CaCl$_2$	SDS	DAH	FPW (A-I process water)
0.01			√		
0.1		√			N/A
1	√	√	√	√	
10		√		√	

A necessary amount of chemicals was weighed on a microbalance to prepare the needed stock solutions at a relatively higher concentration, which were diluted to the desirable concentrations. Milli-Q water was filtered with a 0.1μm pore size vacuum or syringe filter to remove larger particles before being used to prepare the solutions. Unless otherwise noted, the pH of all solutions for submicron size bubble generation was adjusted to pH 6.5 with either NaOH or

60

HCl both before and after agitation. The pH was monitored to ensure a consistent pH condition. The pH is chosen to be very close to the original pH of all aqueous solutions, thus limiting the need for pH adjustment and simplifying interpretation of results. The prepared solutions were filtered with the 0.1 μm-filters again prior to their use to avoid any possible contamination of solution by dust or precipitation.

In the case of FPW, the critical step in solution preparation is to remove a massive amount of fines—one of the major problems which need to be, but not yet handled by the oil sands industry[189-192]—that come with industrial process water. In order to clarify the applied process water as much as possible, process water was left to settle for at least 8 weeks, after which the bottom part of the process water was discarded. The relatively clear upper part of the process water was first centrifuged with a high-speed centrifuge (Sorvall RC6PLUS, Thermo Electron Corporation) at 12000 g for 30 min. The supernatant after centrifuge was carefully taken out without disturbing the sedimentation of fine clay at the bottom of the centrifuge tubes. The centrifuged process water was filtered with 0.1 μm pore size vacuum or syringe filters before storage and filtered again with the same kind of filters before its use.

Gas saturation is known to greatly facilitate bubble generation efficiency[32, 130, 193]. To confirm this statement, another group of the prepared solutions were placed in a thermally controlled water bath (Neslab RTE7, Thermo Electron Corporation) which remained at 8 ℃ while the solution was being saturated with tanked air and CO_2 (Praxair) through an air stone for 24 hr at the

same regulated outlet pressure of 200 atm. Bubble generation results of such solutions were compared with solutions without air/CO_2 saturation. The solutions more capable of generating submicron size bubbles were used in the subsequent study of bubble-particle interactions.

Before agitation, the HIA cell was filled with approximately 350 ml of the prepared solutions all the way to its opening, with a water level parallel to the surface of the cell lid, leaving no gap for air to be entrained during the agitation. The cell lid was then tightened with two screws and sealed with several gasket rings to assure air leak tightness. The impeller shaft was aligned to the center of the opening and made sure not to touch any part of the wall during high-speed agitation. If necessary, the HIA cell was fixed to position as the cell tended to shift when the mechanical force of agitation got too server. The high speed agitator was first set to agitate for a given duration at different agitation speed (from 500 rpm to 3500 rpm with an increment of 500 rpm) to examine the role of agitation speed in bubble generation; and then set at certain agitation speed for different agitation time of 10, 20, 30 and 40 minutes, to study the impact of agitation time. In both cases, the initial and final temperature of the systems (aqueous suspensions) was recorded for reference. Finally, the effect of temperature on submicron size bubble generation was studied by varying the initial temperature of the solutions, while allowing them to agitate at identical speed for the same amount of time.

3.3.2   ZetaPALS Particle Sizing and Zeta-Potential Measurements

Size of the submicron size gas bubbles was measured using a ZetaPALS after bubble generation. Approximately 50 ml of the HIA agitated solution (bubble suspension) was collected into a beaker through the valve located at the bottom of the HIA cell. The pH of the suspension was measured and, if necessary, adjusted to pH 6.5 with either NaOH or HCl. As the temperature of the solutions used to generate bubbles was found to increase from 24 ºC to 75 ºC with increasing agitation time and speed, the gathered bubble suspension was set aside to cool for 30 min before the bubble size measurements. For each measurement, $2 \sim 3$ ml of the gathered solution was placed in a cuvette, which was then placed in the sample chamber of ZetaPALS. Unless otherwise noted, all of the bubble size measurements were conducted at room temperature by setting the temperature of ZetaPALS to 25 ºC, and repeated at least 3 times for each individual sample by refilling the cuvette with fresh sample from the beaker.

To measure the size of the SiO_2, Al_2O_3 and carbon black particles in an aqueous colloidal suspension, a suspension of much higher concentration was made in advance by adding the nano powders (weighed to the same amount in mole) with about 60 ml of 1 mM KCl or 0.1 mM DF250 + 1 mM KCl solution into a beaker. To break down the large lumps of aggregated nano particles and disperse them uniformly through out the solution, the suspension was left in an ultrasonic bath (275DA, Crest Ultrasonic) at power lever 9 for 15 min. After sonication, the suspension was allowed to settle for 15 min. Several drops of the supernatant were then diluted into 50 ml solutions of the same chemistry as those

used for preparation of the concentrated particle suspensions. The diluted

suspension was mixed with a magnetic stirrer. The pH of the diluted suspension

was then measured and adjusted. As for the case of Posyn fines, the preparation

of sample for particle size measurement was quite different. Posyn ore was first

placed in Denver Cell with A-II process water. After flotation, the resulting

tailings water was gathered. Since we were only interested in particles of very

small sizes in this work, we do not need any of the coarse solids in the tailings

water. For this reson, the tailings water was either centrifuged (CF) or allowed to

settle down (SF) for several days. The supernatant was collected as source of clay

particles. Fines from bitumen froth was also collected and suspended in

corresponding tailings water. More details on this subject will be described later

in this thesis. When the particle and fines suspensions were ready, particle size of

the suspended SiO_2, Al_2O_3, carbon black and fines was measured by ZetaPALS

using the same procedure as applied to gas bubbles suspensions described above.

The average diameters of the particles used in this study are given in Table 3-4.

Since ZetaPALS is also capable of measuring the zeta-potential of

particles, droplets and bubbles, ZetaPALS was used for zeta-potential

measurements to study the stability and properties of the generated submicron

size bubbles. This is particularly useful for single component systems in which

conditions are not suitable for Zetaphoremeter due to its principle and design. The

suspensions that were used for particle size distribution measurement were used

for zeta-potential measurement. As measuring the zeta-potential would require an

applied electric field, a pair of palladium-coated electrode were fully immersed in

the sample suspensions in the measurement cuvette. The measurement

temperature was also set at 25 ºC. Each data was an average of at least 3 repeated

measurements of refilling the cuvette with fresh samples. In order to study the

stability of the generated bubbles, both the size and zeta-potential of the sample

were measured at increasing intervals for several hours to up to 24 hours

depending on the life time of the submicron size bubbles.

Table 3-4: Particle size of fine SiO_2, Al_2O_3 and clay particles in suspensions.

	SiO_2		Al_2O_3		Posyn CF & SF	Posyn FF	Carbon Black
	Nano	Micron	Nano	Micron			
Diameter (nm)	668.9	939.3	533.5	868.1	464.4	778.6	295.9
Standard Deviation (nm)	14.4	162.6	22.1	114.7	34.3	35.5	30.9
Polydispersity	0.25	0.32	0.29	0.32	0.26	0.27	0.20
Solution	1mM KCl				Tailings Water		0.1 mM DF250 & 1 mM KCl

3.3.3   Correlation of Particle Number (Population) and ZetaPALS Count Rate

In particle size measurement using ZetaPALS, the instrument provides an

output called particle count rate in kilo counts per second (kcps). This feature of

ZetaPALS allows us to quantify the number or the local concentration of bubbles

in each sample and hence study the generation of submicron size bubbles by HIA.

To do this, it is important to establish a correlation between the number of

particles and corresponding count rate. For the purpose of applying ZetaPALS to

determining the actual number of submicron size bubbles, a calibration was

needed to relate the number of particles in the suspension and the measured count rates. The measurements were therefore conducted using standard silica nano particles in Milli-Q water of different suspension concentrations. The standard silica suspensions were prepared by sonicating the mixture of powder and solution in a beaker for 15 min using a sonicater bath. The measurements were performed immediately after sonication in attempt to avoid sedimentation of larger particles. With a simple calculation of $N = \dfrac{M/\rho}{V}$, the mass of silica powder in suspension was converted to the number of silica particles, where N is the number of particles, M is the mass silica powder , ρ is the density of silica and V is the average spherical volume of a single silica particle.
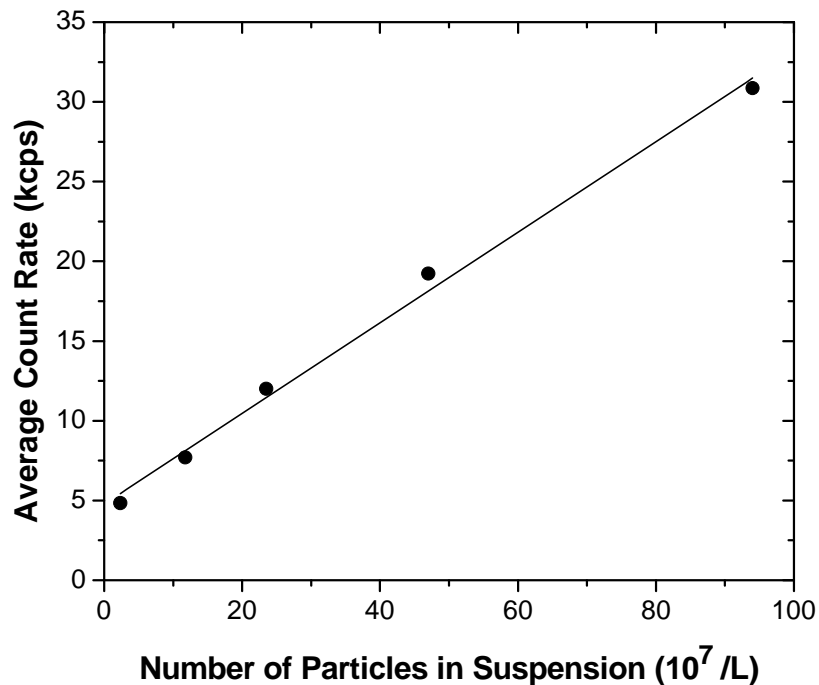
Figure 3-6: Relationship between the count rate readout on ZetaPALS and the number of silica particles suspended in Milli-Q water.

Over the particle concentration range studied, the results in Figure 3-6 clearly show a linear correlation between the count rate from ZetaPALS and the number of silica particles in suspensions: a higher count rate corresponding to a larger number of particles. We can therefore conclude that the count rate from ZetaPALS could serve as a semiquantitative measurement of number of particles or bubbles in a suspension.

3.3.4 Zeta-Potential Distribution Measurements

Bubble-solid interaction or attachment was investigated in this study through zeta-potential distribution analysis of submicron size gas bubbles, solid particles and the mixture of the two using a Zetaphoremeter. To study the effect of existence of solid particles on bubbles generation and *in situ* gas nucleation during bubble generation, two experimental procedures were adopted—one, mixing after bubble generation known as mixing process or attachment process, and the other, bubble generation/agitation in the presence of particles, know as *in situ* gas nucleation process.

3.3.4.1 Mixing of Submicron Size Bubbles and Solid Particles after Bubble Generation (Mixing/Attachment Process)

In order to obtain the zeta-potential distribution of gas bubbles alone, solutions were first saturated with air at 8 ºC for 24 hr to enhance bubble generation. The submicron size gas bubbles were generated in the same way as described in Section 3.3.1 but at a fixed agitation speed of 2200 rpm and agitation time of 40 min. The bubble suspension produced was left in the HIA cell to cool

down for at least 30 min while its pH was measured and adjusted. The suspension was then pumped into the rectangular quartz micro-electrophoresis cell of Zetaphoremeter, which was inserted between a pair of palladium-coated electrodes. A laser illuminator was used as the optical light source for light refraction of the suspended bubbles within the stationary layer. The stationary layer was verified by the custom-programmed software on notification of detecting a sensor located on the table of microscope sample holder. The CCD camera mounted on top of the microscope above the quartz cell recorded the movement of particles within the cell and displayed it on the computer screen. An electric field was applied to the cell upon click of the control button of the software after no visible rising of bubbles in the cell was observed. The movements of 20 ~ 100 bubbles in the view were tracked. The direction of electric field was reversed after tracking the bubbles in ten consecutive time intervals, causing the bubbles to move towards the opposite directions. The movement of particles was traced again in the same way. The circuit was then switched off. The images captured by the CCD camera were sent to the computer and analyzed by the image analysis software, which converted the various velocities of different particles into electrophoretic mobility and further into zeta-potential using the Smoluchowski equation[194]. With all the mobility or zeta-potential being calculated, the software offered a mobility/zeta-potential distribution histogram with mobility/zeta-potential as X-axis and the occurrence frequency of particles of the corresponding mobility/zeta-potential, shown in percentage, as Y-axis. Each sample was measured for at least 5 times by replacing

the suspension in the quartz cell with a fresh sample in the HIA cell. The

measurement was repeated as described above. The number of bubbles that had

been under observation was given as "tracking number". The tracking number of

the observed bubbles was recorded for each measurement and used as a measure

of component population during mixing of bubbles with solid particles.

For the situation of particle suspensions, the suspensions were pretty

much prepared in the same manner as stated in particle size measurements, except

that the volume of the concentrated solution drawn for dilution was controlled so

that the tracking numbers of the measured particles were controlled within the

same range as those of the bubbles. The diluted particle suspensions were then

used to fill the quartz cell through a plastic tube of which one end was attach to an

end of the quartz cell while the other immersed in the suspension. A syringe

attached to one end of another tube whose other end was attached to the second

end of the quartz cell was used to draw the samples. The zeta-potential of

particles was measured in the same way as for bubbles. As zeta-potential is more

commonly mentioned in literature when studying the surface charge of particles[53,
83, 84, 187, 188, 195], we hereby use the zeta-potential distribution histogram instead of

the mobility distribution histogram for studying bubble-particle interactions.

After measuring the zeta-potential of bubbles and particles individually,

the bubble suspension and particle suspension were mixed together to study their

interactions. As noted above, the tracking number of bubbles and particles were

recorded for each measurement and thereby an average tracking number was

acquired on basis of at least five measurements for each suspension to make sure

that number of the bubbles and particles in the respective suspensions was almost the same. In this manner, the bubble suspension and particle suspension mixed at a 1:1 volume ratio would ensure similar number of bubbles and particles in the mixture. The mixture suspension was agitated with a magnetic stirrer for 30 min before the zeta-potential distribution of the mixture was measured in the same manner as that of a single component particle or bubble suspension.

For single component suspensions of bubbles or particles, the zeta-potential was first measured as a function of pH ranging from pH 2.1 ~ pH 11.0 to determine the isoelectric point (iep) of the particle and bubbles in corresponding aqueous environment. From measured iep of pH = 2, pH 2.1, 4.0 and 6.5 were selected for mixtures involving negatively charged silica particles. For the similar reason, pH 6.5, 9.8 and 11.0 where chosen for mixtures contenting positively charged alumina particles, as the iep of alumina is determined around pH 9[187, 188]. Zeta-potential distributions of bubbles and particles were first measured individually at the selected pHs. The zeta-potential distribution of a binary mixture of bubble and solid particles was then measured at the same pH. For bubble generation, the pH of the solution (which became bubbles suspension later) was measured and adjusted before and after agitation. For particle suspension, pH was adjusted after the concentrated suspension was diluted. For mixtures, pH was adjusted both at the beginning and end of mixing of the two components. The pHs of all samples were monitored until they were drawn into the quartz cell for zeta-potential distribution measurement. For all the zeta-potential measurements,

both the zeta-potential distribution histograms and the average zeta-potential values were recorded.

3.3.4.2 Mixing of Submicron Size Bubbles and Solid Particles before Bubble Generation (*In Situ* Gas Nucleation)

It has long been discussed that existence of solid particles in a system somewhat alters the bubble generation process[51, 130, 141]. To study whether solid particles during HIA influence bubble generation or in other words, change bubble-solid interactions, a group of experiment was designed. In this process, a small amount of solid particles was added to the bubble generation solution before HIA. The tracking numbers of particles during several (≥ 3) zeta-potential measurements at a given pH were recorded and their average value was taken. Similarly, the average tracking numbers of at least three independently generated bubbles suspensions were determined during zeta-potential measurements. The concentrated particle suspension was then diluted into the air/CO_2 saturated bubble generation solutions according to volume ratio so that the number of particles was similar to the anticipated number of bubbles that would be generated. The pH of the resulting bubble generation solution was adjusted to same value as the concentrated particle suspension used for dilution. The particle suspension was then injected into the HIA cell where bubbles were generated at 2200 rpm agitation for 40 min. The resulting suspension should be a mixture of solid particles and bubbles either attached to each other or freely suspended. Such suspension was agitated with a magnetic stirrer for pH measurement (monitoring and amendments). After cooling for 30 min with stirring of the magnetic stirrer

71

(same as that mentioned in the mixing/attachment process), the mixture was drawn into the quartz cell for zeta-potential distribution measurements.

3.3.4.3 Bubble Particle Ratio in a Mixture

The procedure to mix the bubble and particle suspensions was based on the tracking number of zeta-potential distribution measurement using single component sample. However the tracking number does not represent the real number of bubbles/particles in a suspension. This is attributed to the design of Zetaphoremeter and limited sensitivity of the instrument in distinguishing the bubbles/particles. In general, the real number of bubbles/and particles were cut down by a large factor. For practical purpose, however, it is still the best way to control the number of bubbles and particles in a mixture on a same level. As long as the tracking number and size of the bubbles/particles being measured are similar and fit the requirements of the instrument, the results still serve the purpose of determining the interactions between particles and bubbles.

3.3.5   *Laboratory Denver Cell Flotation*

Posyn oil sands ore is a high fines ore and was used in this study to study bubble-solid interactions in a simulated bitumen flotation system. Denver flotation cell was connected to a thermally controlled water bath to maintain a flotation temperature of 35 ºC. Prior to flotation test, 950 ml of A-II process water was placed in a beaker and the pH was adjusted to pH 8.5. The water was heated to 35 ºC, identical to the temperature of flotation. 330 g of Posyn ore was weighed and placed directly into the flotation cell followed by the addition of heated

72

process water. Denver cell was then turned on to mix and condition the ore in the

process water at an agitation rate of 1500 rpm for 5 min. During the conditioning

of the slurry, the pH was measured and adjusted to remain at pH 8.5. After 5 min

of conditioning, air was introduced to the system at a flow rate of 150 ml/min.

The flotation process continued for 1 hr during which the froth was collected to

another container as soon as it was produced. The tailings water was obtained in

the form of fines suspension after removal of coarse solids by settling. The clear

supernatant after centrifugation and filtration was used for bubble generation and

zeta-potential distribution measurements. The collected froth was cleaned by

Dean stark to remove the bitumen from the hydrophobic fine clay particles in

froth. Such fines (mostly clay particles) were also used to study bubble-particle

interactions.

Chapter 4 Generation and Properties of Submicron Size Bubbles

4.1 Generation of Submicron Size Bubbles

4.1.1 Effect of Agitation Speed on Submicron Size Bubble Generation

Generation of submicron size bubbles is a challenging task. During the past few decades, several methods have been proven to be successful in accomplishing this goal[31-33, 59, 70, 130, 144]. HIA is considered to be a promising candidate[59, 70]. Even though there were direct and indirect evidence that HIA is capable of generating bubbles less than several microns[59, 70], understanding the process itself is still at a primitive state. One of the main focuses of this study is to further understand the mechanism of bubble generation by HIA effect of process parameters, such as agitation speed, agitation time and process temperature on bubble generation.

Aqueous solutions of 1 mM KCl, 1 mM SDS + 1 mM KCl and FPW were prepared using procedures described in Chapter 3. Submicron size bubbles were generated through HIA as a function of agitation speed starting from 500 rpm to 3500 rpm with a fixed agitation time of 30 min. The effect of agitation speed on bubble generation in different solutions is shown in Figure 4-1 ~ Figure 4-3.

The results in Figure 4-1 show that when generated in 1 mM KCl solution, the average bubble diameters decreased whereas the population of bubbles increased with increasing agitation speed. This finding is not unexpected as we

74

would anticipate an increased hydrodynamic cavitation and expanded bubble generation zone with increasing agitation speed. Another obvious fact shown in Figure 4-1 is a dramatic decrease, from 821 nm to 364 nm, in the size of bubbles generated when the agitation speed increased from 500 rpm to 2000 rpm, along with an increase in the population of bubbles from 16 kcps to 54 kcps after agitation speed exceeds 2500 rpm. The results clearly show that increasing agitation speed is advantageous for generation of stable submicron size bubbles in 1mM KCl solution.
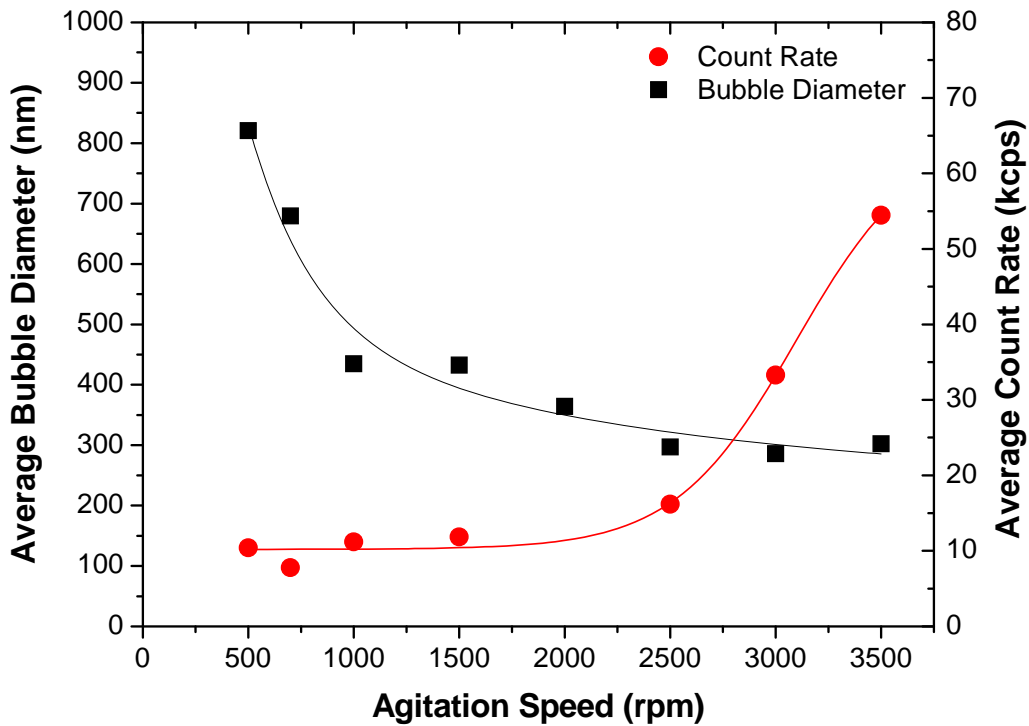
Figure 4-1: Effect of agitation speed on generation of submicron size bubbles in 1 mM KCl solutions of pH 6.0. The agitation time was fixed at 30 min.
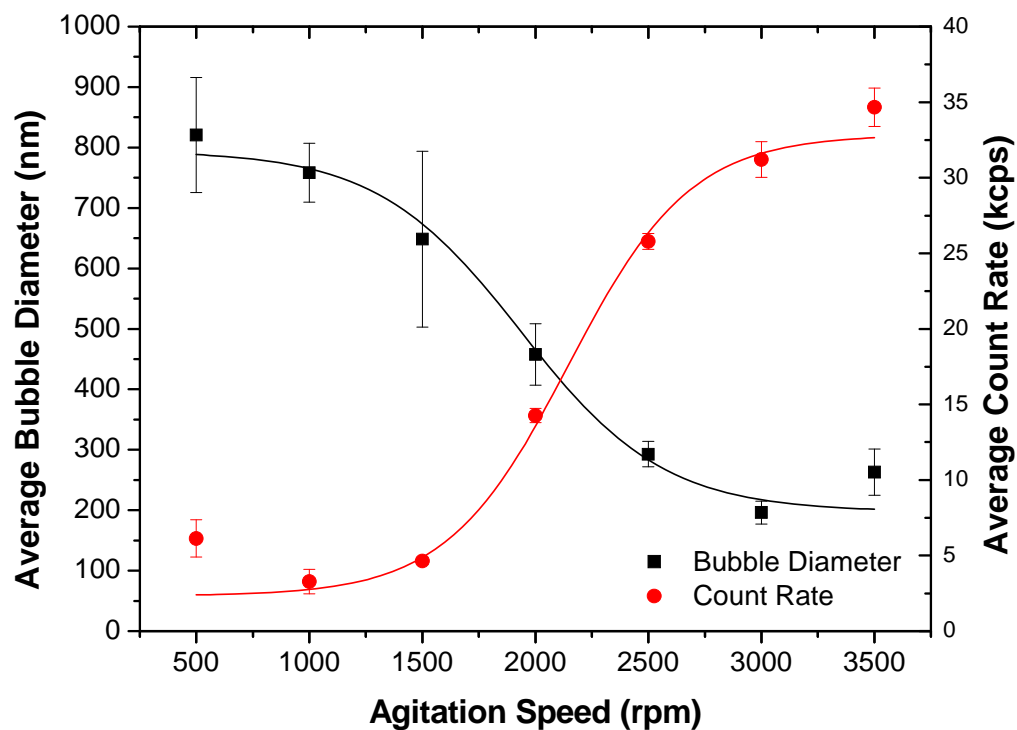
Figure 4-2: Effect of agitation speed on generation of submicron size bubbles in 1 mM SDS + 1 mM KCl solutions of pH 6.0. The agitation time was fixed at 30 min.

As shown in Figure 4-2, bubble generation in 1mM SDS solution with 1 mM KCl was also influenced by agitation speed. The trend here pretty much simulates the pattern seen in Figure 4-1, that is decreasing bubble size and increasing bubble population with increasing agitation speed. The average diameter of the bubbles decreased from 820 nm to approximately 200 nm, and the count rate increased by almost 14 times when the agitation speed increased, from 500 rpm to 3500 rpm. SDS has been found to assist the bubble generation by lowering the surface tension of the aqueous phase and protecting the generated bubbles from coalescence[31]. Thus, it is reasonable to find smaller and more

stabilized bubbles in a SDS solution due to limited bubble coalescence and growth. However, it is important to note here that even though the average count rate implies the number of bubbles generated in a solution, it is still better to keep the comparison of bubble population within the same group of experiments performed under the same condition. From the results provided in Figure 4-2, it is still evident that agitation speed above 2500 rpm remains effective for bubble generation in 1 mM SDS solutions.
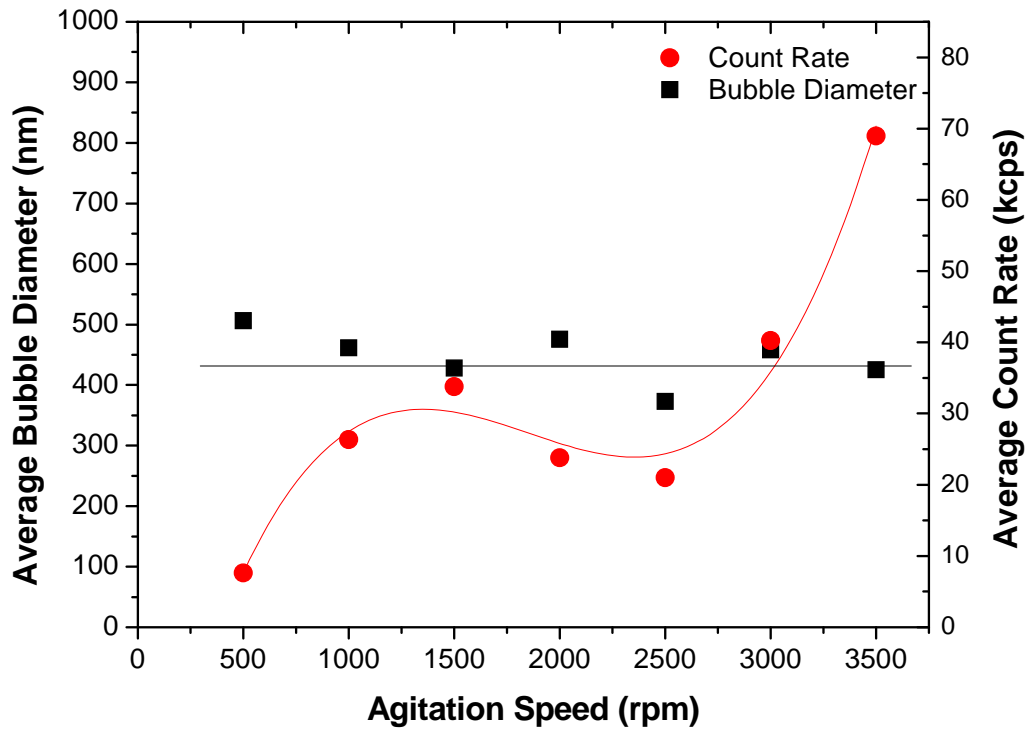
Figure 4-3: Effect of agitation speed on generation of submicron size bubbles in FPW of pH 8.5. The agitation time was fixed at 30 min.

The results in Figure 4-3 show that generation of bubbles in FPW is rather different from bubble generation in simple electrolyte or surfactant solutions. When the agitation speed increases from 500 rpm to 3500 rpm, the size of the

bubbles remained constant at around 400 nm although there is a clear increase in population of bubbles at agitation speed above 2500 rpm. The different bubble generation pattern in FPW reflects complex nature of FPW water chemistry, such as high ion concentration and considerable amount of different natural surfactants[5, 16].

From results discussed here, it can be concluded that increasing the agitation speed generates more and smaller bubbles, which facilitates studying the physicochemical properties of the bubbles and bubble-solid interactions. Based on this conclusion, agitation speed around 2500 rpm should be applied to bubble-solid interaction experiments in this work.

4.1.2   *Effect of Agitation Time on Submicron Size Bubble Generation*

The effect of agitation time on submicron size bubble generation in 1 mM SDS + 1 m M KCl solution at 2000 rpm is shown in Figure 4-4. Although there is a slight decrease in bubble diameter from 600 nm to 500 nm with increasing agitation time from 10 min to 30 min, the agitation time at 2000 rpm has a negligible effect on the number of bubbles generated, as shown by a relatively constant count rate. It is possible that at such high agitation speed, the gas nucleation occurs within a relatively short period. The observed decrease in bubble diameter with agitation time could be attributed to shrinkage of bubbles by gas dissolution in solution. Further investigation is, however needed, to further confirm this mechanism by conducting experiments at both lower and higher agitation speeds.

78
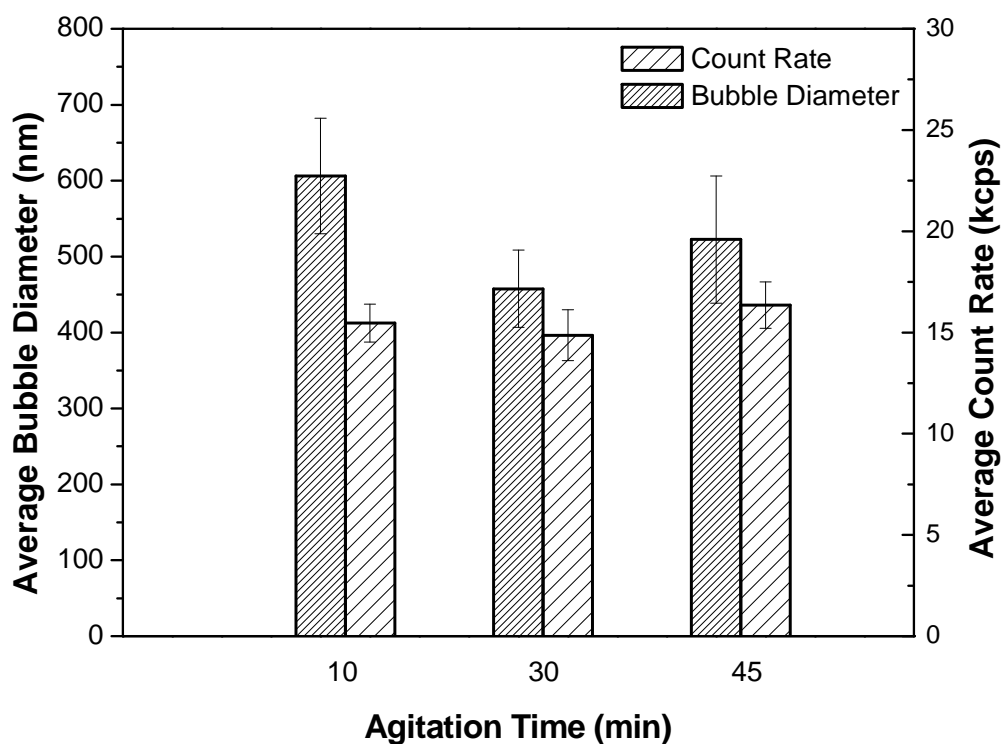
Figure 4-4: Effect of agitation time on generation of submicron size bubbles in 1 mM SDS + 1 mM KCl solutions of pH 6.0. The agitation speed was fixed at 2000 rpm.

4.1.3 Effect of Temperature on Submicron Size Bubble Generation

During the experiments, solution temperature was found to creep up by agitation with the heating rate depending on the speed of agitation. As shown in Figure 4-5, a maximum difference of more than 50 ℃ (from 24 ℃ to 78 ℃) was determined when the agitation speed was at 3500 rpm. The results in Figure 4-5 also show that the temperature of solution increased almost linearly with increasing agitation speed with a single slope independent of solution chemistry. Temperature is known to play an important role in changing the dissolved gas

content, fluid viscosity and density of an aqueous solution. All these changes could have a considerable impact on bubble generation by hydrodynamic cavitation/gas nucleation[32, 70, 130]. A change in temperature could also affect coalescence of the generated bubbles[196], which is also critical to generation of submicron size bubbles. For these reasons, temperature is highly likely to impact bubble generation. It would therefore be important to study the influence of temperature on bubble generation by hydrodynamic cavitation.
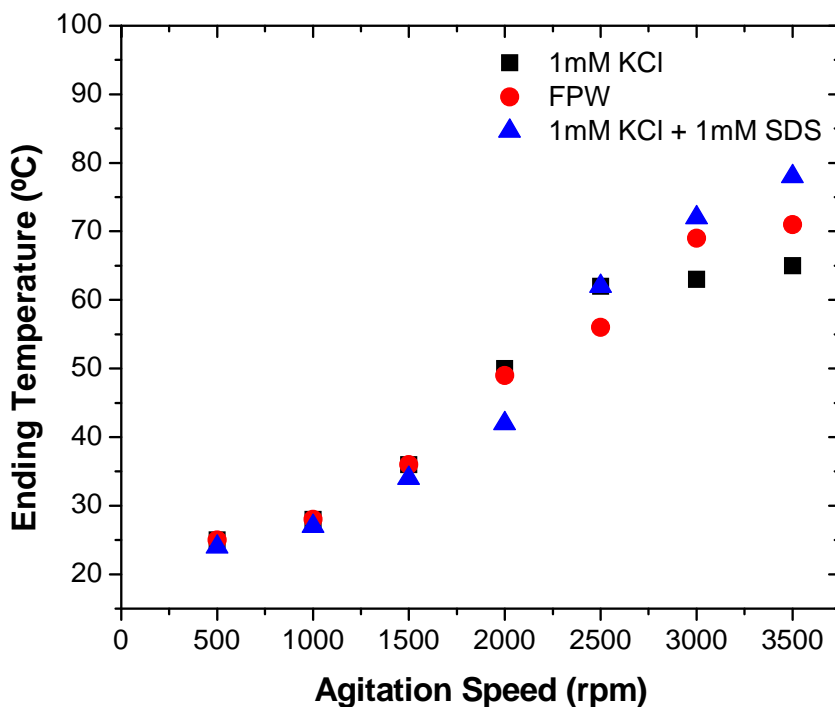
Figure 4-5: Increase in temperature during HIA as a function of agitation speed. The agitation time was fixed at 30 min.

To study the effect of temperature on submicron size bubble generation, two sets of experiments were conducted in two different solutions at different agitation speeds. Figure 4-6 shows that at a fixed agitation speed of 2000 rpm,

when the final temperature of the bubble generation solution after HIA increased

from 50 ℃ to 72 ℃, the average bubble count rate increased from 14.3 kcps to

33.5 kcps. At the same time, the average bubble diameter also increased from

458 nm to 701 nm. This finding indicates the expansion of bubbles. When the

final temperature of the solutions increased from 50 ℃ to 72 ℃, the process may

have reached condition of homogeneous gas nucleation, or more commonly

called—boiling[112], which led to formation of larger and unstable bubbles.

However when the temperature remained at around 70 ℃ while the agitation

speed increased from 2000 rpm to 3000 rpm, the average count reached a constant

value of around 32 kcps while the average bubble diameter dramatically

decreased to 196 nm. This result agrees with our previous observation that

increasing agitation speed caused an increased count rate and a decreased bubble

diameter. It appears that increasing agitation speed by 1000 rpm (from 2000 to

3000 rpm) limited the growth of bubbles in size as a result of increased shear

and/or overall temperature. However, the count rate of the bubbles remained the

same. The limited number and decreased size of bubbles with increasing agitation

speed above 2000 rpm are attributed to the decreased gas content in solution with

increasing solution temperature, which needs further investigation.

Figure 4-7 shows the effect of temperature on generation of submicron

size bubbles in FPW at a much lower agitation speed of 500 rpm. In this case, the

increase in final solution temperature from 24 ℃ to 50 ℃ led to a small decrease

in average bubble diameter from 455 nm to 401 nm. Although the bubble

population increased slightly with increasing temperature, the total amount of

bubbles generated at 500 rpm is, in general, small. According to Figure 4-5, the final temperature for agitation at 2000 rpm was 48 ºC. To study the effect of temperature on submicron size bubble generation and recognizing small increase in temperature by agitation at 500 rpm, the tests were performed using water of 50 ºC at 500 rpm for comparison. Figure 4-7 shows that although at the same final temperature, increasing agitation speed from 500 rpm to 2000 rpm doubled the population of bubbles while the average diameter of bubbles remained the same. This finding is in good agreement with the former results of FPW, which showed increase of bubble population with agitation speed without significant change in bubble diameter. Hence, for the case of FPW, although neither the agitation speed nor the final solution temperature seemed to have an effect on bubble size, both parameters played a role in determining the bubble population.

There appears to be two mixing regimes of below 2000 rpm and between 2000 rpm to 3000 rpm. In all three cases of electrolyte solution, surfactant solution and FPW, increasing agitation speed from 500 rpm to 2000 rpm led to increase of solution temperature from 24 ºC to around 50 ºC where such increase had little impact on bubble generation. Bubble generation results within this regime showed that agitation speed had small influence on the average count rate of generated bubbles as the count rate was generally low, but greatly affected the size of the generated bubbles (i.e. bubble size dramatically decreased with increasing agitation speed) with the exception of FPW where size of bubbles remained constant at all agitation speeds. When the agitation speed was increased from 2000 rpm to 3000 rpm for all three solutions, the temperature of the

solutions increased from around 50 ºC to up to 80 ºC. The effect of the increasing

temperature on bubble generation became obvious as increasing temperature

resulted in increase in both number and size of bubbles generated. Within the

regime of 2000 rpm ~ 3000 rpm of agitation speed, the average count rate of

generated bubbles significantly increased while the size of bubbles suddenly

decreased to around 300 nm ~ 400 nm and remained considerably constant

(except for the case of FPW) with increasing agitation speed. The reason for such

division remains to be further investigated.
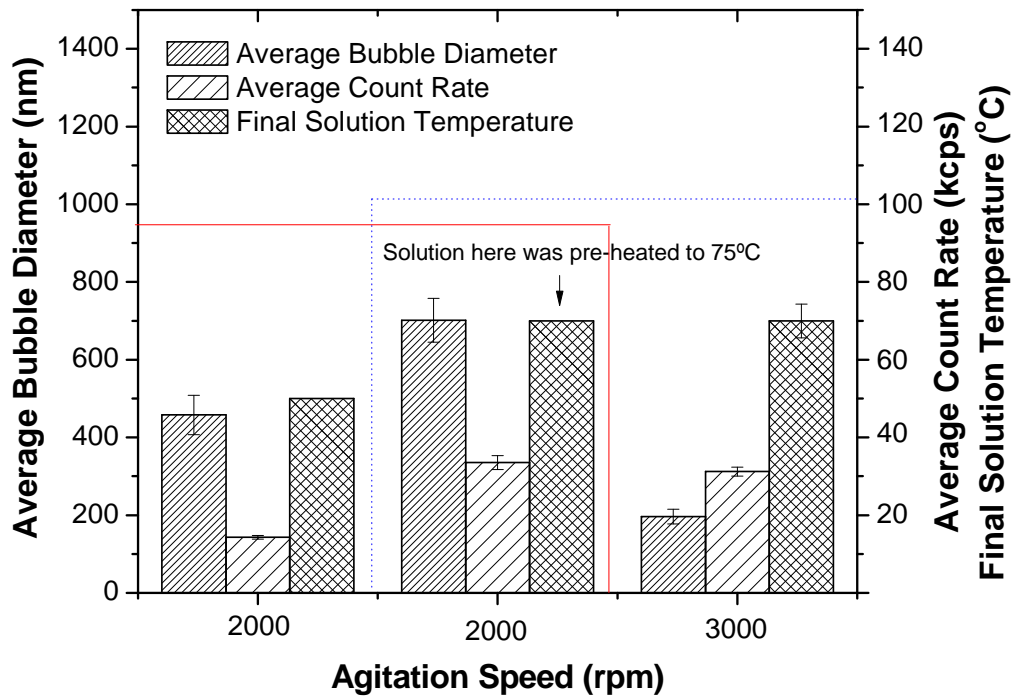
Figure 4-6: Effect of temperature on generation of submicron size bubbles in

1 mM SDS + 1 mM KCl solutions by 30 min of HIA at their original pHs.
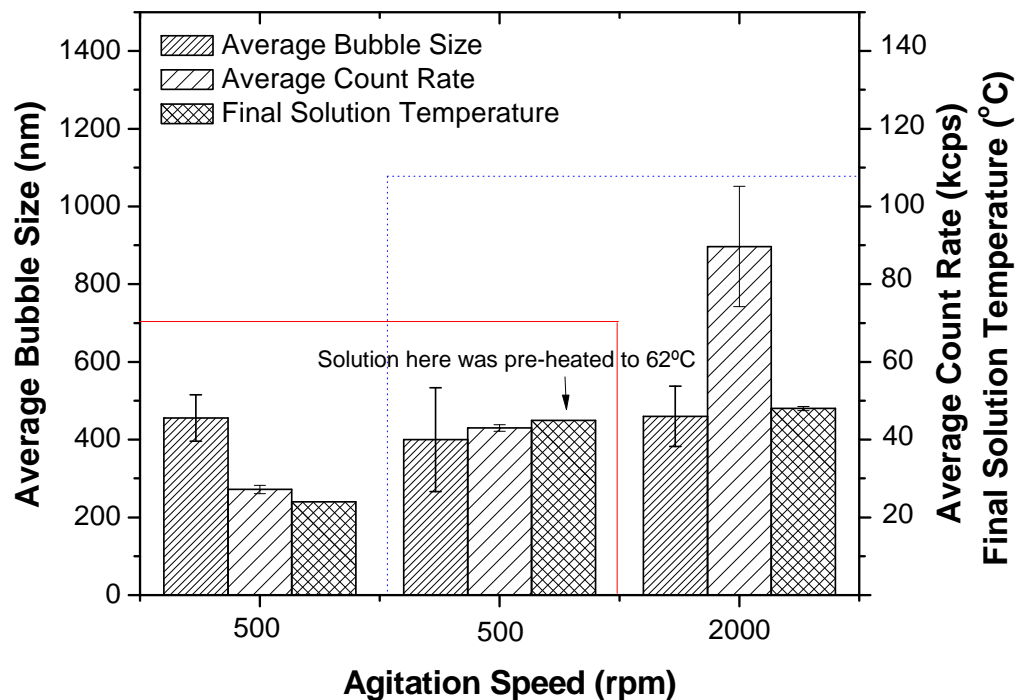
Figure 4-7: Effect of temperature on generation of submicron size bubbles in FPW by 30 min of HIA at their original pHs.

To fully understand how temperature influences bubble generation, further and more precise experiments should be designed and carried out. Due to the limitation of time and design of the current system, further experiments on temperature effect were not included in this study.

4.2   Properties of Submicron Size Bubbles

4.2.1   Zeta-Potential of Submicron Size Bubbles in Different Solutions

Zeta-potential is one of the most commonly examined properties of bubbles. Great effort has been devoted to this aspect during the past few decades[31, 32, 79, 145, 197]. It has been well accepted that air bubbles in deionized water bare

negative surface charge, while in most cases this charge is easily influenced by

such parameters as electrolyte concentration and pH[31, 32, 75, 78, 145, 198]. As

mentioned previously, submicron size bubbles generated via HIA is most likely a

mixture of water vapour and naturally dissolved gas[70, 112, 113, 120, 193, 199], so it is

logical to infer that these submicron size bubbles should have a similar

zeta-potential as that of air bubbles. In this part, we will discuss the zeta-potential

of submicron size bubbles generated in different solutions as a function of pH.
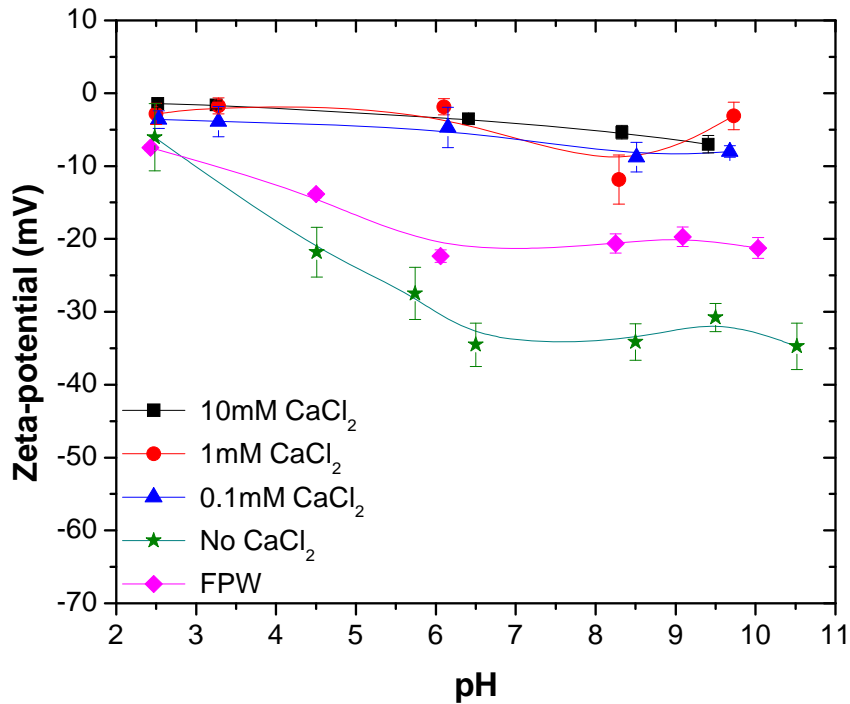
Figure 4-8: Effect of pH on zeta-potential of submicron size bubbles in various

CaCl$_2$ solutions containing 1 mM KCl and FPW, measured by ZetaPALS.

As shown in Figure 4-8, zeta-potential of submicron size bubble in 1 mM

KCl solutions changed from -6 mV to -35 mV when pH of the solutions increased

from 2.5 to 10.5. These values are very similar to zeta-potential data of air

bubbles in 1 mM KCl solutions reported by Cho *et al*. (2005) and Elmahdy *et al*. (2008). The reason for this increasing negative value of zeta-potential with alkaline addition is attributed to the excessive amount of OH^- in the aqueous system. OH^- groups are known to adsorb to the gas-water interface, bringing the zeta-potential to a more negative value. With the addition of 0.1 mM Ca^{2+}, the zeta-potential of the submicron size bubbles shifted to -4 mV ~ -9 mV within over a wide pH range of 2.5 to 10. Ca^{2+}, as described in Section 2.3.2, is considered as a specific adsorbing ion which could significantly alter the zeta-potential of bubbles. However, it is interesting to note that, when the concentration of Ca^{2+} further increased to 1 mM and 10 mM, the corresponding change in zeta-potential of bubbles was minor. It appears that at 1 mM Ca^{2+} concentration, Ca^{2+} was already in excess to cover all bubble surfaces. The redundant amount of Ca^{2+} at higher concentrations would only compress the electrical double layer, affecting zeta-potential to a comparably smaller extent. Another point to note is that, in the presence of Ca^{2+}, pH no longer has an obvious effect on zeta-potential of bubbles although a tendency for zeta-potential to become more negative with increasing pH remains visible. This finding agrees with results reported by Han *et al*. (2004) where they also found that within a pH range of 2 ~ 9, the effect of pH and further addition of Ca^{2+} from 0.1 mM to 1 mM on zeta-potential was insignificant in solutions already with Ca^{2+} concentration.

According to the results listed in Table 4-1, neither the temperature nor the agitation speed seemed to have an effect on the surface charge of bubbles generated. When bubbles were generated in 1 mM SDS solutions at their natural

pH of around 6.0, the zeta-potential of bubbles was measured to be

around -60 mV. When bubbles were generated in FPW of pH around 8.3, the

zeta-potential turned out to be at a much less negative value of -15 mV. It is

understood that SDS is an anionic surfactant which adsorbs at the bubble-water

interface as a result of its amphiphilic characters[16]. The negatively charged

hydrophilic heads of SDS would contribute to the more negative charge of the

bubbles[32, 145]. FPW, on the other hand is of highly complex water chemistry,

containing not only naturally dissolved surfactants, but also high concentration of

Ca^{2+} and Mg^{2+}. Both cations, as well as $Ca(OH)^+$ and $Mg(OH)^+$, have the

capability of adsorbing at bubble-water interface and lowering the magnitude of

the negative zeta-potential which partially came from anionic surfactants[16, 32, 75, 78, 197]. One other reason for this less negative zeta-potential value of bubble

generated in FPW may be attributed to higher electrolyte concentration which

results in compression of the electrical double layer[31, 74, 79, 92, 197]. The observed

variation of zeta-potential of bubbles in FPW with pH, in some way, was similar

to the case of Ca^{2+}. As FPW is a complex system of high Ca^{2+} concentration, it is

not supersizing to observe reduced effect of pH on zeta-potential. However since

FPW is not only high in Ca^{2+} but also contains natural surfactants, it is

understandable that the zeta-potential of bubbles generated in such system shifted

to a range between -7 mV and -20 mV instead of remaining around zero.

Table 4-1: Effect of temperature and agitation speed on zeta-potential of submicron size bubbles generated in 1 mM SDS + 1 mM KCl solutions and FPW at their corresponding original pHs of approximately 6.0 and 8.3, respectively.

	Agitation Speed (rpm)	Final Temperature (ºC)	Zeta-potential (mV)
1mM SDS + 1mMKCl	2000	50	-61.9 ± 1.9
	2000	70	-62.1 ± 2.9
	3000	70	-64.5 ± 7.1
FPW	500	24	-15.6 ± 2.4
	500	45	-15.9 ± 3.2
	2000	48	-16.5 ± 0.8

Surfactants and frothers have been proven to enhance the stability of gas bubbles by preventing them from coalescence[31, 160]. It is also known that the positive and negative charges of cationic and anionic surfactants would contribute to a rearrangement of ions at gas-water interface[32, 145]. SDS is a common experimentally-studied anionic surfactant where MIBC and DF250 are two most conventional industrial frothers. The zeta-potential of bubbles generated with the assistance of such chemicals is shown in Figure 4-9. By comparison, it was evident that bubbles generated in 1 mM SDS solutions bared a much more negative charge than those in 0.1 mM MIBC or 0.1 mM DF250 solutions due to the anionic character of SDS. Zeta-potential of bubbles generated in 1 mM SDS solutions ranged from -33 mV to -67 mV, while that of bubbles in 0.1 mM MIBC and 0.1 mM DF250 solutions ranged between 2 mV to -51 mV and -8 mV to -51 mV, respectively, with pH changing from 2 to11. Figure 4-9 also shows that bubbles in 0.1 mM MIBC and 0.1 mM DF250 solutions have very similar zeta-potential. This is reasonable as both MIBC and DF250 are considered as non-ionic surfactants and thus should not affect the surface charge of bubbles

significantly, even though they dramatically improve bubble stability. However, one can still see a maximum difference of about 15 mV in the magnitude of zeta-potential when pH changed from 6.5 to 10. Therefore, it is highly possible that, frothers, though with a non-ionic head, compete with OH$^-$ at air-water interface, leading to a change of bubble surface charge. Similar results on effect of surfactants and furthers on zeta-potential of bubbles were reported by several other researchers [32, 85, 145]. It is generally agreed that anionic surfactants bring negative charge to the bubble-water interface while the effect of frother on bubble zeta-potential is relatively smaller.
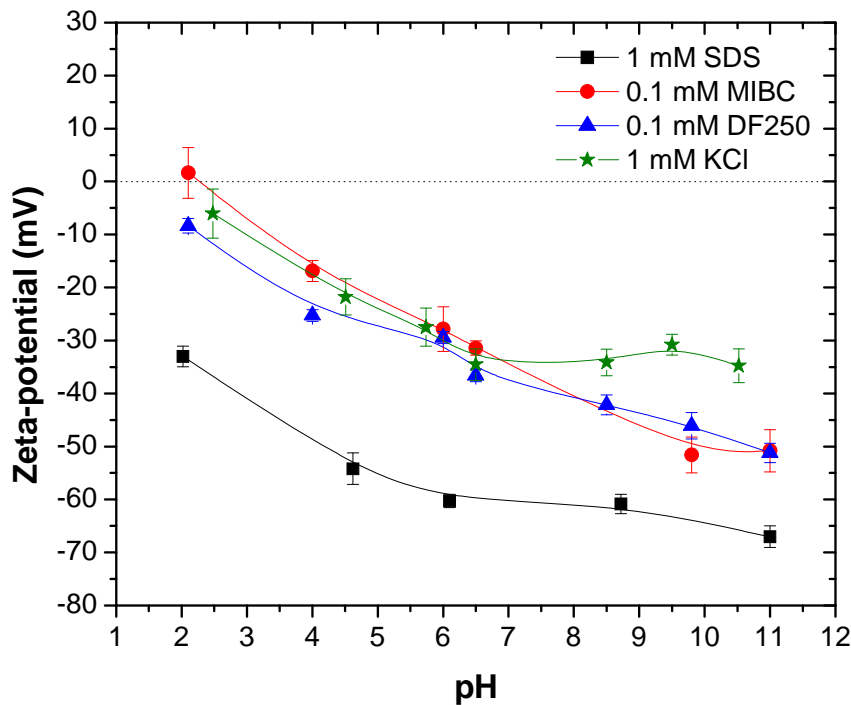
Figure 4-9: Effect of pH on zeta-potential of submicron size bubbles in different surfactant solutions containing 1 mM KCl.

In this study, the effect of gas type on submicron size bubble generation and corresponding physical properties of generated bubbles was also investigated. CO_2 bubbles were generated by pre-saturating the aqueous bubble generation solutions with tanked CO_2 at 8 ºC for 24 hours before HIA. Saturation at lower temperature is intended to dissolve as much gas as possible for bubble generation. Compared with the results in Figure 4-8 for air bubbles, results in Figure 4-10 show that CO_2 bubbles and gas bubbles generated as a result of naturally dissolved air (air bubbles will be used in this paragraph for short) have quite distinct pH dependence of their zeta-potential values to pH changes.
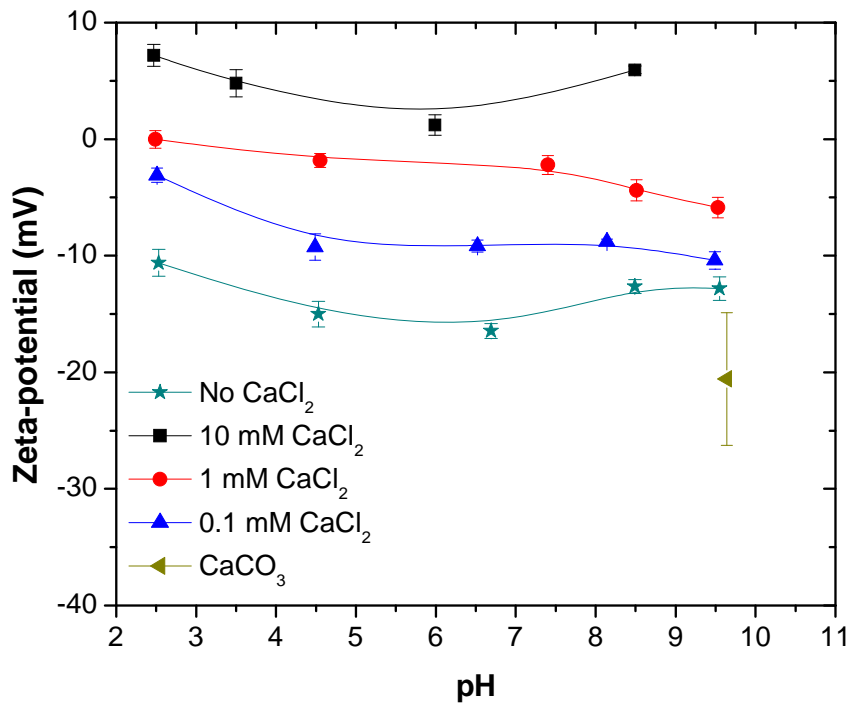
Figure 4-10: Effect of pH on zeta-potential of submicron size CO_2 bubbles in various $CaCl_2$ solutions containing 1 mM KCl (note: zeta-potential of $CaCO_3$ at precipitation pH is measured as reference).

Zeta-potential of CO_2 bubbles at pH 2.5 was -10 mV, which is very similar to zeta-potential of air bubbles at the same pH. However, the zeta-potential value of CO_2 bubbles hardly changed with caustic addition and remained relatively stable varying between -10 mV to -17mV. There appeared to be a minimal value of -17 mV at pH 6.7. However, the difference was only 7 mV in magnitude compared to -10 mV at pH 2.5. It was found during the experiments that the conductivity of CO_2 bubble suspensions at a mild pH of 6.5 was about 0.385 mS/cm, which was almost 3 times the conductivity of air bubble suspensions at the same pH. Increasing conductivity of CO_2 bubble suspension would compress electrical double layer, making the zeta-potential of bubbles less pH-dependent. It is known that CO_2 has a much larger solubility than air which is mostly N_2 and O_2. CO_2 exists in forms of CO_3^{2-}, HCO^{3-} and CO_2 in water with the distribution depending on pH of suspension. These species of CO_2 greatly affect the property of the gas-water interface. Increasing pH (OH^-) would increase concentration of CO_3^{2-} and HCO^{3-} which would make CO_2 bubbles more negative if CO_3^{2-}/ HCO^{3-} would be potential determining ions. The fact that there was no significant change of zeta-potential with pH clearly indicates predominant role of electrical double layer compression. When Ca^{2+} was added to the CO_2 bubble suspensions, the zeta-potential of the CO_2 bubbles were brought to a less negative value and even reversed in 10 mM $CaCl_2$ solutions, indicating specific adsorption of Ca^{2+}. This finding is in contract to air bubbles where bubbles remained negatively charged in 10 mM $CaCl_2$ solutions, indicating the presence of CO_2 species at $CO_2(g)$-water interface, which has stronger affinity to Ca^{2+} than OH^-

does. As anticipated, pH had little effect on zeta-potential values of CO_2 bubbles in presence of three different concentrations of Ca^{2+}, which was also discovered for air bubbles. Compared with zeta-potential of solid $CaCO_3$ precipitation at pH 9.8, the zeta-potential of CO_2 bubbles is much less negative as shown in Figure 4-10, indicating different surface of CO_2 bubbles from $CaCO_3(S)$, i.e. incomplete coverage of CO_2 bubbles by $CaCO_3$.

4.2.2   Stability of Submicron Size Bubbles Generated in Different Solutions

The stability of gas bubbles generated in 1mM KCl was hereby studied. The results in Figure 4-11 show that bubbles generated in 1 mM KCl solutions (pH 6) agitated at 2000 rpm for 30 min had an average bubble diameter of 352 nm, and maintained to be visible even 5 hr after generation. This finding suggests that submicron size bubbles generated by HIA had a life span of 5 hours in 1mM KCl solutions. During the measurement period after bubble generation, the bubble size was found fluctuating around an average value of 370 nm. However, 6 hr after agitation, bubbles were hardly detected by ZetaPALS. Since bubbles at these sizes are of negligible buoyancy to float away, the extinction of bubbles in suspension provides an indirect evidence of bubble dissolutions in the absence of protective surfactant layer. Without protective surfactant layer, submicron size bubbles may coalesce to become substantially larger size bubbles and disappear by flotation to the top of suspension, contributing to the disappearance of bubbles with time. However, since no significant increase in bubble size was measured, this mechanism is unlikely significant for bubble disappearance.
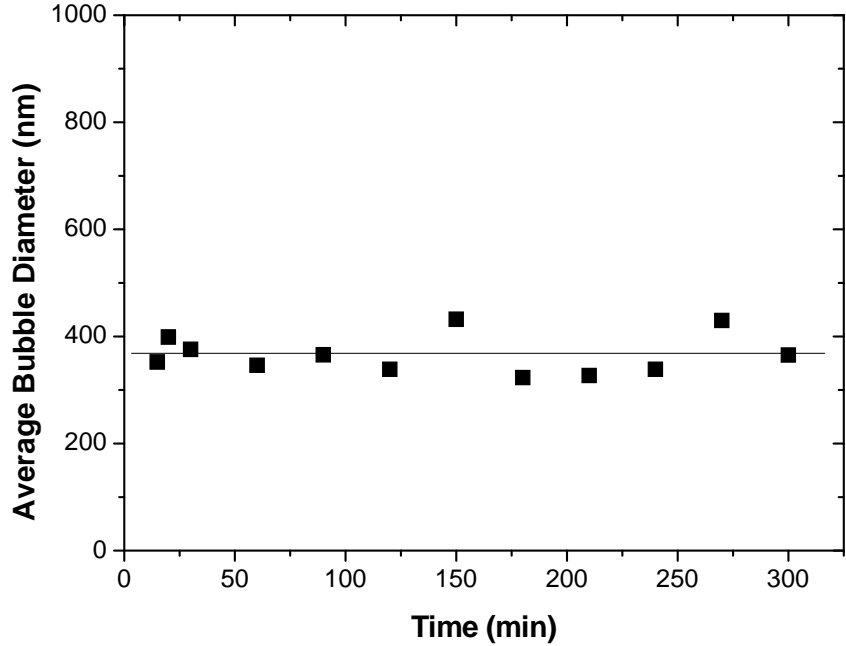
Figure 4-11: Stability of submicron size bubbles generated in 1 mM KCl solution of pH 6.0 by HIA at 2000 rpm for 30 min.

Similar tests were preformed on bubbles generated in 1 mM SDS + 1 mM KCl solutions under the same condition, with the monitoring period after bubble generation extended to 24 hr. The results in Figure 4-12 show that, submicron size bubbles generated in 1 mM SDS solutions at pH 6.0 had an average bubble diameter of 460 nm. Over the monitored period of 24 hours, the size of bubbles was seen to be remarkably constant at about 500 nm. Although a slight increase in bubble size was observed with prolonged measurement time, the increase can be considered negligible when the experimental error is taken into consideration. The population (average count rate) and zeta-potential of the generated bubbles were also recorded within this 24 hr period. The count rates varied between 11 kcps and 13 kcps, showing insignificant change in the number

of submicron size bubbles generated; the zeta-potential of bubbles was also found to remain around -60 mV without significant fluctuation over the period of measurement, as anticipated. It is again confirmed here that adsorption of SDS at the gas-water interface of submicron size bubbles seemed not only to impart the negative charge to the bubble surfaces, but also provide a protective layer to prevent bubbles from coalescing and dissolution[85] , which is distinct from air bubbles generated in 1 mM KCl solutions.
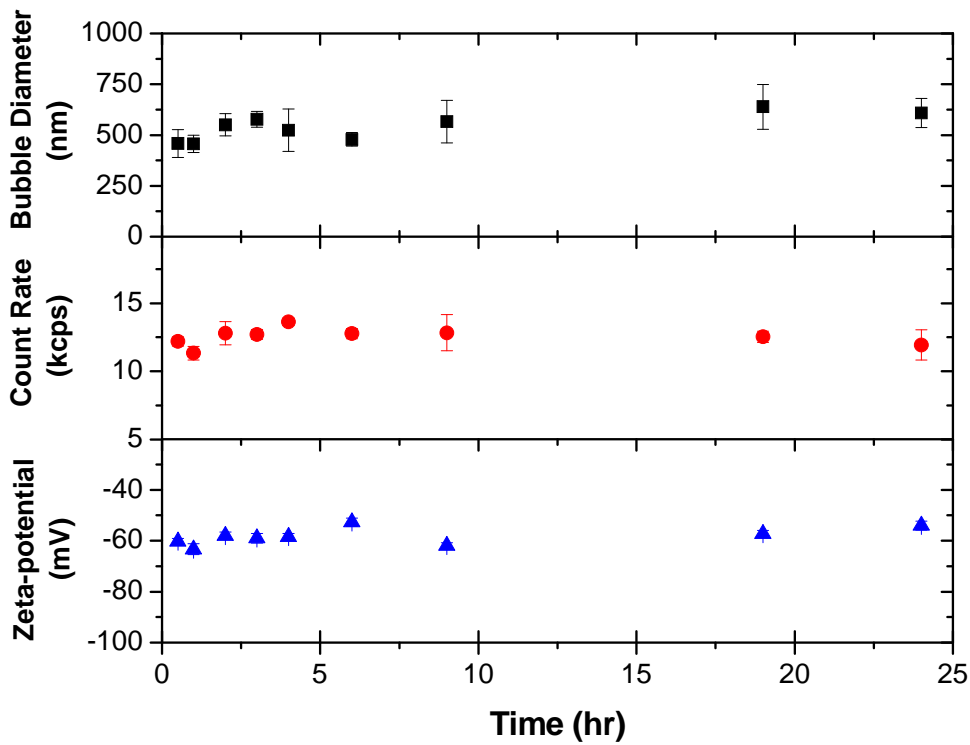
Figure 4-12: Stability of submicron size bubbles generated in 1 mM SDS + 1 mM KCl solutions of pH 6.0 by HIA at 2000 rpm for 30 min.
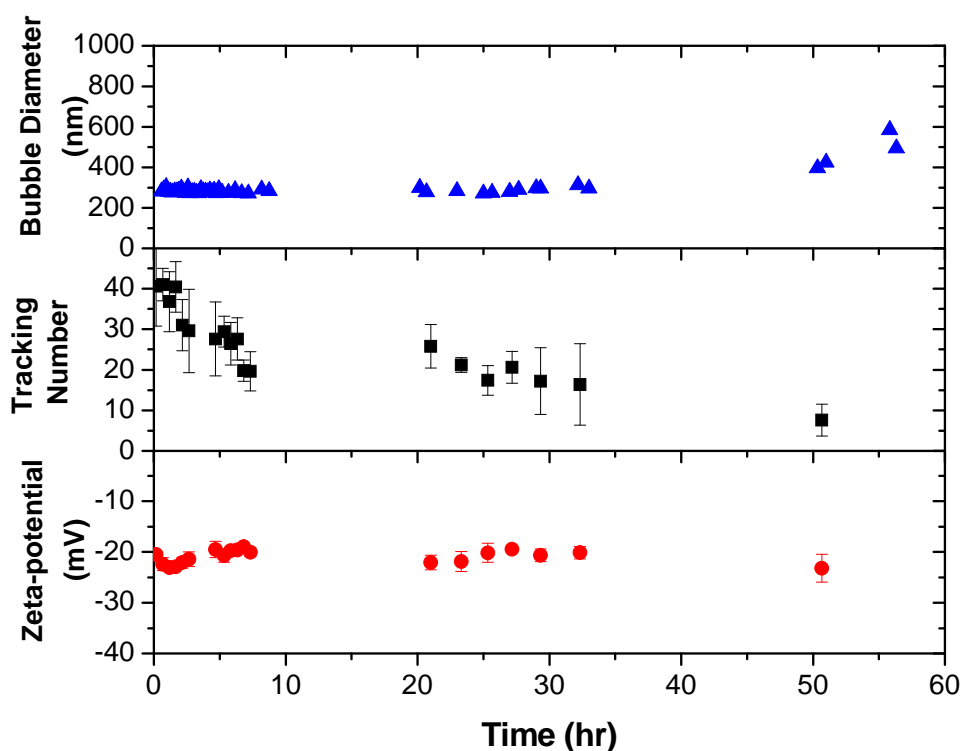
Figure 4-13: Stability of submicron size bubbles generated in FPW of pH 8.3 by HIA at 2000 rpm for 30 min, measured with Zetaphoremeter.

Finally, the stability of submicron size bubbles generated in FPW under the same conditions was examined. In order to validate that the former stability results were not due to artefact of ZetaPALS, the stability of the number and zeta-potential of bubbles generated in FPW was examined using Zetaphoremeter for confirmation while the size of the bubbles was still measured using ZetaPALS. Shown in Figure 4-13, within the first 24 hr after agitation, the bubbles remained considerably stable with a diameter around 300 nm and zeta-potential about -20 mV. However, starting from 50 hours after generation, the diameter of the bubbles started to increase from 300 nm to almost 600 nm, suggesting growth in bubble size, which would likely lead to eventual disappearance of bubbles from

suspension by flotation. And as for zeta-potential values, they continued to be constant at approximately -20 mV. Since the average count rate was a special feature given by ZetaPALS to reflect the population of bubbles, it was impossible to quantify the number of bubbles by count rate. Zetaphoremeter however, also had a unique function to provided the "tracking number" as a measure of bubble population as mentioned in Section 3.3.4. For this reason, the amount of bubbles during the measurement was tracked. Figure 4-13 shows that during the whole measurement period of 50 hr, there was significant drop in tacking number from 40 to 8, suggesting disappearance of bubbles during this period. The result seemed reasonable as bubbles may either shrink and dissolve into the solutions, or/and grow to a larger size and disappear by slowly rising to the surface of the solution. This observation is in good agreement with results demonstrated in bubble size measurement. Such trend was however not observed for bubbles generated in the first two sets of measurements using ZetaPALS. This discrepancy is attributed to Zetaphoremeter being more sensitive in tracking bubbles of larger sizes which would disappear with time.

Generally speaking, the results displayed in the stability study of the generated submicron size bubbles suggest that such bubbles generated by HIA in 1 mM KCl, 1 mM SDS + 1 mM KCl solutions and FPW are suitable for investigation of fine particle-bubble interactions (attachments) by zeta-potential distribution analysis.

4.3   Summary

1) HIA is capable in generating submicron size bubbles with diameters less than
    1 μm through hydrodynamic cavitation. Submicron size bubble generation by
    HIA is largely affected by factors such as agitation speed, agitation time and
    temperature of solutions. With increasing agitation speed, the size of bubbles
    generated in 1 mM KCl and 1 mM SDS solutions decreases while the number
    of the bubbles increases. For the case of FPW, bubbles remain at a constant
    diameter but increase in number as the agitation speed increases. Temperature
    has a larger effect on bubble generation only when it exceeds 50 °C while the
    effect is negligible at lower temperatures. Agitation time has small effect on
    bubble generation when agitation speed is high. However, the effect of
    temperature and agitation time on bubble generation needs to be further
    confirmed.

2) Bubbles generated by HIA in 1 mM SDS solutions and FPW remain stable for
    as long as 24 ~ 50 hours, whereas those generated in 1 mM KCl solutions
    disappear in 5 hours after generation. With extending the measurement time,
    slight increase in bubble size could be observed while the zeta-potential of
    bubbles remains constant throughout the measurement period. A decrease in
    number of bubbles in solutions was detected only by Zetaphoremeter not by
    ZetaPALS. This finding indicates that quantification of the number of bubbles
    generated is strongly dependent on the sensitivity of the instrument used in
    tracking the entire bubble population, as different instrument could provide
    very different results.

3) The zeta-potential of submicron size bubbles is strongly pH dependent in the case of 1 mM KCl solutions and surfactant/frother solutions. Zeta-potential of bubbles in such solutions becomes increasingly negative with increasing pH. Bubbles generated in FPW is less affected by pH as their zeta-potential becomes relatively constant at around -20 mV when the pH of the FPW becomes higher than pH 6.

4) Ca^{2+} ion strongly affects the zeta-potential of bubbles generated. The positive charge of Ca^{2+} ion makes the zeta-potential of bubbles less negative (between 0 mV ~ -10 mV) and less dependent on pH. However, further addition of Ca^{2+} ion from 0.1 mM to 10 mM does not continue to make the zeta-potential of bubbles less negative. SDS is capable of lowering the zeta-potential of bubbles generated. The effect of frothers on zeta-potential becomes is more significant at higher pH.

5) Surface charge of CO_2 bubbles is very different from that of air bubbles. CO_2 bubbles bare a much smaller negative charge which does not change with pH. The influence of Ca^{2+} ion on zeta-potential of CO_2 bubbles is more apparent than that of air bubbles. The presence of Ca^{2+} ion lowers the magnitude of the negative surface charge values of CO_2 bubbles. Increasing concentrations of Ca^{2+} ion further reduce the negative charge of CO_2 bubbles, which even become reversed to positive at 10 mM of Ca^{2+} ion concentrations.

Chapter 5 Interactions of Submicron Size Bubbles with Colloidal Solids

5.1   Inorganic Electrolyte Solutions

In this section, zeta-potential of alumina micron and nano particles and silica micron and nano particles were measured. Results were compared with zeta-potential results of submicron size bubbles. Based on the stability of bubbles generated, and the difference in zeta-potential of bubbles and particles, bubble-alumina (micron) and bubble-silica (micron) interactions in 1 mM KCl solutions were studied.

5.1.1   Zeta-Potential of Single Components

It was discussed in Section 3.2.1 that one of the most important conditions for studying interactions by zeta-potential distribution measurement is to have adequate differences between zeta-potential distribution peaks of the single components in an interaction system (mixture). pH had been shown by researchers[31, 32, 75, 78, 145, 198] to play an important role in determining the zeta-potential of materials. Therefore, pH could be used to adjust the difference between zeta-potential distribution peaks of two interacting components by shifting the position of the zeta-potential distribution peaks. To find optimize pH conditions for studying bubble-particle interactions using zeta-potential distribution measurement, the zeta-potential of single component alumina and silica particles (micron and nano) was measured. Figure 5-1 shows the results of

zeta-potential measured for alumina and silica particles (micron and nano) in 1 mM KCl solutions with or without 1m M CaCl$_2$ as a function of pH. For comparison, the results of submicron size bubbles were also included in this figure.
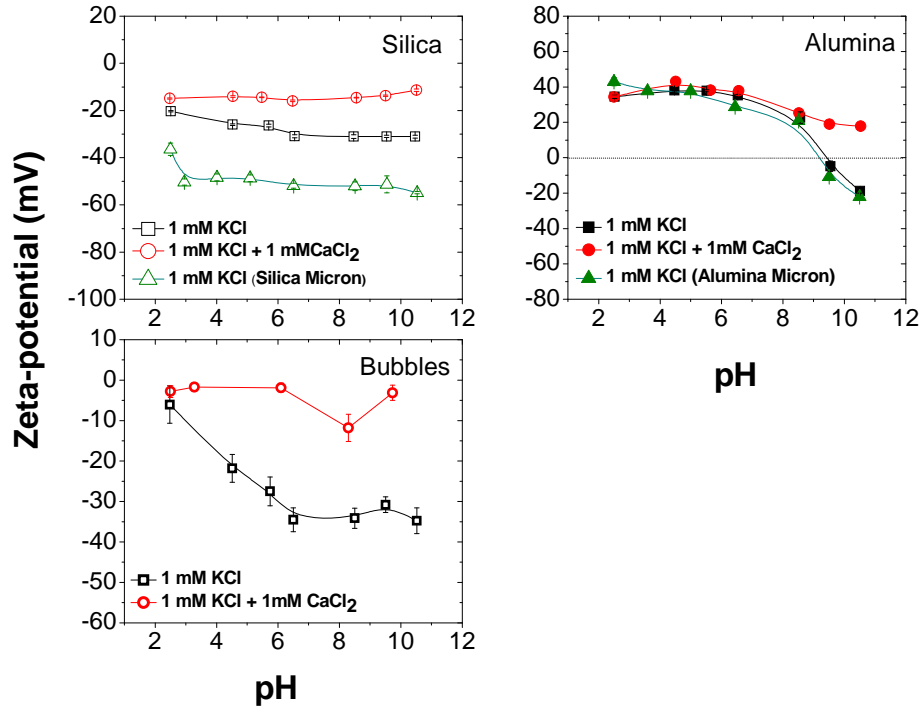
Figure 5-1: Zeta-potential of submicron size bubbles and silica and alumina particles in 1mM KCl and 1mM KCl + 1mM CaCl$_2$ solutions. Particles are in nano sizes unless otherwise specified.

Figure 5-1 shows that in1 mM KCl solutions, silica particles were negatively charged between -36 mV ~ -55 mV in the selected pH range of 2 ~ 11. Zeta-potential of alumina particles ranged between 0 mV ~ 43 mV below pH 9.0. Above pH 9.0, the zeta-potential of alumina particles reversed to a negative value and a minimum value of -22 mV was found at pH 10.5. This result agrees with

reported isoelectric points of alumina[187, 188]. For both particles, zeta-potential was found to decrease (becoming more negative or less positive) with increasing pH. The effect of pH on zeta-potential of micron size particles was more significant between pH 2 ~ 3 for silica particles and when above pH 6 for alumina particles.

Considering particle size might affect bubble-particle interactions[70, 200, 201], silica and alumina nano particles (simply referred to silica and alumina or silica and alumina particles in this work unless otherwise stated) were purchased to match the size of submicron size bubbles. The zeta-potential of the nano particles was measured and shown in Figure 5-1. Zeta-potential of silica nano particles in 1mM KCl solution remained negative between pH 2.5 ~ pH 10.5. Zeta-potential values of nano silica particles were relatively smaller as compared with the value for micron size silica particles in the same solution. Although the isoelectric point of silica was reported to be around pH 2[80, 83], the isoelectric point of silica was not detected in the current experiment. Figure 5-1 also showed that when the pH of the 1mM KCl solution increased from pH 2.5 to pH 10.5, the zeta-potential of alumina particles changed from a maximum positive value of 38 mV at pH 4.5 to a maximum negative value of -19mV at pH 10.5. A significant drop in zeta-potential of alumina particles was also observed at around pH 6 and the isoelectric point was again found to be around pH 9, which is identical to the value for micron size alumina particles.

Zeta-potential of the silica and alumina nano particles were further measured in 1 mM KCl + 1 mM $CaCl_2$ solution. The results are also shown Figure 5-1. With the addition of 1mM $CaCl_2$, zeta-potential of silica increased by

6 mV ~ 20 mV within the range from pH 2.5 to pH 10.5. Similar to the results of submicron size bubbles, the dependency of zeta-potential of silica nano particles on pH was weak. The zeta-potential value remained approximately -15 mV throughout the pH range investigated. The results of alumina nano particles with Ca^{2+} addition showed obvious difference in the effect of cations. The added Ca^{2+} did not seem to further increase the zeta-potential of alumina particles until pH approached 9, where the surface charge of alumina became negative. This result is not supersizing as alumina particles bear positive charge below its pzc. Ca^{2+} would not adsorb at positively charged alumina surfaces. However, it compresses the electrical double layer. When the surface charge of alumina became negative (around pH 9), Ca^{2+} would start to adsorb on the negatively charged particle surfaces, thus making the surfaces less negative or even positive again. When the effect of Ca^{2+} was dominant in affecting alumina zeta-potential, the zeta-potential values were less independent on pH. This observation is similar to what was found in cases of silica nano particles and submicron size bubbles.

Zeta-potential of submicron size bubbles in solutions of same chemistry are provided in Figure 5-1 for comparison. As discussed in Section 4.2.1, bubbles were negatively charged in 1 mM KCl. The zeta-potential approached zero when $CaCl_2$ was added. Zeta-potential of bubbles in KCl solutions became more negative with increasing pH, but changed only marginally as a function of pH in 1 mM KCl + 1 mM $CaCl_2$ solutions. By comparing the three graphs in Figure 5-1, it is obvious that KCl solutions was better for studying bubble-particle interactions by zeta-potential distribution measurement as the difference in

zeta-potential of bubbles and particles were much larger than the case with Ca^{2+} addition. The optimum pH for studying bubble-particle interactions using the zeta-potential distribution analysis was shown to be around pH 6 where the zeta-potential difference between bubbles and silica micron particles, and between bubbles and alumina micron particles was 15 mV and 40 mV, respectively.

5.1.2   Interactions of Silica and Alumina with Submicron Size Bubbles

Zeta-potential distribution measurements of silica or alumina micron size particles and submicron size bubbles were preformed in 1 mM KCl solutions at their natural pHs. The pH of the bubble-alumina micron size particle interaction system was measured to be 5.3 whereas pH 6.0 was obtained from bubble-silica micron size particle interaction system. Results from these systems would serve as basis for designing the more complicated bubble-particle interaction systems.

Zeta-potential distribution of the micron size particles and bubbles were first measured individually in 1mM KCl solutions and then in the forms of bubble-particle mixtures at a 1:1 volume ratio. The corresponding zeta-potential distributions are shown in Figure 5-2.

The zeta-potential distributions of alumina micron size particles and submicron size bubbles had peaks at 39 mV and -30 mV, respectively. A unimodal zeta-potential distribution was observed for bubble-alumina micron size particle mixtures. The location of the distribution peak was at -12 mV, which is located in-between the distribution peaks of bubbles and particles measured separately. This result indicates attachment of alumina particles to submicron size bubbles, which was not unexpected as the two components were of opposite

103

charge and therefore a strong electrostatic attraction force was anticipated between bubbles and micron size alumina particles. Based on the fundamentals of the zeta-potential distribution analysis technique described in Section 3.2.1.4, it is most likely that the surfaces of the positively charged micron size alumina particles were partially covered by the negatively charged bubbles. Because the diameter of micron size alumina particles was more than twice the diameter of bubbles, the possibility of bubbles attaching to particle surfaces was relatively higher. Moreover, an equal number of bubbles and particles in the mixture would lead to a total alumina surface area at least four times the total bubble surface area. Such difference suggests that there would be insufficient number of bubbles to fully cover the total surface of micron size alumina particles. All in all, it is firm to conclude that strong attachment occurred between positively charged micron size alumina particles and negatively charged bubbles in 1 mM KCl solution.

Graph on the right hand side of Figure 5-2 describes interactions of bubble with micron size silica particles in 1 mM KCl solutions. When measured separately, the zeta-potential distribution peak of micron size silica particles was located at -54 mV. The zeta-potential distribution of micron size silica particles was sharp suggesting small variation in surface charge among individual particles. The bubbles had a broad zeta-potential distribution from -20 mV to -62 mV with a peak at -54 mV. This widely-spread distribution of bubbles indicates polydispersity of surface charge of bubbles. The zeta-potential of the bubble-silica micron particle mixture was measured to range from -21 mV to -57 mV, covering the range of the zeta-potential distributions of both micron size silica particles and

bubbles, with a peak position of -47 mV. In this case, no clear gap between the individual peaks of the two components was observed. Thus, the zeta-potential distribution analysis technique was less applicable as the attachment of bubbles and silica micron particles was difficult to determine. However, as surface of the micron size silica particles were hydrophilic and both surfaces were negatively charged, due to electrostatic repulsion, bubbles are unlikely to attach to micron size silica particles. To confirm this conclusion requires further experiments using the technique.
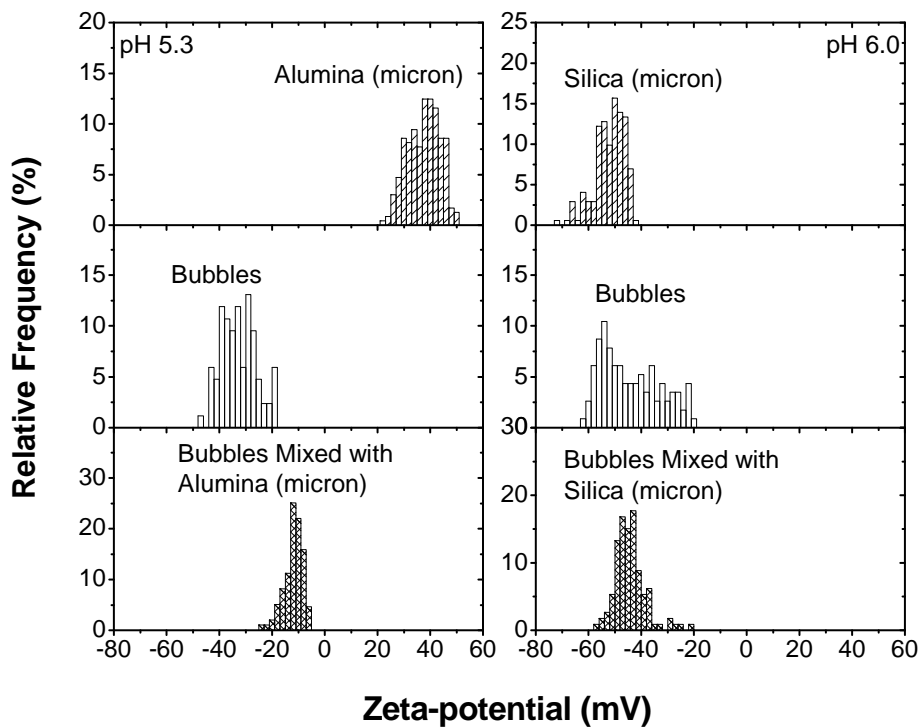
Figure 5-2: Zeta-potential distributions of submicron size bubbles and micron size alumina and silica particles in 1 mM KCl solutions at their natural pHs, measured individually or in a binary mixture.

5.1.3   Summary

1) Silica (both micron and nano particles) was negatively charged in 1 mM KCl
   and 1 mM KCl + 1 mM $CaCl_2$ solutions of pH from 2.5 to 10.5.
   Zeta-potential of micron and nano size silica particles showed a moderate
   decrease with increasing in pH in 1 mM KCl solutions, while zeta-potential of
   silica nano particles in 1 mM KCl + 1 mM $CaCl_2$ solution was less pH
   dependent.

2) Alumina (both micron and nano particles) was positively charged in 1mM
   KCl and 1 mM KCl + 1 mM $CaCl_2$ solutions at most pHs. Zeta-potential of
   micron and nano size alumina particles progressively decreased with
   increasing pH above pH 6.5 in 1 mM KCl solutions. Isoelectric point of
   alumina particles was found to be around pH 9.0. Nano size alumina particles
   remained positive even after pH 9.0 with 1 mM $CaCl_2$ addition. In the
   presence of 1 mM $CaCl_2$, the zeta-potential values of alumina nano particles
   were less dependent of pH.

3) Negatively charged submicron size bubbles strongly attached to positively
   charged micron size alumina particles as a result of electrostatic attractive
   force. However, zeta-potential distribution analysis technique was unable to
   determine interaction of bubble- micron size silica particles due to the overlap
   of zeta-potential distributions of bubbles and particles.

5.2   Surfactant and Frother Solutions

As mentioned, frothers and surfactants are surface active agents used in
froth flotation. The addition of frothers or surfactants reduces the surface tension

of the aqueous solution and changes the properties of bubbles[85, 145, 152, 154, 156]. In order to generate more submicron size bubbles of higher stability and modify the surface properties of the bubbles generated, frothers and surfactants were used in this work. By using frothers and surfactants, the applicability of zeta-potential distribution analysis technique for studying bubble-solid interactions was expected to be improved. Interactions of silica and alumina nano particles with submicron size bubbles in SDS (anionic surfactant), DAH (cationic surfactant), MIBC and DF 250 (frothers) solutions were studied. The concentration of surfactants and frothers was chosen to meet the priority of generating sufficient number of stable submicron size bubbles.

5.2.1   SDS Solutions

5.2.1.1 Interactions of Silica and Alumina with Submicron Size Bubbles

Zeta-potential distributions of bubble-alumina and bubble-silica interactions in 0.01 mM SDS + 1 mM KCl solution at pH 6.0 are shown in Figure 5-3. The zeta-potential distribution of alumina particles spread from 25 mV to 57 mV with a peak located at 36 mV. The zeta-potential distribution peak of submicron size bubbles in 0.01 mM SDS + 1 mM KCl solution is located at -53 mV. The zeta-potential distribution of submicron size bubbles is rather narrow compared to what that in 1 mM KCl solutions. By comparison with the zeta-potential results of -32 mV and bubbles in 1mM KCl solution of same pH, it is clear that SDS adsorbed at bubble-water interface. SDS adsorption not only made the bubble surface more negatively charged but also less hydrophobic due to ionic groups of the surfactant at bubble-water interface. However, the effect of

107

SDS on zeta-potential of alumina was negligible, suggesting low SDS adsorption at alumina surface. Such finding agrees with the zeta-potential and adsorption results from former studies[202-204]. Researchers found that although changes in alumina zeta-potential was closely related to SDS adsorption on solid surface, at surfactant concentration as low as the case here, only trace amount of SDS adsorbed on alumina surface while the zeta-potential of alumina remained almost the same as the case without surfactant addition[202-204]. On the other hand, previous force measurement results show that even at such low concentration, SDS adsorption on alumina surface resulted in obvious decrease in electrostatic repulsive force among the alumina particles. The observed adsorption was attributed to hydrophobic attraction induced by the hydrophobic chain of SDS[205].

When alumina and bubbles suspensions were mixed at a 1:1 volume ratio, the mixture had a unimodal distribution with zeta-potential ranging from -1 mV to -25 mV and peaked at -10 mV. Such single-peak zeta-potential distribution of the mixture suggests that strong attachment occurred between the two components. Since both components are of similar population in the mixture, it is unlikely one component would fully cover the other, leading to the observed zeta-potential distribution characteristics, i.e. the zeta-potential distribution measured in the mixture was more likely the result of bubble-particle aggregates. As a result of SDS adsorption, bubble-alumina attachment here is most likely due to electrostatic attractive force between positively charged alumina and negatively charged air bubbles.
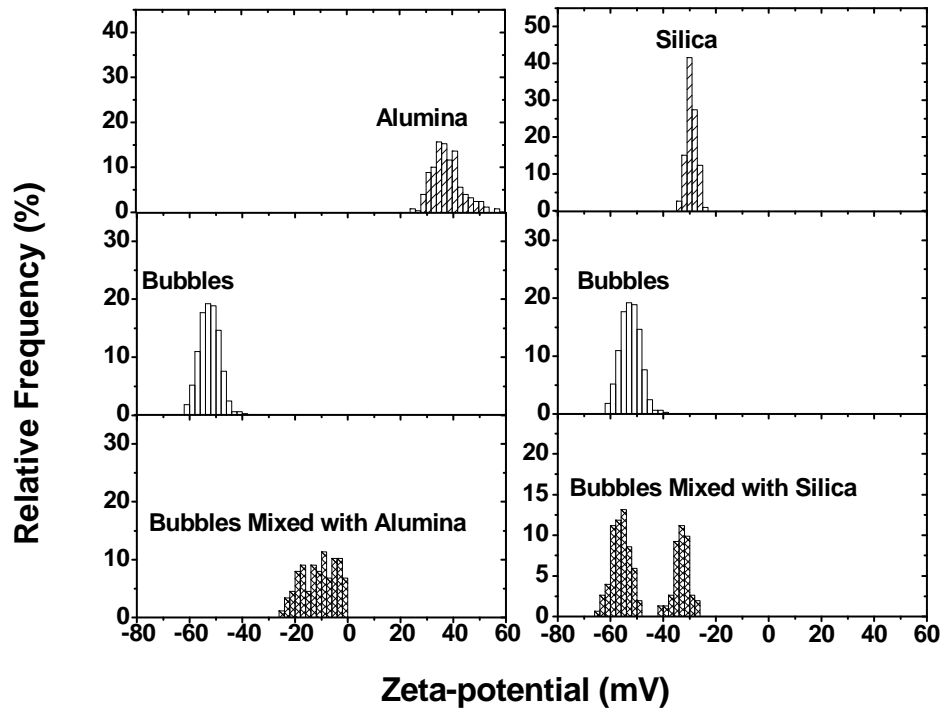
Figure 5-3: Zeta-potential distributions of submicron size bubbles with nano size alumina and silica particles in 0.01mM SDS + 1 mM KCl solutions at pH 6.0, measured individually or in a binary mixture.

Figure 5-3 also shows a zeta-potential distribution peak at -30 mV with a rather narrow distribution for silica in 0.01 mM SDS + 1 mM KCl solution at pH 6.0. This distribution is similar to that of silica in 1mM KCl (Figure 5-1), indicating little, if any adsorption of SDS on silica. As silica surface is negatively charged, the absence of adsorption of anionic SDS is anticipated. When silica and bubbles were mixed together, the binary mixture showed a zeta-potential distribution of two distinct peaks. These two peaks were located at -55 mV and -33 mV, which correspond to those of bubbles and silica when measured individually. This finding implies that no obvious attachment/aggregation

occurred between bubbles and silica particles. The electrostatic repulsion between negatively charged silica and bubbles is responsible for the absence of attachment.

Micron size silica particles were treated to become hydrophobic by soaking the particles in 0.5% (volume percentage) of chlorotrimethylsilane (C_3H_9ClSi, 97%, Aldrich) in toluene solution ($C_6H_5CH_3$, ACS, Fisherchemicals), overnight, followed by washing with pure toluene for 5 times before being air-dried. The interaction of these hydrophobic micron size silica particles with submicron size bubbles were studied in 0.01 mM SDS + 1 mM KCl at pH 6.0. Results of bubble-hydrophobic silica interactions are shown in Figure 5-4 in comparison with previous results of bubble-silica (nano particles) interactions under the same condition.

Large variation among surface charges of hydrophobic silica micron particles was shown by a widely spread zeta-potential distribution of the hydrophobic particles, ranging from -35 mV to -57 mV. The distribution peak of hydrophobic silica was observed at -41 mV. The bubbles distribution spread between -39 mV and -61 mV with a peak at -53 mV. When the hydrophobic micron size silica particles and submicron size bubbles were mixed together, a bimodal distribution was observed. This broadly spread distribution started from -35 mV and ended at -61 mV, where one of the peaks was located at -51 mV and the other at -41 mV. This bimodal distribution was almost the exact combination of the individual distributions of the hydrophobic micron size silica particles and bubbles when measure separately. Such distribution suggests the absence of attachment in the mixture. This result may be caused by the

110

overwhelming electrostatic repulsive between highly negatively charged bubbles and particles. Even thought the silica particles are hydrophobic initially, the role of hydrophobic force could not be clearly determined here as the adsorption of SDS on hydrophobic silica and air bubbles would make both hydrophilic, eliminating hydrophobic force. To evaluate hydrophobic contributions, further experiments need to be designed to measure the hydrophobicity of both bubbles and silica particles.
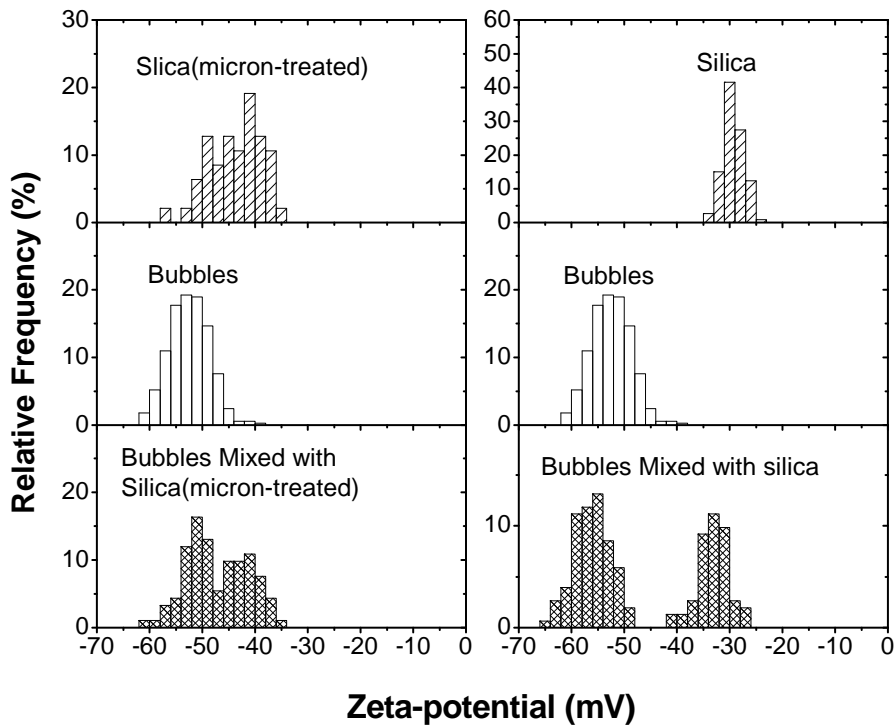
Figure 5-4: Zeta-potential distributions of submicron size bubbles, hydrophobic micron size silica particles and nano size silica particles in 0.01m M SDS + 1 mM KCl solutions at pH 6.0, measured individually or in a binary mixture.

5.2.1.2 Effect of pH

Interaction of alumina with air bubbles in 0.01 mM SDS + 1 mM KCl solutions was studied as a function of pH. To study the effect of *in situ* gas nucleation on bubble-particle interaction, *in situ* gas nucleation procedure was introduced in this part of the experiments in comparison with the mixing process. Therefore, four types of zeta-potential distribution measurements were conducted in total, namely, measurements of alumina particles, bubbles, *in situ* nucleation and mixing process. Alkaline conditions were used in this set of experiments to control the surface charge of alumina particles.

It had already been shown in the preceding experiments that strong attachment of alumina and bubbles occurred when mixed in 1 mM SDS solutions at pH 6.0. The bubbles-alumina aggregates had a zeta-potential distribution somewhere in-between those of individual bubbles and alumina. As shown in Figure 5-5, the zeta-potential distribution peaks of bubbles and alumina were measured at -45 mV and 37 mV, correspondently, under current conditions. The number of the interacting bubbles and alumina particles in both processes of mixing and *in situ* gas nucleation were controlled to be at a 1:1 ratio by the method described in Section 3.3.4.1 and Section 3.3.4.2, respectively. Figure 5-5 shows that the zeta-potential distributions of *in situ* gas nucleation and mixing were similar both in the shape and location. Such unimodal distributions indicate that both processes had the same outcome of forming bubble-alumina aggregates, as anticipated between negatively charged bubbles and positively charged alumina particles.

112
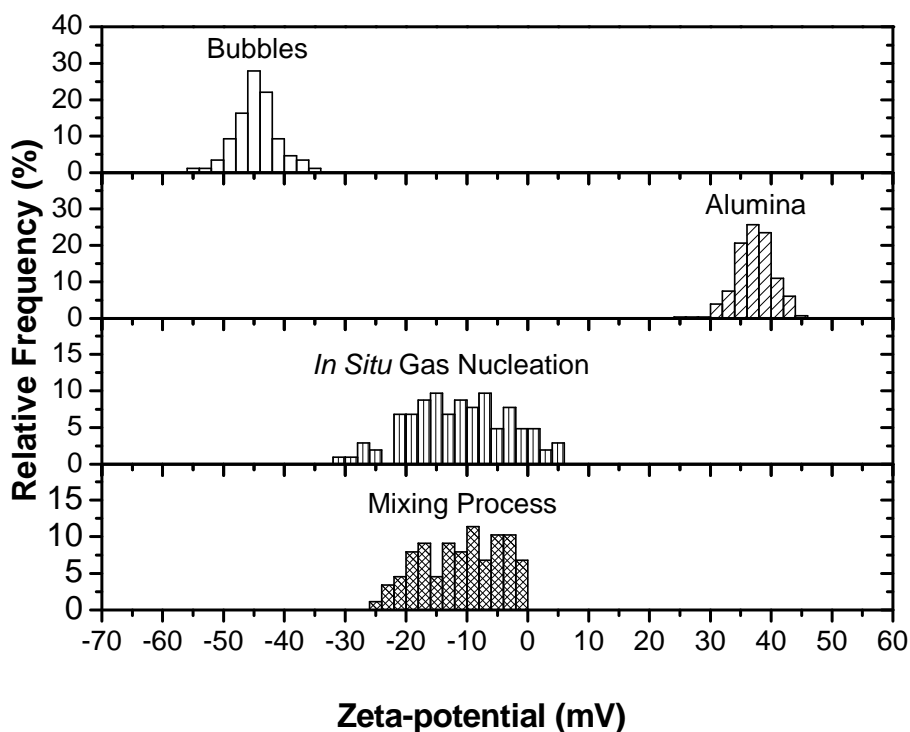
Figure 5-5: Zeta-potential distributions of submicron size bubbles and nano size alumina particles in 0.01 mM SDS + 1 mM KCl solutions at pH 6.0, measured individually or in a binary mixture.

When the pH of the SDS solution was adjusted to pH 9.8, as shown in Figure 5-6, zeta-potential of alumina was reversed to a slightly negative value and the zeta-potential of bubbles further decreased to become more negative. The zeta-potential distribution peaks of the bubbles and alumina particles were located at -51 mV and -10 mV, respectively. Compared with the results of bubbles and alumina in 1 mM KCl (Figure 5-1) where corresponding zeta-potential distribution peak values were around -34 mV and -9 mV, adsorption of SDS at bubble-water interface was apparent while the amount of SDS adsorbed at alumina surface was negligible.

113

For the mixing process, two distinct distribution peaks were observed as shown in Figure 5-6. The peaks of the two distributions were located at -51 mV and -17 mV. Such peaks matched well with those of bubble and alumina when measured separately, indicating that bubbles and alumina particles in the mixture did not attach to each other. Such finding is reasonable as electrostatic repulsive force is expected among the negatively charged bubbles and particles. A small shift of the distribution peak of alumina was mostly likely due to electrokinetic retardation.

The situation was however very different in the case of *in situ* gas nucleation. It is shown in Figure 5-6 that the zeta-potential distribution of alumina suspension after *in situ* gas nucleation was relatively broad but clearly single-peaked. The peak of the distribution was located at -31 mV with the left side of the distribution dragging towards -67 mV. It was suggested by such distribution that bubbles were attached to alumina particles during *in situ* gas nucleation. This significant difference seen between zeta-potential distribution results of *in situ* gas nucleation and mixing process suggest that these two processes have very different effect on bubble-particle interactions. It is believed that during *in situ* gas nucleation, tiny bubbles are nucleated on the surface of solid particles in the form of gas hemi-spheres or gas envelopes instead of free bubbles in the bulk of the solution[51, 58, 60, 60, 70]; whereas during the mixing process, bubbles are expected to be attracted to the solid particles by colloidal forces to finally accomplish attachment. It was reported by many researchers that *in situ* gas nucleation promotes bubble-particle interactions[58, 59, 70]. These former findings are in an

excellent agreement with zeta-potential distribution results shown here in Figure 5-6, which shows that under the same conditions of weak electrostatic repulsion, bubble will only attach to alumina to form aggregates by *in situ* gas nucleation but not by mixing.
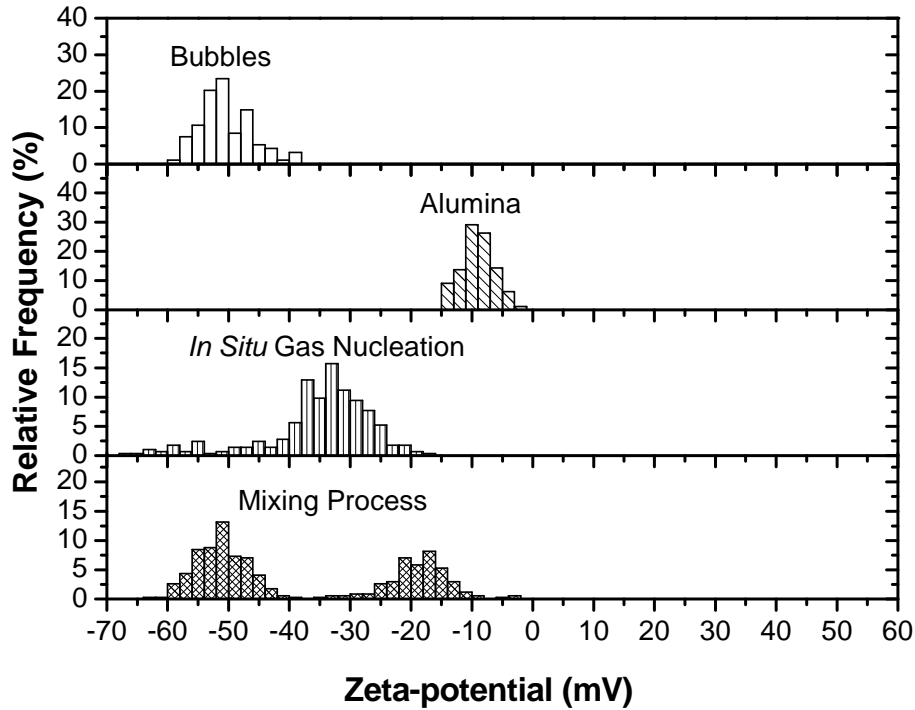

Figure 5-6: Zeta-potential distributions of submicron size bubbles and nano size alumina particles in 0.01 mM SDS + 1 mM KCl solutions at pH 9.8, measured individually or in a binary mixture.

The pH of the 0.01 mM SDS + 1 mM KCl solution was further increased to pH 11.0 where zeta-potentials of both bubbles and alumina particles were of highly negative values. The results of zeta-potential distribution measurement at pH 11.0 are shown in Figure 5-7. Zeta-potential distributions of submicron size bubbles and alumina particles peaked at -54 mV and -25 mV, both more negative

than the values at pH 9.8. When compared with zeta-potential distributions in

1 mM KCl solution (Figure 5-1), similar conclusion was drawn that: SDS

adsorbed on bubbles but hardly on alumina particles, as observed at the other two

pH conditions.

As presented in Figure 5-7, *in situ* gas nucleation in this case showed two

distinct distribution peaks at -56 mV and -20 mV, which are similar to those

measured independently for bubbles and particles. The zeta-potential distributions

of mixing process were almost identical to those of *in situ* gas nucleation,

showing two sharp peaks at -52 mV and -16 mV. These results point out that no

attachment of bubbles and alumina particles occurred. Under this condition, the

highly negative surface charge of the two components induces a strong

electrostatic repulsive force between bubbles and particles, preventing them

approaching each other. Even under *in situ* gas nucleation condition, bubbles were

no longer nucleated on highly negative, hydrophilic alumina surfaces, but

generated in the bulk solutions[51]. Consequently, individual bubbles generated

during *in situ* gas nucleation and alumina particles were pushed away from each

other as a result of strong electrostatic repulsion, same as observed during mixing

process.

By comparing the zeta-potential distributions of mixing process in

Figure 5-6 and Figure 5-7, it is interesting to note that the mutual effect caused by

the hydrodynamic interaction of the neighbouring bubbles and alumina particles

seemed to have different impact on zeta-potential distributions of the two

components in a mixture of varying strength in electrostatic double layer

116

repulsive force. When the electrostatic repulsive force was weak, the mutual effect of the two different components shifted the two respective zeta-potential distributions toward each other, whereas when the electrostatic repulsive force was strong, the zeta-potential distributions parted from each other.
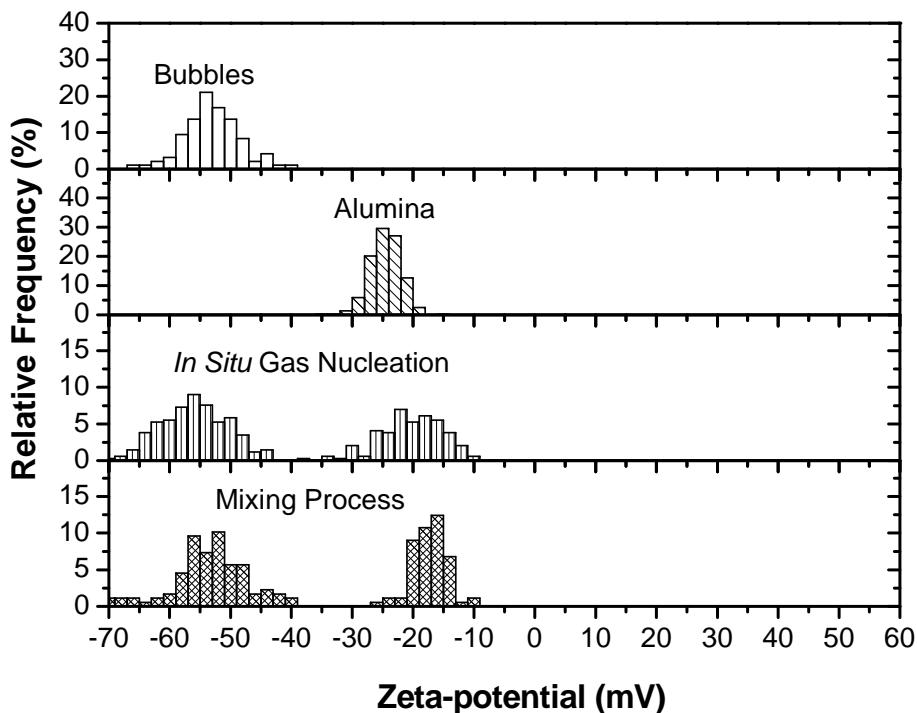

Figure 5-7: Zeta-potential distributions of submicron size bubbles and nano size alumina particles in 0.01 mM SDS + 1 mM KCl solutions at pH 11.0, measured individually or in a binary mixture.

It was found during bubble-alumina interactions in SDS solution at pH 6.0 (Figure 5-8) that the zeta-potential distribution of the mixing process shifted towards the positive direction as the mixing time was extended from 30 min to 2 hr during which large aggregates were seen to accumulated at the bottom of the mixture. The observed shift in zeta-potential distribution peak

position and enhanced aggregation by extended mixing appear to suggest "bubble-bridging" where tiny bubbles act as bridges in connecting the bubble-alumina aggregates in forming even larger aggregates with more alumina particles exposed towards the bulk solution[58].
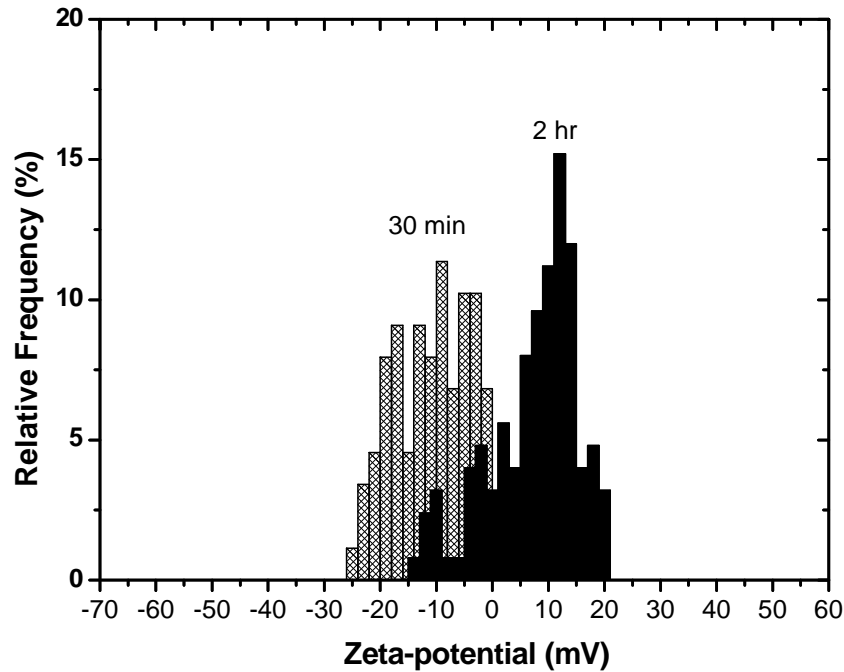
Figure 5-8: Zeta-potential distribution of nano size alumina particles mixed with submicron size bubbles after bubble generation in 0.01 mM SDS + 1 mM KCl solutions at pH 6.5 when mixed for different mixing time.

5.2.1.3 Summary

1) Anionic surfactant SDS was able to adsorb at bubble-water interface in 0.01 mM SDS + 1 mM KCl solutions, making the zeta-potential of bubbles more negative than that in 1 mM KCl solutions. Such negative zeta-potential of bubbles became more negative with increasing pH. Zeta-potential of

alumina in such solutions was positive at pH 6.0. As the pH of the solutions became more alkaline, the zeta-potential of the alumina particles reversed to a negative value and became increasingly negative with increasing pH. Zeta-potential results of alumina particles were very similar in 1 mM KCl solutions with and without SDS addition.

2) Negatively charged bubbles did not attach to the negatively charged silica particles, even when silica particles were treated to become hydrophobic (at pH 6.0) as a result of strongly electrostatic repulsive force.

3) Negatively charged bubbles attached to positively charged alumina particles (at mildly acidic pH) possibly due to electrostatic attractive force, but repel negatively charged alumina particles (at high pH) likely as a result of electrostatic repulsive force.

4) When electrostatic double layer force was strong, *in situ* gas nucleation and mixing process showed similar bubble-particle interaction behaviour. When electrostatic double layer force was weakly repulsive, bubbles only attached to (nucleated on) particles by *in situ* gas nucleation but not by mixing process, suggesting that *in situ* gas nucleation promotes bubble-particle attachment.

5) Mutual effect of the interacting bubbles and alumina particles had different influence on the zeta-potential distributions of binary mixtures, depending on different electrostatic double layer repulsive force present in the system.

6) Zeta-potential of bubble-alumina aggregate changed with increasing mixing time during mixing process, indicating the importance of customizing mixing time for all bubble-particle interactions.

119

5.2.2   DAH Solutions

5.2.2.1 Interactions of Silica and Alumina with Submicron Size Bubbles

Zeta-potential distribution results in 0.01 mM SDS + 1 mM KCl showed that electrostatic double layer force plays a very important role in bubble-particle attachment. Former researchers suggested that at micron/nano scale, electrostatic double layer force becomes dominant in determining interactions among fine particles[16]. In order to further confirm the importance of electrostatic double layer force in determining bubble-particle interactions, DAH solutions of different concentrations were used. Experiments were preformed in the same manner as those in SDS solutions. Zeta-potential distributions of bubble-alumina and bubble-silica in 0.1 mM DAH + 1 mM KCl solutions at pH 6.5 are shown in Figure 5-9.

Shown on the left-hand side of Figure 5-9 are zeta-potential distributions of alumina in 0.1 mM DAH + 1 mM KCl solutions at pH 6.5. In 0.1 mM DAH, zeta-potential distribution of alumina spread between 17 mV and 31 mV and peaked at 23 mV. The decrease in the magnitude of zeta-potential as compared to the case in 1 mM KCl solution (Figure 5-1) is likely the result of electrical double layer compression. When looking at the zeta-potential distribution of bubbles (Figure 5-9), the peak of the distribution was found to be shifted from a negative value to 29 mV. Compared with the data in Figure 5-1, this result shows that abundant amount of DAH adsorbed at bubble-water interface, not only reversing the charge of bubbles, but also reducing the hydrophobicity of the bubble surface.

120

The positively charged heads of these cationic surfactants contributed to the reversed surface charge of bubble from negative to positive.

By mixing the bubbles and alumina at a 1:1 volume ration, a broad unimodal distribution was obtained, stretching between 7 mV ~ 37 mV with a peak around 25 mV. Because zeta-potential distributions of bubble and alumina measured individually were overlapping one another, it is difficult to judge whether there was attachment of the two components.
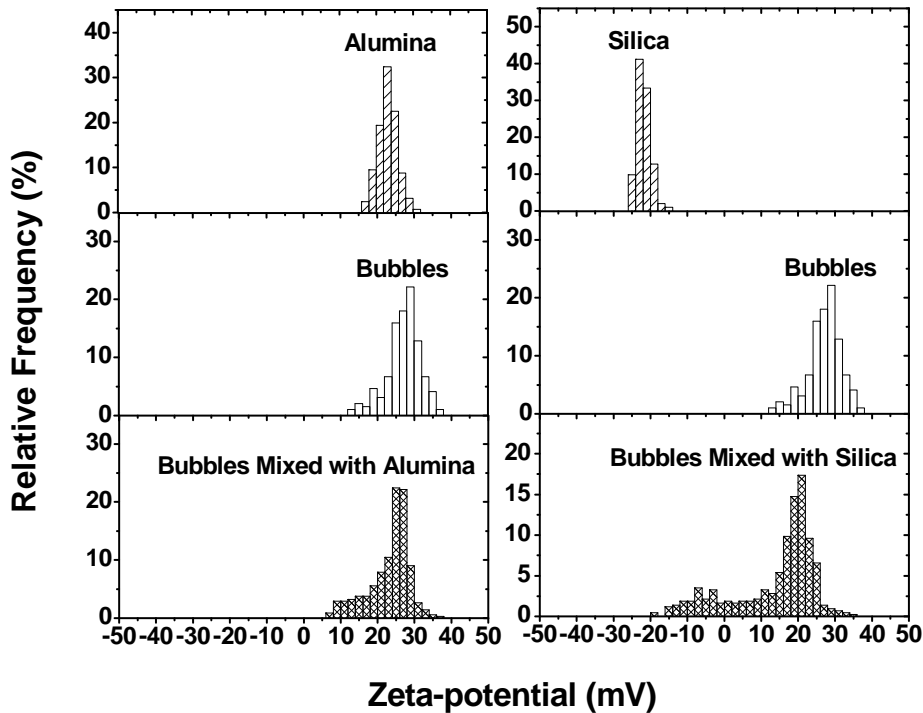
Figure 5-9: Zeta-potential distributions of submicron size bubbles and nano sized alumina and silica particles in 0.1 mM DAH + 1 mM KCl solutions at pH 6.5, measured independently or in a binary mixture.

Figure 5-9 also shows that silica in 0.1 mM DAH + 1 mM KCl solutions had a narrower and sharper distribution ranging between -15 mV and -25 mV

with a peak at -22 mV, in comparison to -30 mV in 1 mM KCl solutions,

suggesting a limited amount of DAH adsorbed on silica. The zeta-potential

distribution at the bottom right of Figure 5-9 indicates that when mixed together,

the binary mixture of bubbles and silica had a very widely spread distribution

with a peak at 21 mV and a tail extending to the position of silica when measured

separately. According to the theory described in Section 3.2.1.4, the zeta-potential

distribution seen here indicates a weak attachment of the two components and a

limited number of individual bubbles and silica particles remain in solution. The

bubble-silica attachment here is highly likely the result of weak electrostatic

attractive force caused by opposite surface charge of bubbles and silica particles.

Effect of DAH Concentration:

Zeta-potential distributions of bubble and silica particles in 10 mM DAH

solutions of pH 6.5 are shown in Figure 5-10. The peak of the zeta-potential

distribution of alumina remained at the positive position of 31 mV. The zeta-

potential of bubbles was however shifted greatly towards the positive direction

when compared with the results from 0.1 mM DAH solution. It is obvious that

DAH further adsorbs at bubble-water interface but not alumina surface. At such

high surfactant concentration, almost the same as cmc (13 mM)[206], the bubble

surface is likely to be mostly covered by surfactants[31]. Thus, instead of being

hydrophobic, the bubble surface is now highly hydrophilic. Moreover, the

zeta-potential of bubbles had a spread out distribution with a broad peak at around

70 mV, suggesting variation of surface charges among individual bubbles

possibly led by excessive DAH adsorption. The graph at the lower left corner of

Figure 5-10 shows the zeta-potential distribution obtained from a mixture of alumina and bubbles in 10 mM DAH + 1 mM KCl solutions. The zeta-potential distribution of the bubble-alumina mixture was obviously bimodal with two apparent peaks with positions and shapes similar to those of alumina and bubbles, measured individually. The results suggest no attachment of the two components as a result of strong electrostatic repulsive force.
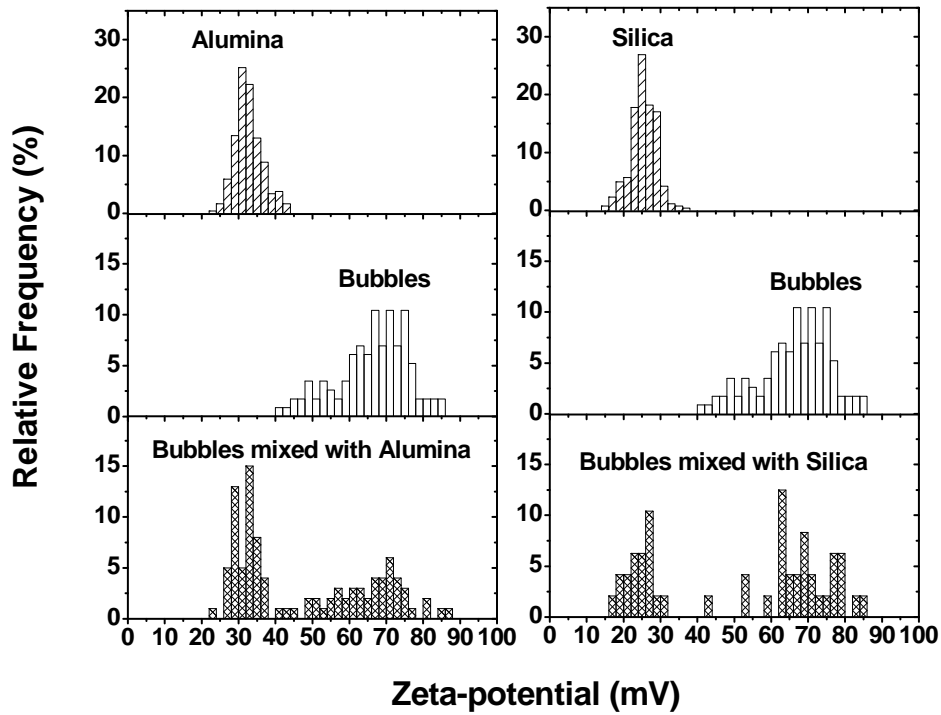

Figure 5-10: Zeta-potential distributions of submicron size bubbles and nano size alumina and silica particles in 10 mM DAH + 1 mM KCl solutions at pH 6.5, measured individually or in a binary mixture.

In the case of silica, as shown on right hand side of Figure 5-10, zeta-potential of silica reversed from a negative value to a positive value, suggesting strong and intensive adsorption of DAH on silica surface. According

to the results reported in literature, bilayer formation could occur at surfactant concentration as low as 1/10 cmc[205, 207]. Thus, in 10 mM (almost the same as cmc) DAH solutions, instead of being made hydrophobic, the silica particles are now hydrophilic due to bilayer formation of surfactant[207]. The zeta-potential distribution of silica particles was narrow with a peak at 25 mV. By mixing the same amount of silica and bubbles together, two separate zeta-potential distribution peaks at 27 mV and 69 mV were observed. Recalling the position of zeta-potential distribution peaks of silica and bubbles at 25 mV and around 70 mV respectively, when measured individually, it is not difficult to conclude that the zeta-potential of the binary mixture distribution was almost an overlay of zeta-potential distributions of silica and bubbles, measured individually. The characteristics of zeta-potential distributions of bubble-silica mixture indicate the absence of bubble-silica attachment. As the hydrophilic silica particles and bubbles were of the same charge and large in magnitude, a strong repulsive force was expected. In general, results in Figure 5-10 indicate that when surface charge of two interacting components were same in sign and large in magnitude, the electrostatic double layer repulsive force dominates bubble-particle interactions and is very effective in prohibiting attachment of the components.

5.2.2.2 Effect of pH

Bubble-silica interactions in 1 mM DAH + 1 mM KCl solutions were studied as a function of pH. The role of *in situ* gas nucleation and mixing process on bubble-silica interactions was investigated according to their resulting

zeta-potential distributions. Acidic pH conditions were used in this study to reduce the negative charge of silica particles.
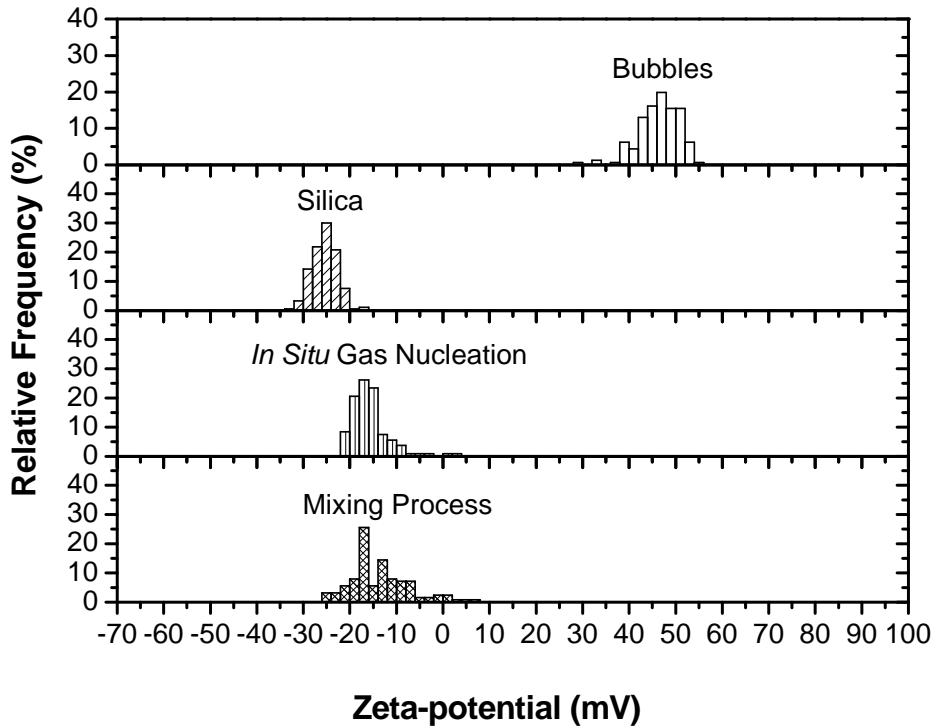
Figure 5-11: Zeta-potential distributions of submicron size bubbles and nano size silica particles in 1 mM DAH + 1 mM KCl solutions at pH 6.5, measured individually or in a binary mixture.

Bubbles in 1 mM DAH + 1 mM KCl solutions at pH 6.5 were positively charged with a zeta-potential distribution peak at 47 mV (Figure 5-11), whereas silica particles were negatively charged with zeta-potential distribution peak at -25 mV (Figure 5-11). As mentioned earlier, some DAH adsorbed on silica surface in this case, while the surface of bubbles was mostly covered by DAH. When bubbles were generated in silica particle suspension by *in situ* gas nucleation, the zeta-potential distribution was located in-between the distributions

of silica and bubbles measured independently with a peak at -17 mV. These results indicate a strong bubble-silica attachment due to electrostatic attraction between oppositely charged components. The more silica-like zeta-potential distribution of *in situ* bubble formation in silica particle suspensions was possibly attributed to formation of larger bubble-silica aggregates, with more silica particles exposed to aqueous phase. It should be noted that the zeta-potential distribution of the mixed silica-bubble suspensions by mixing process were similar to the case of *in situ* gas nucleation.
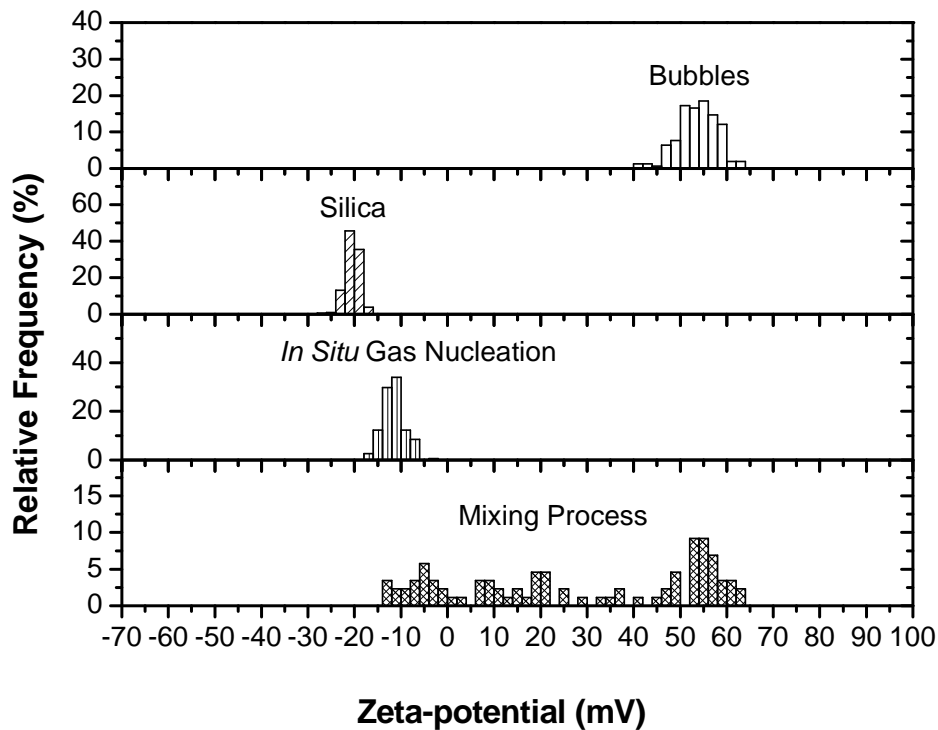
Figure 5-12: Zeta-potential distributions of submicron size bubbles and nano size silica particles in 1 mM DAH + 1 mM KCl solutions at pH 4.0, measured individually or in a binary mixture.

126

Figure 5-12 shows zeta-potential distributions of bubble and silica in the same DAH solution at pH 4.0, measured individually and as a binary mixture. At this low pH, the abundant H^+ ions would make the silica particles less negatively charged while the bubbles more positively charged. As shown in Figure 5-12, zeta-potential distribution of bubbles centered at 55 mV and that of silica at -21 mV. *In situ* gas nucleation had a sharp zeta-potential distribution with a peak value of -11 mV. The situation here is similar to what was shown by *in situ* gas nucleation at pH 6.5 where bubbles and silica particles strongly attached to each other. In contrast, the zeta-potential distribution of a binary mixture of bubble-silica suspension shows a much wider distribution, ranging form -10 mV to 65 mV, almost covering the combined range of zeta-potential measured for silica and bubbles, individually. This zeta-potential distribution of a binary mixture is a strong indication of limited attachment of silica to bubbles by mixing. The weak attachment in this case is possibly due to a decrease in attractive electrostatic double layer force with decreasing zeta-potential difference between the two components. Former study by Atkinson (1973) suggested that cationic surfactant adsorption on silica surface at acidic pH was rather low. Thus, silica in this case remains more hydrophilic than the case of pH 6.5. The lower hydrophobicity might have contributed to the result of weaker attraction. If this was the case, bubble-silica attachment at pH 6.5 was not only the result of attractive electrostatic double layer force, but also the result of hydrophobic force. To confirm the role of surface hydrophobicity in bubble-silica attachment as observed at pH 6.5 but not at pH 4.0, additional tests on hydrophobicity of

bubbles and particles need to be preformed. By comparing the results of *in situ* gas nucleation and mixing process, the effect of i*n situ* gas nucleation in enhancing bubble-particle interactions is evident.
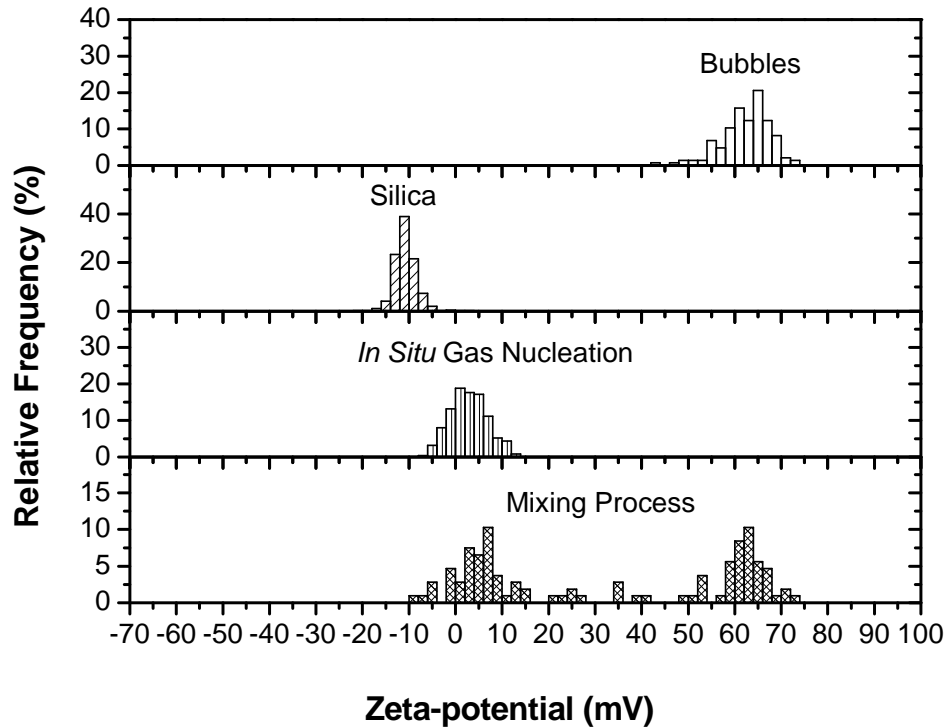

Figure 5-13: Zeta-potential distributions of submicron size bubbles and nano size silica particles in 1 mM DAH + 1 mM KCl solutions at pH 2.1, measured individually or in a binary mixture.

Additional measurement was conducted by further lowering the pH of the DAH solution to pH 2.1. As shown in Figure 5-13, the zeta-potential distribution of silica particles centered at -13 mV, where the peak of zeta-potential distribution for bubbles was further shifted to 65 mV. The zeta-potential distribution of *in situ* gas nucleation remained to be sharp and unimodal and peaked at 5mV, which is similar to the zeta-potential distribution peak of silica as measured individually.

128

Such observation indicates a strong attachment of silica to bubbles, almost fully

covering bubble surfaces. In the case of mixing bubble and silica suspensions of

the same solution chemistry, the bimodal zeta-potential distribution peaks at

pH 4.0 were further separated here to locations of 7 mV and 63 mV which are

almost identical to the distribution peaks of bubbles and silica measured

independently. The results suggest that bubble-particle attachment at pH 2.1 was

further weakened to become negligible or not to exist at all. Again, results here

provide solid evidence that *in situ* gas nucleation enhances bubble-particle
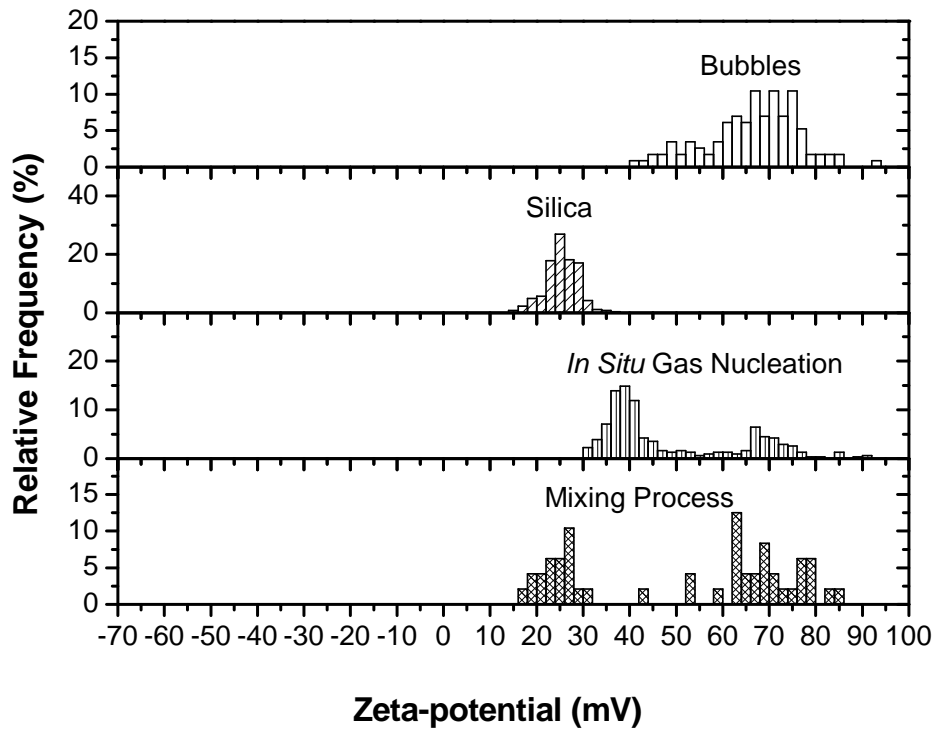
attachment.

Figure 5-14: Zeta-potential distributions of submicron size bubbles and nano size

silica particles in 10 mM DAH + 1 mM KCl solutions at pH 6.5, measured

individually or in a binary mixture.

As mentioned previously in Section 5.2.2.1, no attachment occurred between bubbles and silica particles in 10 mM DAH + 1 mM KCl solutions at pH 6.5 during mixing process as a result of strong electrostatic repulsive force. Figure 5-14 shows that even during *in situ* gas nucleation, bubbles hardly attach to silica particles as shown by a broad bimodal distribution with two peaks at 67 mV and 39 mV, which are almost the same the positions of bubbles and silica measured individually. Since both silica and bubble surfaces were hydrophilic due to formation of DAH bilayer, the bimodal zeta-potential distribution could be easily understood: only few bubbles were nucleated on silica surface due to highly hydrophilic character of silica and the majority of bubbles were generated in the bulk solutions. Due to repulsive electrostatic double layer force, bubbles in the bulk could not attach to silica particles.

5.2.2.3 Summary

1) Cationic surfactant DAH adsorbed at bubble-water interface, which reversed the zeta-potential of bubbles from negative (in 1 mM KCl solutions) to positive and possibly decreased the hydrophobicity of the bubble surface dramatically. DAH were also found to adsorb on silica surface in 0.1 mM DAH and 1mM DAH solutions at neutral pH, whereas a bilayer was likely formed on silica surface 10 mM DAH solutions. The positive zeta-potential of bubbles in both DAH solutions became more positive with decreasing pH. Zeta-potential of silica become less negative and increasingly positive with decreasing pH and increasing DAH concentration from 0.1 mM and 1 mM to 10 mM.

2) Due to electrostatic double layer force: positively charged bubbles did not attach to positively charged alumina but attached to the negatively charged silica particles in 0.1 mM and 1 mM DAH solutions. As the silica particle became positively charged in 10 mM DAH solutions, attachment of bubbles with silica particles was no longer observed.

3) When electrostatic double layer force was strong, *in situ* gas nucleation and mixing process showed similar bubble-particle interaction behaviour. When electrostatic double layer force was weak, bubbles only attached to (nucleated on) particles by *in situ* gas nucleation but not by mixing process, suggesting that *in situ* gas nucleation promotes bubble-particles attachment.

4) Surfactant concentration has large impact on bubble-particle interactions possibly by changing the surface charge and hydrophobicity of the interacting surfaces.

5) Mutual effect of the interacting bubbles and silica particles on zeta-potential distributions of binary mixtures was similar to that found in SDS solutions: under conditions of weak electrostatic double layer repulsive force, the two distribution peaks of a non-aggregating mixture suspension shifted towards each other when compared to positions of the zeta-potential distributions of the two components measured independently.

5.2.3   MIBC Solutions

In order to further distinguish the role of electrostatic double layer force and hydrophobic force in bubble-particle interactions, MIBC, a non-ionic surfactant, was used. In this case, MIBC would only adsorb at gas-water interface,

the negatively charged bubbles would become less hydrophobic due to massive coverage of MIBC molecules and the positively and negatively charged alumina and silica particles would remain hydrophilic. Therefore there should be no source of hydrophobic force within the system. Interactions of submicron size bubbles with silica and alumina particles during both processes of *in situ* gas nucleation and mixing process were studied as a function of pH.

5.2.3.1 Bubble-Alumina Interactions (Effect of pH)

As shown in Figure 5-15, at pH 6.5, submicron size bubbles in 0.1 mM MIBC + 1 mM KCl solution had a zeta-potential distribution peak at -31 mV and alumina had a zeta-potential distribution peak at 33 mV, both distributions were narrow and sharp. Shown in Figure 5-15, the zeta-potential distribution of mixing process had an extremely scattered zeta-potential distribution which spread from -43 mV to 23 mV with no obvious distribution peak. While *in situ* gas nucleation showed a relatively sharp distribution centering at 17 mV. The two mixture distributions provide us with the information that, in mixing process, attachment of the bubbles with alumina particles is weak while the attachment was greatly improved by *in situ* gas nucleation where bubbles directly nucleate on the surface of solid particles. Even though alumina is conventionally considered as hydrophilic here, the roughness of the alumina particles might have triggered bubble formation[60]. This weakened attachment of bubbles with alumina could be caused by weak electrostatic attractive force, effect of relatively high frother concentration, effect of frother itself or a combination of all.
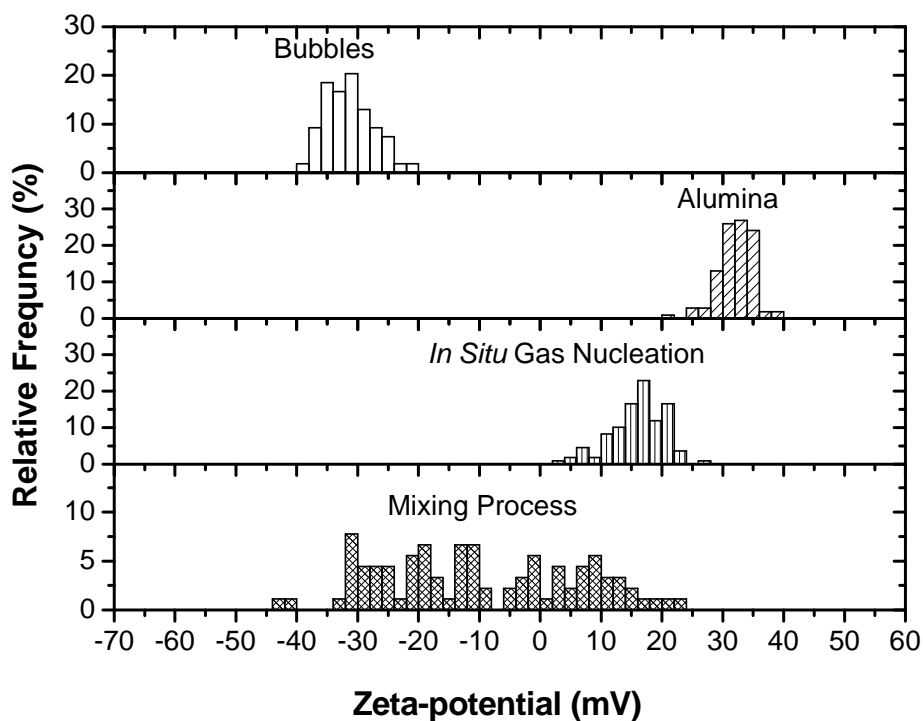
Figure 5-15: Zeta-potential distributions of submicron size bubbles and nano size alumina particles in 0.1 mM MIBC + 1 mM KCl solutions at pH 6.5, measured individually or in a binary mixture.

When the pH of the MIBC solution was adjusted to pH 9.8, the zeta-potential distribution peak of alumina dropped to -13 mV and that of bubbles decreased to -55 mV. The bubble distribution was observed to be much broader with a 30 mV of span while the alumina distribution was still relatively sharp. Similar patterns in zeta-potential distributions of *in situ* gas nucleation and mixing process here with those at pH 6.5 were observed, suggesting strong bubble-alumina attachment during *in situ* gas nucleation and weak attachment in mixing process. The extremely broad zeta-potential distribution of mixing process at pH 6.5 had further developed from a scattered distribution into a bimodal one at

pH 9.8, of which the peaks were located at -58 mV and -26 mV, respectively. The

two distribution peaks of mixing process indicate large portion of freely

suspended bubbles and alumina as only very few of the components attached. As

mentioned previously in Section 5.2.1.3 and Section 5.2.2.3, the shift in position

of peak at -26 mV from the original position of the alumina distribution peak

(-13 mV) is likely the mutual effect of interacting components under weak

electrostatic double layer force. As for *in situ* gas nucleation, bubbles continue to

nucleate on alumina surface.
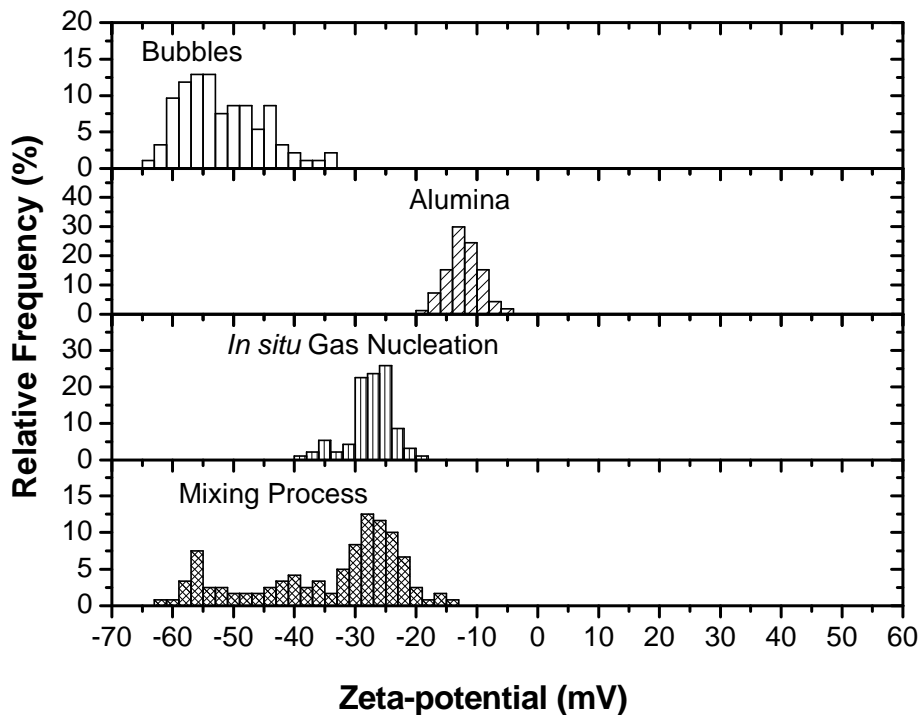
Figure 5-16: Zeta-potential distributions of submicron size bubbles and nano size

alumina particles in 0.1 mM MIBC + 1 mM KCl solutions at pH 9.8, measured

individually or in a binary mixture.
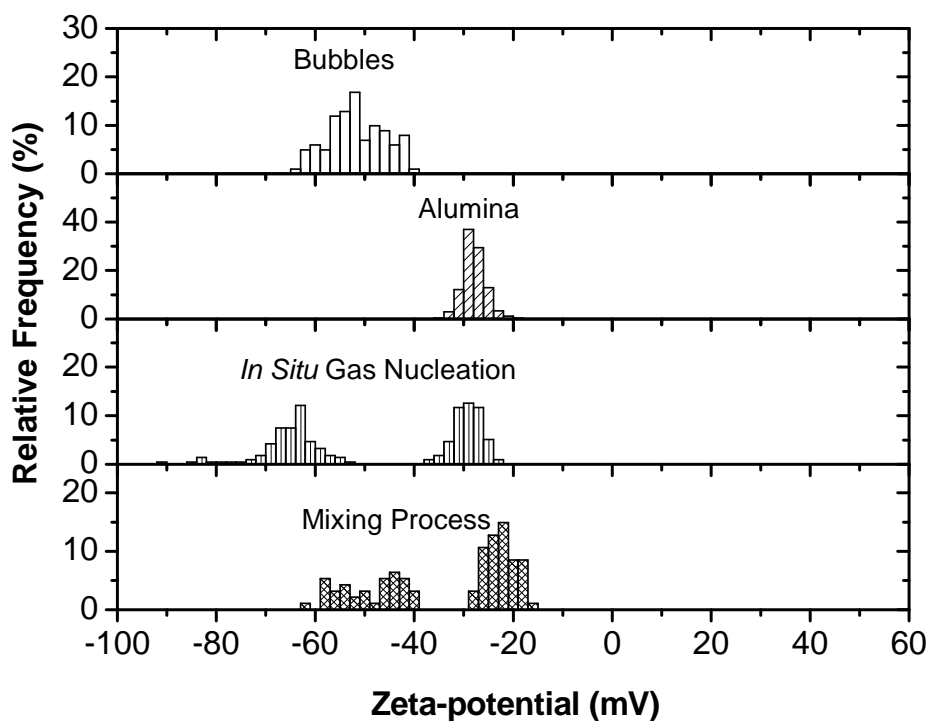
Figure 5-17: Zeta-potential distributions of submicron size bubbles and nano size alumina particles in 0.1 mM MIBC + 1 mM KCl solutions at pH 11.0, measured individually or in a binary mixture.

Figure 5-17 demonstrates bubble-alumina interactions in MIBC solutions of pH 11.0 where both the bubbles and alumina particles were negatively charged. The zeta-potential distribution peaks of bubbles and alumina particles were located at -54 mV and -29 mV, correspondingly. It is provided in Figure 5-17 that the zeta-potential of air bubbles became less negative if compared with the value obtained at pH 9.8. This is possibly due to compression of the electrical double layer led by high electrolyte concentration, as the conductivity of the solution increased form originally about 0.195 mS/cm at pH 9.8 to around 0.562 mS/cm at pH 11.0. Both *in situ* gas nucleation and mixing process showed two independent

zeta-potential distribution peaks, almost identical to those of bubbles and alumina particles when measured individually. The more negative distribution peak represents freely suspended bubbles and the less negative one corresponds to free alumina particles. Such results suggest that no attraction is found among the bubbles and alumina due to strong repulsive electrostatic double layer force. As a result of highly hydrophilic surfaces, bubbles were no longer nucleated on the surface of alumina particles. The positions of the distribution peaks of *in situ* gas nucleation and mixing processes further agreed with our previous finding of the inter-component mutual effect, where the two distribution peaks of a non-aggregation mixture part from each other when electrostatic double layer force is strong.

5.2.3.2 Bubble-Silica Interactions (Effect of pH)

A similar group of experiments was performed by using submicron size gas bubbles and silica particles. Figure 5-18 gives the details of bubbles interacting with silica in 0.1 mM MIBC + 1 mM KCl solutions at pH 6.5. Both silica and bubbles were negatively charged with zeta-potential distributions overlapping each other. The zeta-potential distribution of bubbles was much wider and more scattered with a range from -44 mV to -18 mV. The peak of the sharp silica distribution was at -29 mV. Both processes of *in situ* gas nucleation and mixing showed a unimodal distribution as broad as that of independently measured bubbles. Since all four distributions were very close to one another, it is difficult to identify whether there was an attachment. However, according to our

136

previous results and discussion, it is more likely that a stable suspension of freely

suspended submicron size bubbles and silica particles was formed.
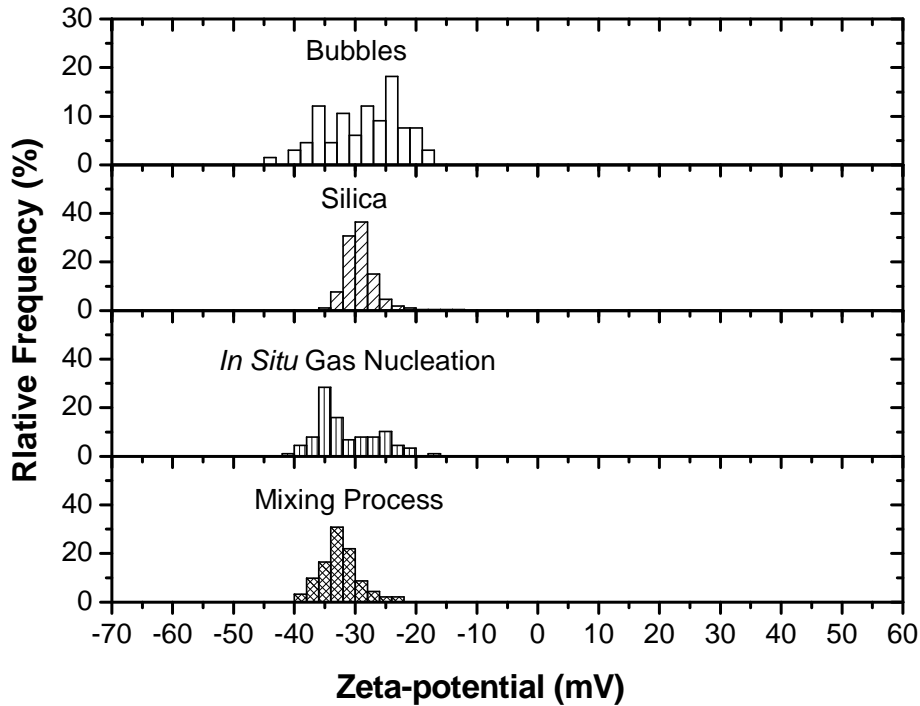
Figure 5-18: Zeta-potential distributions of submicron size bubbles and nano size

silica particles in 0.1 mM MIBC + 1 mM KCl solutions at pH 6.5, measured

individually or in a binary mixture.

  As the pH of the solution was lowered to pH 4.0, both zeta-potential

distribution peaks of bubbles and silica particles had shifted to less negative

positions at -15 mV and -27 mV, respectively (Figure 5-19). The zeta-potential

distribution of bubbles was still scattered while the silica distribution remained

sharp. *In situ* gas nucleation and mixing process resulted in the similar zeta-

potential distributions under current circumstances, of which both showed two

adjacent distribution peaks with one around -25 mV and the other at -11 mV.

Such peaks correspond with those of silica and bubbles when separately measured, thus indicating no obvious attachment among the two components when mixed together. The two distribution peaks of both *in situ* gas nucleation and mixing process were shifted towards each other for the reason of inter-component mutual effect under weak electrostatic repulsion.
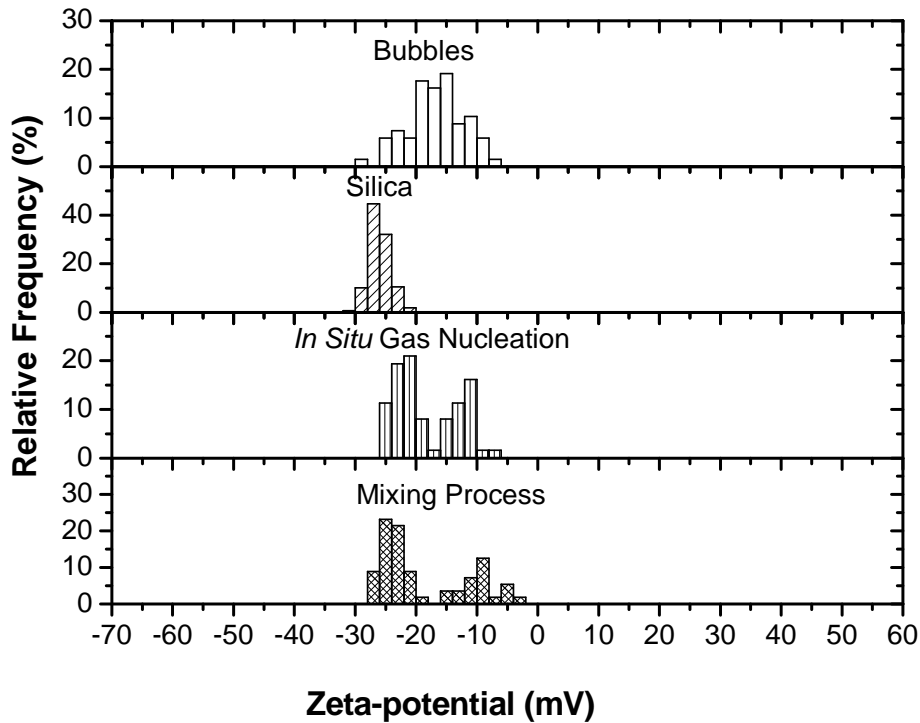
Figure 5-19: Zeta-potential distributions of submicron size bubbles and nano size silica particles in 0.1 mM MIBC + 1 mM KCl solutions at pH 4.0, measured individually or in a binary mixture.

From results in Figure 5-20, it is shown that at pH 2.1, the zeta-potential distribution peak of the submicron size bubbles shifted to around 0 mV while that of the silica particles shifted to -16 mV. Since the zeta-potential of both components were in the unstable zone of colloidal systems[194, 208], it is debatable

138

whether there would be an attachment. Compared with zeta-potential distributions of the individual components as provided in Figure 5-20, the broad and scattered distributions of *in situ* gas nucleation and mixing process suggest weak attachment among bubbles and particles in the mixture. However, it is obviously shown here that, though both *in situ* gas nucleation and mixing process showed weak adhesive behaviour of bubbles and silica, bubble-silica attachment was considerably enhanced by *in situ* gas nucleation. The zeta-potential distribution of *in situ* gas nucleation showed bubble-nucleated silica surface while that of mixing process is more likely the result of loosely associate bubbles and silica particles. According to literature, components of colloidal suspension within the unstable zone have large tendency to aggregate due to weak electrostatic double layer repulsive force and Van der Waals attractive force[76].

However, it is important to note that MIBC, of which the ccc was 0.11 mM[209], was less effective in producing stable, uniformed and larger amount of submicron size bubbles when comparing with SDS and DAH. Hence a better frother needs to be applied for better interpretation of results.
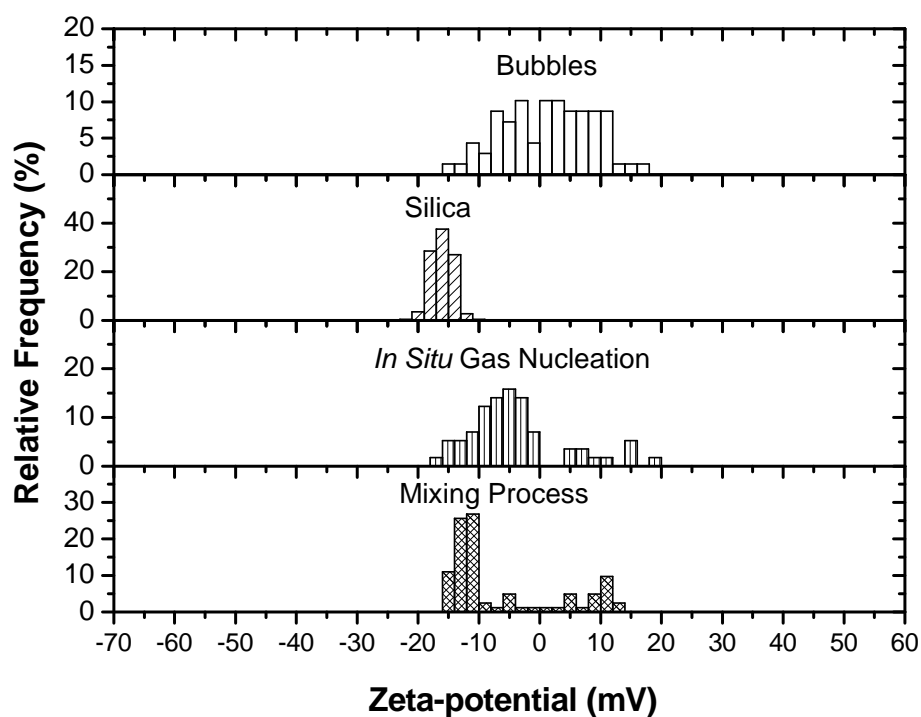
Figure 5-20: Zeta-potential distributions of submicron size bubbles and nano size silica particles in 0.1 mM MIBC + 1 mM KCl solutions at pH 2.1, measured individually or in a binary mixture.

5.2.3.3 Summary

1) MIBC addition has a weak influence on zeta-potential distribution of submicron size bubbles and silica and alumina particles. Bubbles and silica particles in 0.1 mM MIBC + 1 mM KCl solutions are negatively charged while alumina particles are positively charged at most pHs and reversed to be negatively charged after 9.8.

2) Electrostatic double layer force still played a dominant role in determining bubble-particle interactions in MIBC solutions. Negatively charged submicron

size bubbles attached to positively or slightly negatively charged alumina

particles at pH 6.5 and 9.8, respectively. Negatively charged bubbles repelled

negatively charged silica (pH 6.5, 4.0) and alumina particles (pH 11.0).

Neutral bubbles attached to slightly negatively charged silica particles at

pH 2.1.

3) *In situ* gas nucleation enhanced bubble-particle attachment when repulsive
electrostatic double layer force was weak while *in situ* gas nucleation and
mixing process showed similar bubble-particle interactions under strong
electrostatic double layer force.

4) Frother type and concentration may play a critical role in determining bubble-
particle interactions. They might have different effect on bubble-particle
attachment by *in situ* gas nucleation and mixing process.

5) MIBC was a less effective surface active agent in producing preferable
zeta-potential distribution of submicron size bubbles, thus improving accuracy
of the zeta-potential distribution analysis is required.

6) Inter-component mutual effect on zeta-potential distributions of
bubble-particle binary mixture in MIBC solutions was similar to that in SDS
and DAH solutions.

5.2.4   DF250 Solutions

Aiming to improve submicron size bubble generation and study the effect

of frother type on bubble-particle interactions, DF250 was used at the same

concentration of 0.1 mM (in 1 mM KCl) as with MIBC. The selected

concentration was about three times the ccc of DF250[209]. Using DF250 increased

the number of submicron size bubbles generated by 3 ~ 4 times the amount generated in MIBC solutions. Attachment of submicron size bubbles with alumina and silica nano particles were studied as a function of pH. The effect of *in situ* gas nucleation and mixing process on bubble-particle attachment was also studied.

5.2.4.1 Bubble-Alumina Interactions (Effect of pH)

Similar to MIBC, DF250 was anticipated to adsorb at bubble-water interface and reduce the surface hydrophobicity of bubbles, whereas its effect on alumina particles would be minimal. In this way, the predominant force of bubble-alumina interaction in 0.1 mM DF250 + 1 mM KCl solutions was expected to be limited to electrostatic double layer force.

Based on the results in Figure 5-21 ~ Figure 5-24, the zeta-potential distribution peak of bubbles in 0.1 mM DF250 + 1 mM KCl solutions at pH 6.5 was at -37 mV. As the pH of solutions increased to pH 8.5, pH 9.8 and pH 11.0, the peak position of bubble zeta-potential distribution shifted in the negative direction to -49 mV, -52 mV and -58 mV, respectively. Except for the case of pH 6.5 where the zeta-potential distribution of bubbles was relatively sharp, the bubble zeta-potential distribution was widely spread and flat for all other pH conditions. Alumina in 0.1 mM DF250 + 1 mM KCl solutions at pH 6.5 had a zeta-potential distribution centering at 33 mV which is similar to the value measured in 1 mM KCl solution. As the pH of solution increased to three more alkaline conditions (pH 8.5, 9.8, 11.0), the zeta-potential distribution peak of alumina also moved to left, with corresponding positions at 7 mV, -9 mV and -25 mV, respectively. Over the selected pH range, the zeta-potential

distributions of alumina particles remained narrow and sharp. The iep of alumina in 0.1 mM DF 250 was found to be between pH 8.5 and pH 9.8.

Figure 5-21 shows that both *in situ* gas nucleation and mixing process at pH 6.5 had unimodal zeta-potential distribution which indicates a strong bubble-alumina attachment. In contrast, zeta-potential distributions in all alkaline pHs exhibited bimodal distributions for both processes as shown in Figure 5-22 ~ Figure 5-24. These distributions suggest a weak bubble-alumina attachment or no attachment at all between the two components. By comparing the four figures here, *in situ* gas nucleation and mixing had identical zeta-potential distributions at all four pHs. There is no enhanced bubble-alumina interaction by *in situ* gas nucleation. As the pH gradually increases from 8.5 to 11.0, due to increasing electrostatic repulsive force, the zeta-potential distribution peaks further differentiate to become located at the same zeta-potential values as bubbles and alumina particles measured separately, suggesting freely suspended bubbles and particle in the mixture. When looking at the four pH conditions independently, four cases are described as: at pH 6.5 (Figure 5-21), negatively charged bubbles strongly attached to positively charged alumina as a result of electrostatic attractive force; at pH 8.5 (Figure 5-22), negatively charged bubbles barely attached to almost neutral alumina particles due to lack of electrostatic repulsion or attraction; at pH 9.8 (Figure 5-23) negatively charged bubbles did not attach to negatively charged alumina particles due to electrostatic repulsive force; and at pH 11.0 (Figure 5-24), the very negatively charged bubbles and alumina particles in mixture repelled each other due to strong electrostatic repulsive force. The

inter-component mutual effect on zeta-potential distributions of mixed systems remained obvious as when electrostatic repulsive force increased from moderate to strong, the two distributions of *in situ* gas nucleation and mixing process changed from shifting toward each other to away from each other.
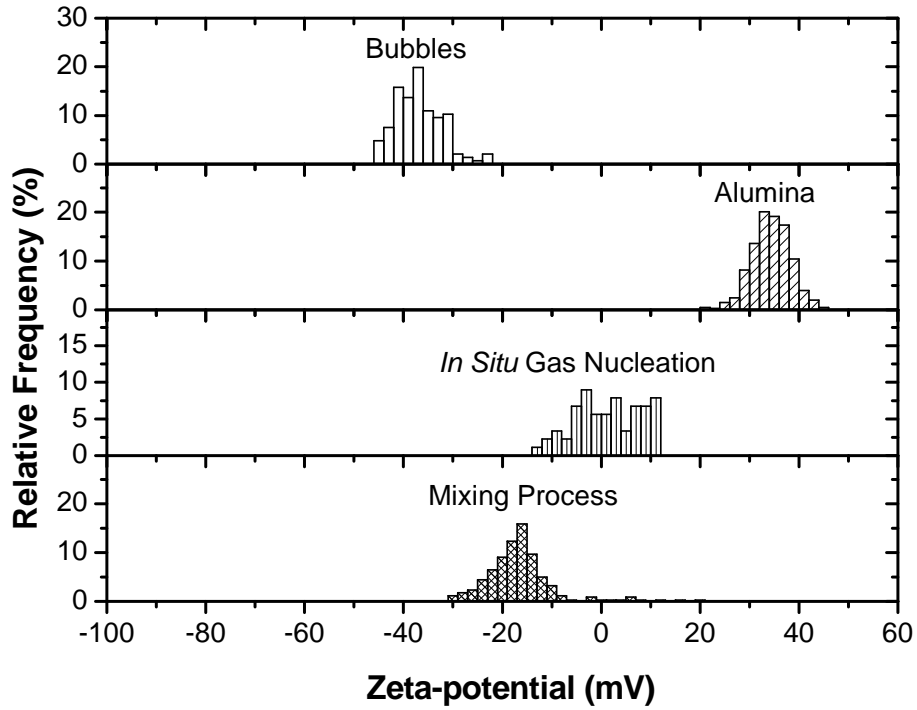
Figure 5-21: Zeta-potential distributions of submicron size bubbles and nano size alumina particles in 0.1 mM DF250 + 1 mM KCl solutions at pH 6.5, measured individually or in a binary mixture.
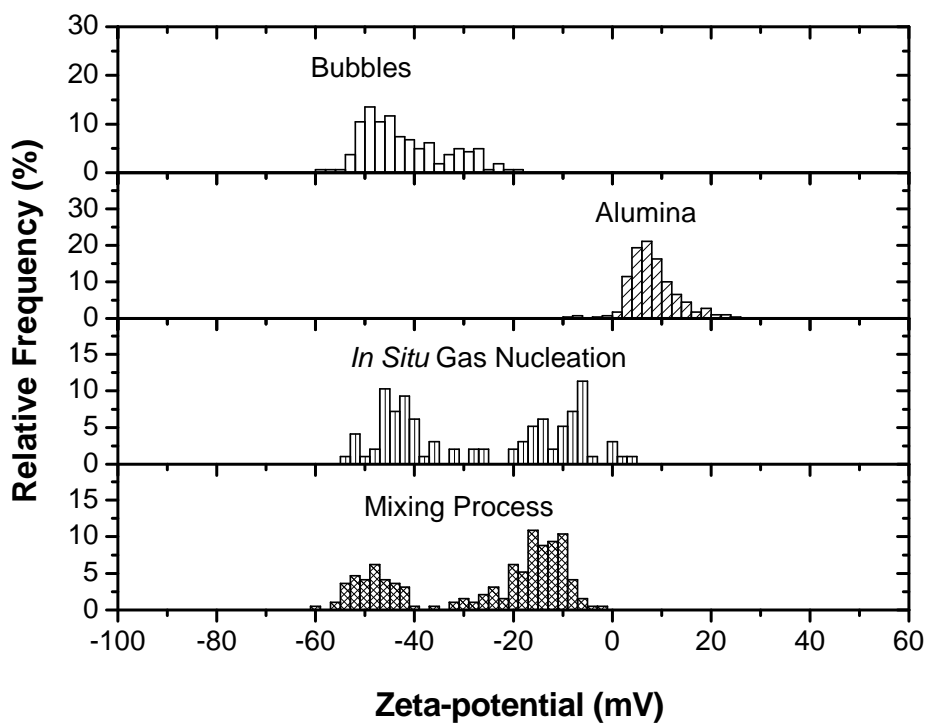
Figure 5-22: Zeta-potential distributions of submicron size bubbles and nano size alumina particles in 0.1 mM DF250 + 1 mM KCl solutions at pH 8.5, measured individually or in a binary mixture.
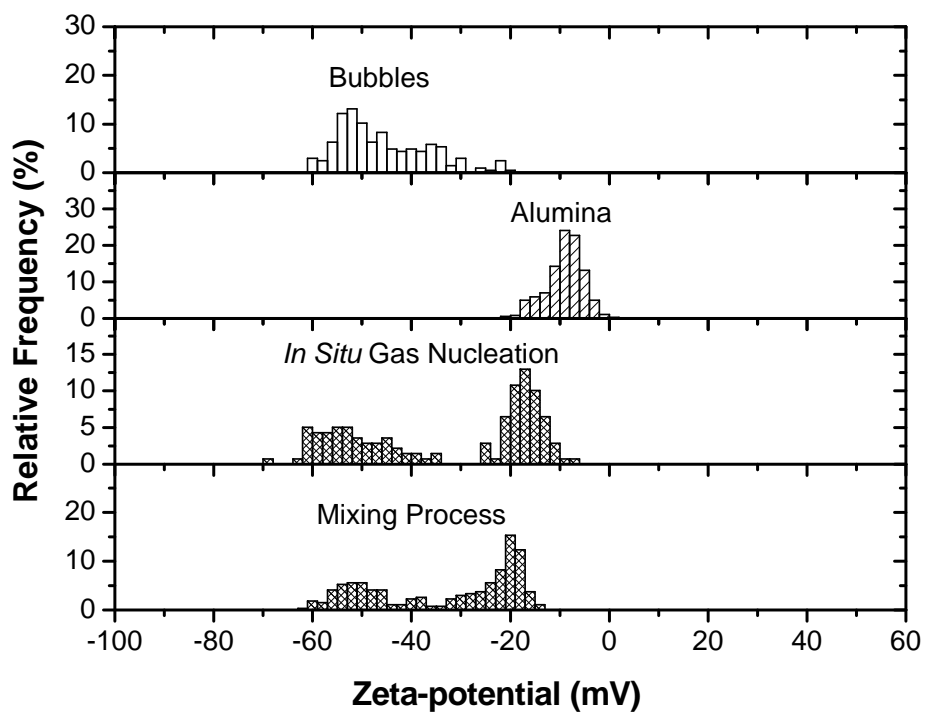
Figure 5-23: Zeta-potential distributions of submicron size bubbles and nano size alumina particles in 0.1 mM DF250 + 1 mM KCl solutions at pH 9.8, measured individually or in a binary mixture.
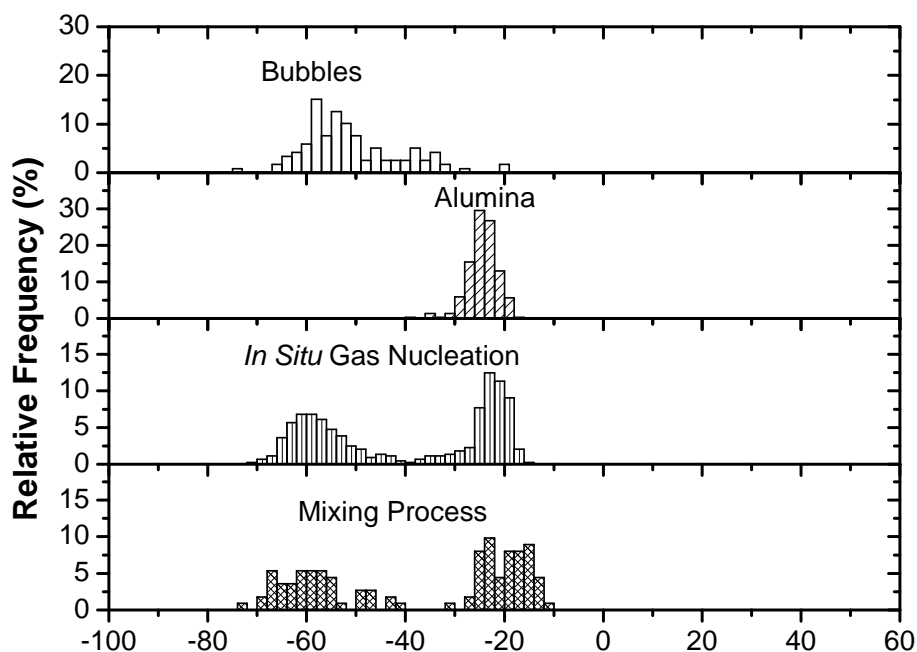
Figure 5-24: Zeta-potential distributions of submicron size bubbles and nano size alumina particles in 0.1 mM DF250 + 1 mM KCl solutions at pH 11.0, measured individually or in a binary mixture.

Recalling the results of bubble-particle interaction in MIBC (Figure 5-15 ~ Figure 5-17), it appears that MIBC weakened bubble-alumina interactions during mixing process and DF250 inhibited the bubble nucleation on particle surface during *in situ* gas nucleation. However, the reason for such effects remains unclear at this stage of investigation.

5.2.4.2 Bubble-Silica Interactions (Effect of pH)

In the same manner, interactions of submicron size bubble with silica particles were studied by conducting measurement in 0.1 mM DF250 + 1 mM

KCl solutions. Similar to bubble-alumina interaction systems, DF250 was expected to only affect bubble-water interface not silica surfaces.

As shown in Figure 5-25 to Figure 5-28, negatively charged silica particles in 0.1 mM DF250 + 1 mM KCl solutions had zeta-potential distributions that were relative narrow and sharp. When pH of the solutions changed from pH 6.5 to 8.5, the zeta-potential distribution peak of silica changed form -26 mV to -30 mV. From the results in Figure 5-25 and Figure 5-26, zeta-potential distributions of *in situ g*as nucleation and mixing process at these two pHs were both bimodal and looked almost the same. Such distributions, with the two peaks at zeta-potential values peaked by bubbles and silica particles measured independently, indicate the absence of attachment between the two components when mixed together. Strong electrostatic repulsion between similarly charged bubbles and silica particles is responsible for the lack of attachment. The slight shift in the peak position corresponding to silica peaks at pH 6.5 in both the *in situ* gas nucleation and mixing process is highly likely the result of inter-component mutual effect.

Figure 5-27 and Figure 5-28 show zeta-potential distribution results of bubble-silica interactions at pH 4.0 and pH 2.1, respectively. The zeta-potential distributions of bubbles and silica particles at pH 4.0 and pH 2.1 were centered at -27 mV (bubble), -21 mV (silica), -15 mV (bubble) and -17 mV (silica), respectively. The zeta-potential distribution peaks of bubbles and silica particles were located extremely close to each other under such two pH conditions. Considering the limitations of the zeta-potential distribution analysis technique,

the technique is not applicable to situations like the case here as there was no gap

for identification of an attachment process. By looking at the results of

bubble-silica interactions by *in situ* gas nucleation and mixing process as shown

in Figure 5-27 and Figure 5-28, no conclusive information of bubble-silica

interactions could be extracted.
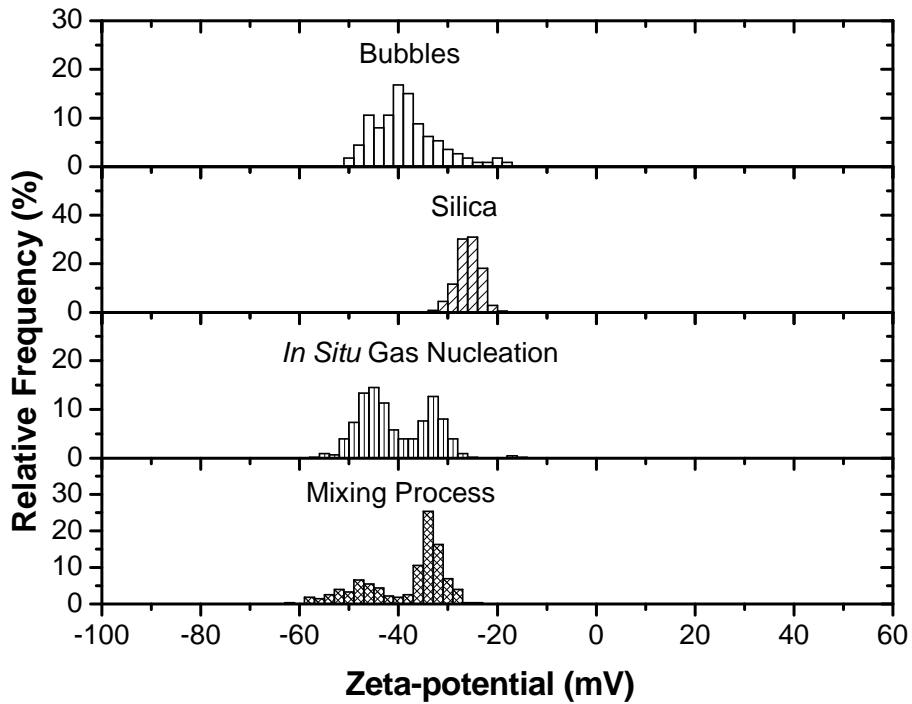
Figure 5-25: Zeta-potential distributions of submicron size bubbles and nano size

silica particles in 0.1 mM DF250 + 1 mM KCl solutions at pH 6.5, measured

individually or in a binary mixture.
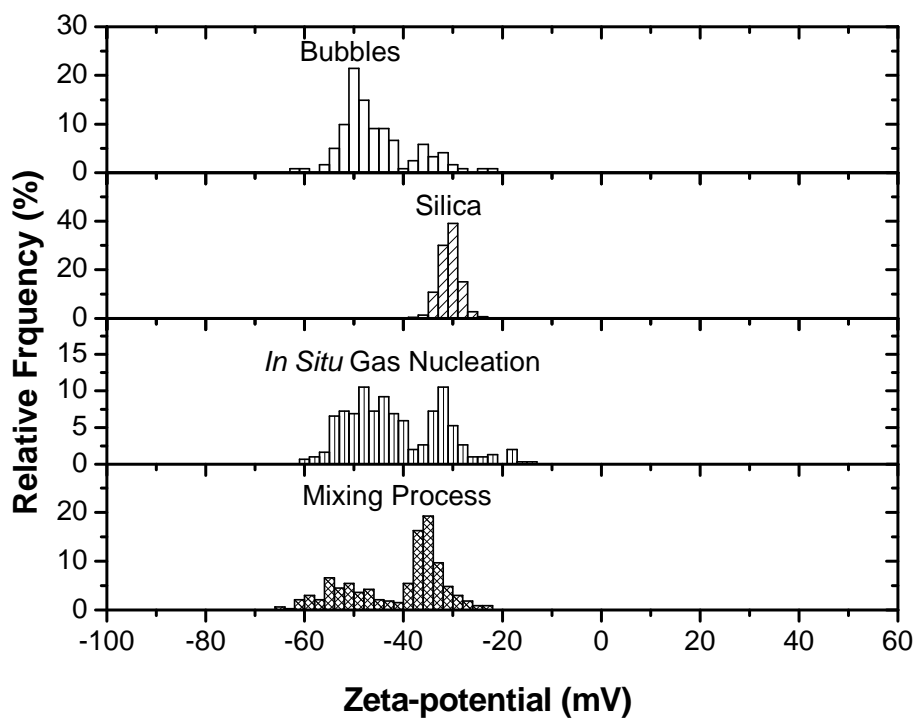
Figure 5-26: Zeta-potential distributions of submicron size bubbles and nano size silica particles in 0.1 mM DF250 + 1 mM KCl solutions at pH 8.5, measured individually or in a binary mixture.
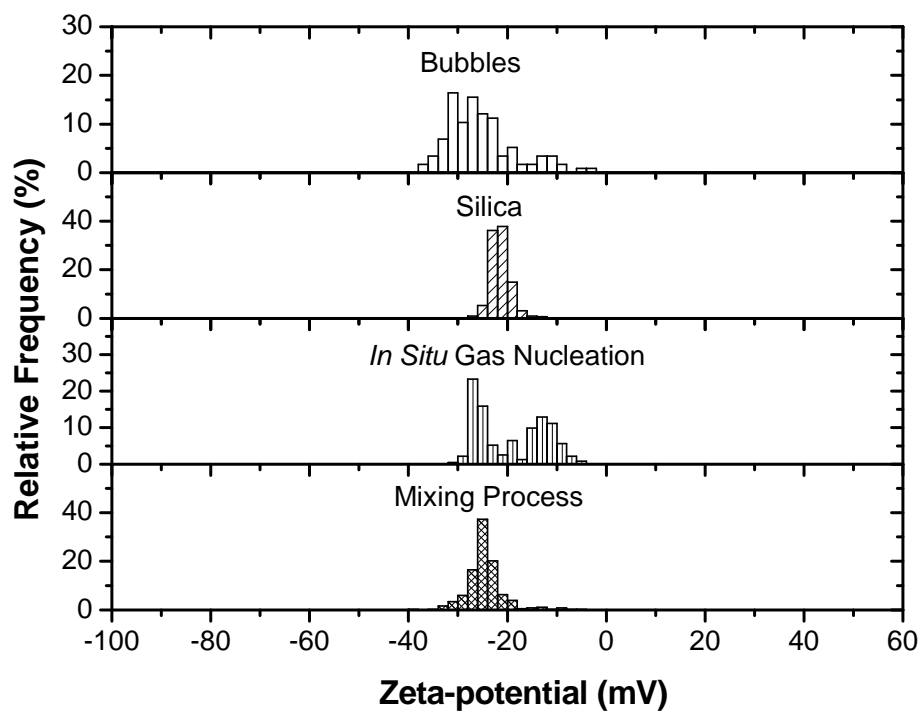
Figure 5-27: Zeta-potential distributions of submicron size bubbles and nano size silica particles in 0.1 mM DF250 + 1 mM KCl solutions at pH 4.0, measured individually or in a binary mixture.
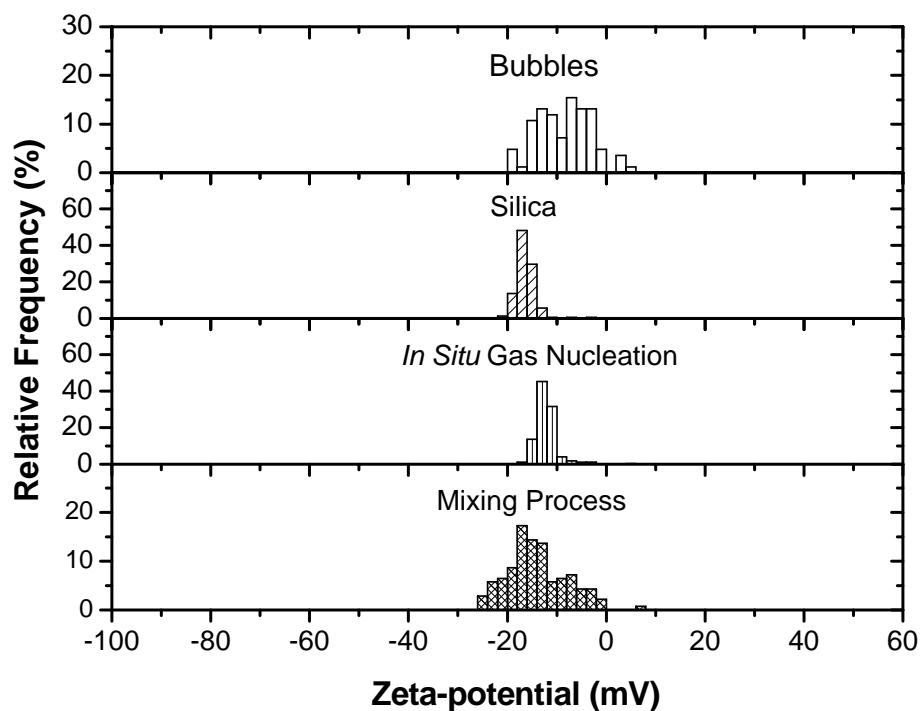
Figure 5-28: Zeta-potential distributions of submicron size bubbles and nano size silica particles in 0.1 mM DF250 + 1 mM KCl solutions at pH 2.1, measured individually or in a binary mixture.

To determine the role of hydrophobic force in bubble-particle interactions, study on interactions between bubbles and highly hydrophobic carbon black particles as a function of pH was attempted. Unfortunately, the zeta-potential distributions of bubbles and carbon black particles were similar, thus the zeta-potential distribution technique was not applicable. The results of this group of experiments did not provide much valuable information. The results of bubble-carbon black interactions are given in Appendix I for your information.

5.2.4.3 Selective Interactions of Submicron Size Bubbles with Alumina and Silica Particles

As shown by the binary results of bubble-particles interaction system of this work, negatively charged bubbles only attached to positively charged alumina particles but not negatively charged silica due to electrostatic double layer force. However, the case in the real world is always much more complicated and bubble-particle interaction systems could involve bubbles and various types of solid particles. Thus it is important to us to find out whether the role of electrostatic double layer force remains as distinct and dominant when both electrostatic attractive force and electrostatic repulsive force are present. For this purpose, zeta-potential distribution measurements were conducted on a ternary system of submicron size bubbles with micron size alumina and silica particles in 1 mM DF250 + 1 mM KCl solutions of pH 6.5.

As shown in Figure 5-29, in a binary mixture of micron size silica and alumina particles, these two particles did not attach to each other. Similar to our previous findings, in binary mixtures of bubble-silica and bubble-alumina, bubbles repelled micron size silica particles while attached to micron size alumina particles. The zeta-potential distribution of the ternary system of bubbles, alumina and silica shows clearly a bimodal distribution with one peak at the same position of micron size silica particles, the other at the same position of a bubble-alumina mixture. It is therefore evident that negatively charged bubbles selectively attached to the positively charged micron size alumina particles while leaving the negatively charged micron size silica particles freely suspended in the mixture.

The role of electrostatic double layer force in bubble-particle interactions is clearly demonstrated, and could be precisely differentiated between attractive force and repulsive force which works independently without interfering with each other.
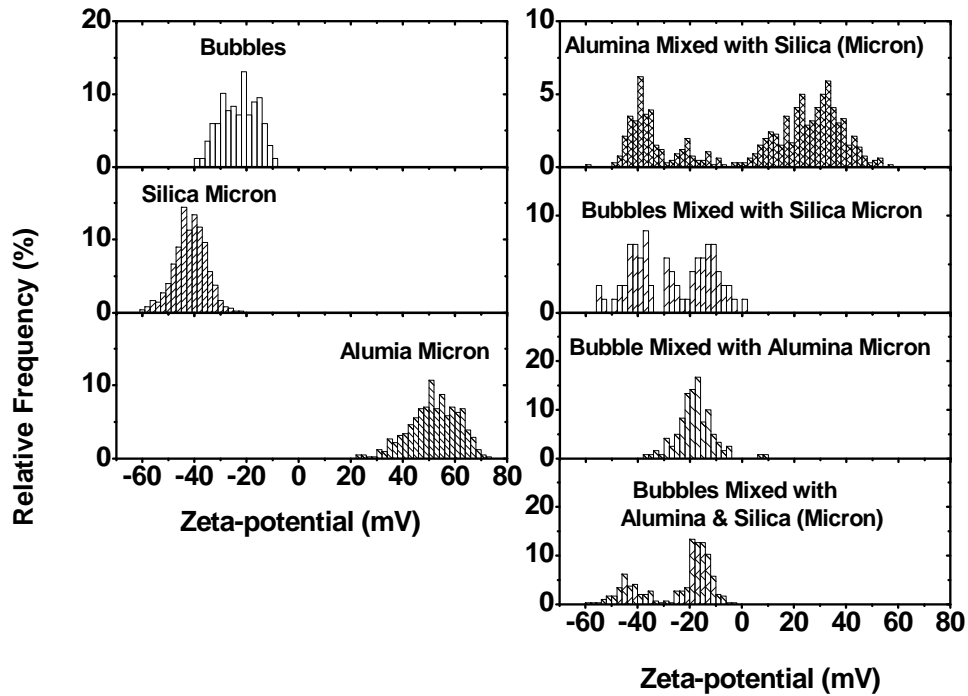
Figure 5-29: Ternary interaction system of submicron size bubbles, micron size silica and alumina particles in 0.1 mM DF250 + 1 mM KCl solutions at pH 6.5.

5.2.4.4 Summary

1) DF250 had better bubble generation proficiency than MIBC in producing larger number of submicron size bubbles. However, the surface charge of bubbles generated using 0.1 mM DF250 + 1 mM KCl solutions still showed broad distributions.

2) DF250 affected zeta-potential of submicron size bubbles by adsorbing at bubble-water interface, whereas the effect of DF250 on zeta-potential of alumina and silica particles was negligible.

3) Electrostatic double layer force was further proved to play a dominant role in determining bubble-particle attachment in DF250 solutions. Negatively charged submicron size bubbles attached to positively charged alumina particles but did not attach to negatively charged silica and alumina particles. Unlike the case of MIBC, negatively charged bubble did not attached to almost neutral alumina particles either. In a ternary system of bubble, alumina and silica, the negatively charged bubbles selectively attached to positively charged micron size alumina particles but not negatively charged micron size silica particles.

4) *In situ* gas nucleation and mixing process resulted in identical bubble-particle interaction patterns in DF250 solutions. No enhanced bubble-particle attachment by *in situ* gas nucleation was found.

5) DF250 and MIBC at the same concentration of 0.1 mM had different effect on bubble-particle attachment. DF250 weakened bubble-alumina attachment during *in situ* gas nucleation, while MIBC weakened bubble-alumina attachment during mixing process.

6) Zeta-potential distribution analysis technique was found to be not suitable for studying the case of bubble-silica attachment at acidic pH as both components had similar zeta-potential values.

5.3　Process Water and Tailings Water

As we've already proven earlier in our work that the zeta-potential distribution analysis technique is capable of determining the bubble-solid interactions in simple electrolyte solutions and surfactant solutions, our following step was to try to apply the technique to more real-world situations by using industrial process water and tailings water as the aqueous environment. Experiments in this section were preformed as described in Section 3.2.1.4.

5.3.1　Zeta-Potential of Single Components in FPW

As shown in Figure 5-30, zeta-potential of alumina changed from mostly positive in 1 mM KCl to mostly negative when measured in FPW. The zeta-potential values of alumina shifted between 0 mV at pH 2.5 and -20 mV at a higher pH. The zeta-potential of silica in FPW fluctuated between -8 mV ~ -24 mV, which was in general less negative than it was measured in 1 mM KCl. Zeta-potential of both silica and alumina decreased moderately as the pH of the solution increased. A more distinct decrease in the alumina zeta-potential occurred within pH 2.5 ~ pH 4.5 as the value started to level off after the range. The effect of pH on the silica zeta-potential was only evident before pH 6.5. Such results suggest that surface properties of alumina and silica particles changed greatly as an effect of the complex water chemistry of FPW.

Bubbles were negatively charged in both 1mM KCl solution and FPW (Figure 5-30) while the zeta-potential of bubbles was considerably more negative in KCl solutions than in FPW. Thus, it is clear that FPW also affected the surface properties of submicron size bubbles possibly by both compression of the

electrical double layer and surfactant adsorption at bubble-water interface. Similar to those of alumina and silica particles, zeta-potential of bubbles also decreased slightly with increasing pH. However, it is also provided in Figure 5-30 that silica, alumina and bubbles all had very similar zeta-potential which ranged between 0 mV ~ -20 mV in FPW. Therefore it is highly likely that studying of bubble-particle interactions in FPW by zeta-potential distribution measurements would face apparent difficulties.
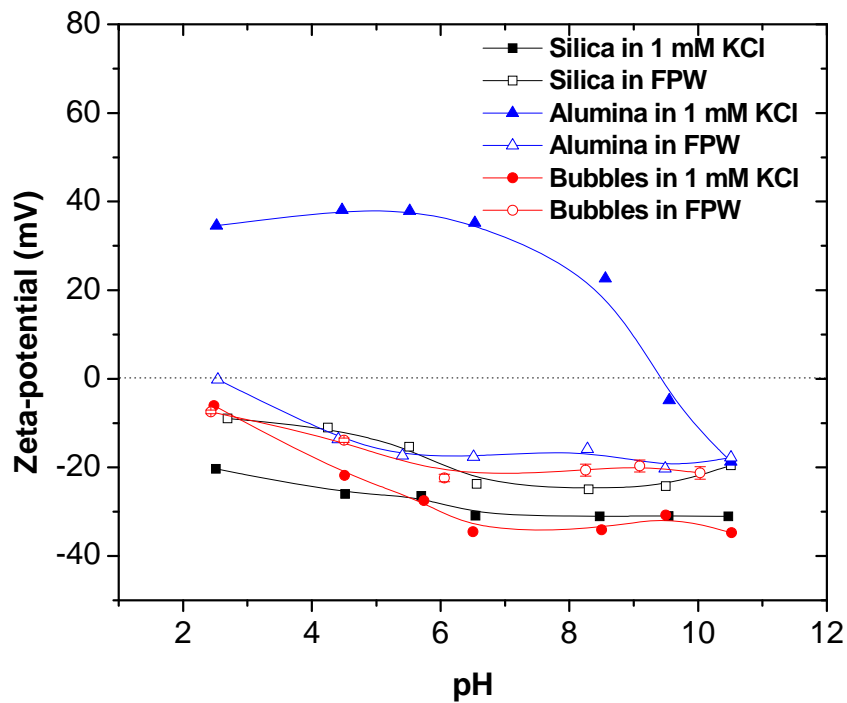
Figure 5-30: Zeta-potential of submicron size bubbles and nano size alumina and silica particles measured in FPW as a function of pH, given in comparison of those measured in1 mM KCl solutions.

5.3.2   Bubble-Particle Interactions in Process Water

Figure 5-31 describes the interaction between submicron size bubbles and nano sized silica and alumina particles in FPW. As shown in the figure, bubbles, alumina particles and the binary mixture of the two components all had a zeta-potential distribution peak around -15 mV. All three distributions were overlapping each other making it very hard to determine whether an attached had occurred. In the case of bubble-silica interaction system, the separation distance between the zeta-potential distribution peaks of silica particles and bubbles were large enough for distinguishing attachment behaviour if all distributions were narrow and sharp. The binary mixture of bubble-silica was shown to have a broad distribution stretching from -31 mV to -9 mV, covering the combined range of individual zeta-potential distributions of bubbles and silica particles. One of the zeta-potential distribution peaks of bubble-silica mixture was observed to be located very closely to the position of the zeta-potential distribution of independently measured silica while the other was found to concentrate between -23 mV ~ -15 mV indicating freely suspended bubbles. Such zeta-potential distribution suggests either very weak attachment or no attachment at all; however, results here more likely refer to repulsion among bubbles and silica particles due to strong repulsive electrostatic double layer force. Hydrophobic force may also play an important role in bubble-particle interactions in FPW due to presence of natural surfactants, but up till now, the effect of hydrophobic force could not be fully determined.
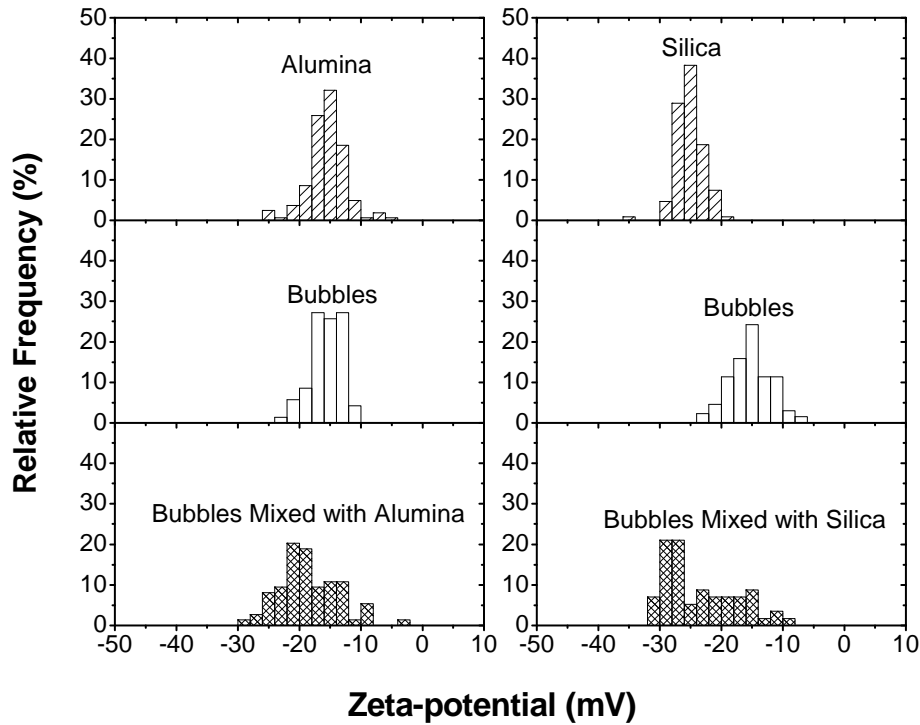
Figure 5-31: Zeta-potential distributions of submicron size bubbles and nano size alumina and silica particles in PFW at pH 8.5, measured individually or in a binary mixture.

Zeta-potential distribution results of submicron size bubbles and micron size particles in FPW of pH 8.5 are shown in Figure 5-32. When comparing with Figure 5-31, similarity is found between the two figures. Micron size alumina particles and bubbles in FPW both have negative zeta-potential distributions, and a gap of 8 mV is present in between the individual zeta-potential distribution peaks of the two components. The bimodal zeta-potential distribution of the binary mixture of bubble-micron size alumina particles have two zeta-potential distribution peaks at about -23 mV and -12 mV, representing independent micron size alumina particles and bubbles, suggesting no attachment among the two

159

components had occurred. The zeta-potential of micron size silica particles were also negative in FPW. The more negative zeta-potential value of silica, led to larger separation distance between the zeta-potential distribution peaks of micron size silica particles and bubbles. The zeta-potential distribution peaks of individually measured micron size silica particles and bubbles located correspondently at -31 mV and -17 mV, and the two associated zeta-potential distribution peaks of the bubble- micron size silica particle mixture were respectively at -29 mV and -15 mV. It is quite obvious that there is no attachment between bubbles and micron size silica particles. So in general, neither of the micron size particles attached to submicron size bubbles in FPW due to large electrostatic repulsion caused by uni-sign charges.

Despite the difference in size of the solid particles, results in this section suggest that changes at both the bubble and solid surfaces when measured in FPW largely affected bubble-particle interactions.
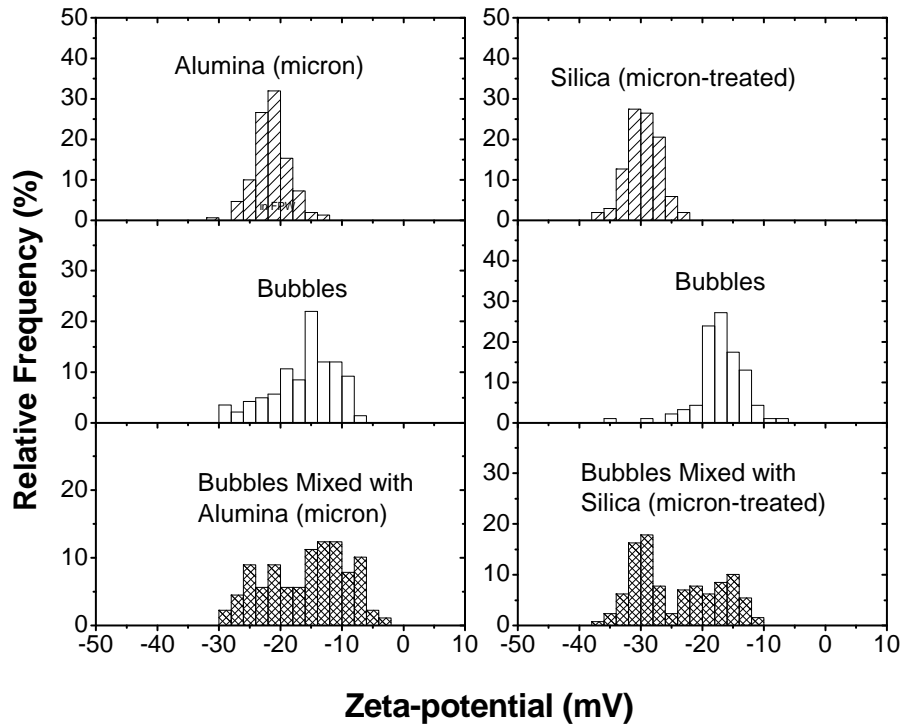
Figure 5-32: Zeta-potential distributions of submicron size bubbles and micron size alumina and hydrophobic silica particles in PFW at pH 8.5, measured individually or in a binary mixture.

5.3.3   Bubble-Particle Interactions in Tailings Water

As discussed earlier in the materials section, Posyn oil sands ore is an ore with high fines content, the zeta-potential of Posyn CF was measured to be -24 mV and that of Posyn FF and Posyn SF was -27 mV and -29 mV respectively. From Figure 5-33 and Figure 5-34, all three zeta-potential distributions of the three different kinds of Posyn fines have wide ranges and similar zeta-potential distribution peaks: -25 mV for CF, -27 mV for FF and -29 mV for SF. The zeta-potential distribution peak of bubbles in flotation

tailings water was around -20 mV. The zeta-potential distributions of the bubble-Posyn CF mixtures during *in situ* gas nucleation and mixing process (Figure 5-33) were alike, both extremely broad covering a range similar to that of independently measured Posyn CF. As a result, bubble-Posyn CF interactions could not be determined. The graphs in Figure 5-34 show that there might be some kind of attachment between bubbles and FF and SF particles. According to former researchers[23, 24, 26, 37, 52, 53], in presence of Ca^{2+} and Mg^{2+}, there should be attachment of solid particles with hydrophobic substances such as bitumen by using these cations as bridges, known as slime-coating. However, for reasons of broad fines distributions and overlapping of the distributions, bubble-fines interactions in tailings water were very difficult to define in current situation. There is the possibility of surfactants playing a role in modifying the surface properties of both bubbles and Posyn fines, but in order to precisely study bubble-particle interactions in industry-applied chemical conditions, further improvements of the technique or the system is desperately needed. It would be very helpful if the limitation of the technique (e.g. the minimum gap distance required) could be more precisely defined.
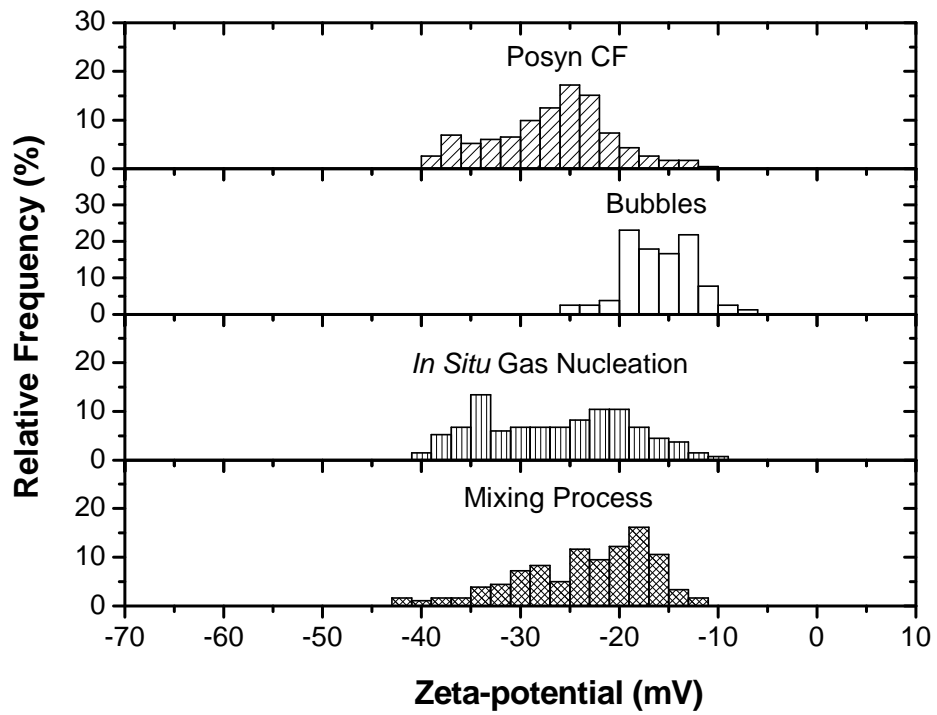
Figure 5-33: Zeta-potential distributions of submicron size bubbles and Posyn

centrifuged fines in flotation tailings water at pH 8.5, measured individually or in
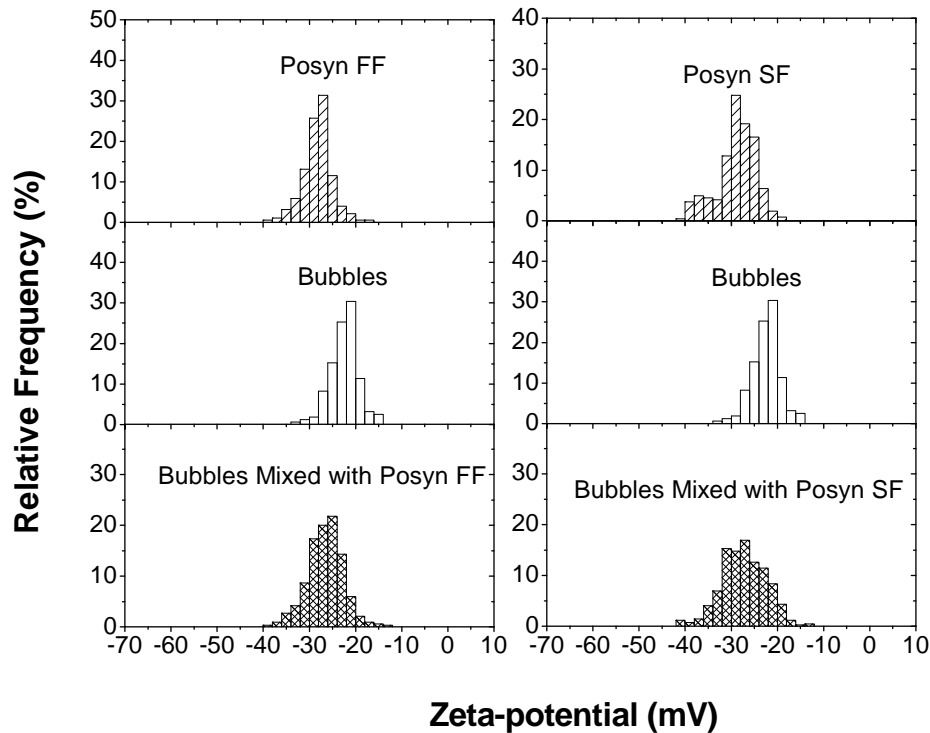
a binary mixture.

Figure 5-34: Zeta-potential distributions of submicron size bubbles, Posyn flotation fines and Posyn settled fines in flotation tailings water at pH 8.5, measured individually or in a binary mixture.

5.3.4   Summary

1) When compared to zeta-potential of submicron size bubbles, silica and alumina particles in 1 mM KCl solutions, zeta-potential of bubbles and silica in filtered process water was less negative while that of alumina became negative. Zeta-potential of all three components measured in FPW were very similar in values and decreased slightly with increasing pH.

2) Electrostatic double layer force dominates bubble-particle interactions in FPW. Negatively charged bubble attached to neither the negatively charged

164

alumina particles nor the negatively charged silica particles due electrostatic repulsive force.

3) Bubble-fines attachment in tailings water was not established by analysis of zeta-potential distributions due to the limitation of the technique.

Chapter 6 Conclusions

High intensity agitation is proven in this study to be efficient in generating submicron size bubbles through hydrodynamic cavitation. The submicron size bubble generation process was found to be greatly affected by agitation speed while the effect of agitation time and solution temperature on bubble generation needs to be further determined.

Submicron size bubbles generated by HIA have a diameter less than 1 μm and normally bare negative charge in simple electrolyte solutions, anionic surfactant solutions, frother solutions, FPW and tailings water. The zeta-potential of such bubbles could become positive in presence of cations, cationic surfactants and excessive H^+ (i.e. at low pH). It is also shown in this work that submicron size bubbles generated by HIA remain stable in size, number and surface charge for at least several hours in the case of 1 mM KCl solutions and up to several days in the case of surfactant solutions and FPW.

As shown previously, the zeta-potential distribution analysis technique is capable of providing excellent details of bubble-particle interactions. Electrostatic double layer force was found to play a dominant role in bubble-particle attachment in all cases of inorganic electrolyte solutions, surfactant/frother solutions and FPW. Strong electrostatic repulsive force resulted in a stable colloidal suspension of bubbles and particles while strong electrostatic attractive force resulted in bubble-particle attachment. Such effect of electrostatic double layer force was clearly differentiated in a ternary system where both electrostatic attractive force and electrostatic repulsive force were present. Negatively charged

bubbles were found to selectively attach to positively charged alumina, but not to negatively charged silica particles. Based on the strength of electrostatic double layer forces, bubbles and particles could be either strongly attached or weakly associated. Therefore armour-coating of fine particles on flotation bubbles is likely to occur when bubbles and fine particles bear surface charge of opposite signs. Improved fine particle flotation by enhanced bubble-particle attachment during *in situ* gas nucleation was confirmed even in presence of weak electrostatic repulsive force by bubble nucleation on particle surfaces that were slightly hydrophilic.

It was also found in this study that surfactants and frothers affect bubbles-particle attachment differently. Both surfactants and frothers have dramatic effect on zeta-potential of bubbles by its adsorption, but neither has significant impact on those of solid particles. Ionic surfactants SDS and DAH have better bubble generation capability than non-ionic frothers MIBC and DF250 even at lower concentrations. The addition of MIBC and DF250 leads to widely-spread and sometimes scattered zeta-potential distributions of submicron size bubbles. Adsorption of surfactant and frother molecules at bubble-water interface has highly likely changed the surface property of bubbles, as the effect of surfactant/frother type and concentration on bubble-particle attachment is evident. The mechanism of this effect remains to be further investigated.

For the case of industrial tailings water, due to limitation of the zeta-potential distribution analysis technique, bubble-fines interactions in such

167

complex chemical environments could not be well defined. Further improvements

in both the technique and interaction systems need to be made.

Chapter 7 Future Work

There are many aspects related to this work that could not yet be covered. Suggestions are made here, aiming to establish a more complete understanding of the fundamentals of bubble-particle interactions.

1) Correlate generation of submicron size bubbles with hydrodynamics and water chemistry, i.e. to relate the experimental data with theoretical simulations.

2) Study the effect of gas content and temperature on the generation of submicron size bubbles to monitor and control the bubble generation process and to achieve a more stable system.

3) Further study the interactions of submicron size bubbles with hydrophobic particles in simple electrolyte solutions or simple surfactant/frother solutions, studying the effect of hydrophobic force on bubble-particle interactions in a real industrial system.

4) Further study the interactions of submicron size bubbles with different clay particles and fines isolated from oil sands processing tailings in both the industrial process water and simulated process water to find the role of different electrolytes and surfactants on bubble-solid interactions or bubble armour-coating.

5) Discover a procedure in measuring the contact angle of powdered materials and thus precisely apply the extended DLVO theory in calculating interaction forces as the calculation in this study is largely based on reported data of

previous studies. There is a chance of large discrepancy between the experimental results and theoretically estimated results.

6) Study the effect of surfactant and frother type and concentration on bubble-solid interactions, identify the structure of surfactants at the interface of different phases and thus include the steric force in calculating interaction energies.

7) Study the effect of surface roughness on in situ gas nucleation (i.e. gas envelope/pocket formation on the surface of solid particles during hydrodynamic cavitation.), as surface roughness, compared to surface hydrophobicity, has been proposed to play a more predominant role in gas nuclation[51, 60].

8) Better define the zeta-potential distribution analysis technique to improve its application limits.

9) Study bubble-particle interactions with AFM, correlated the results with both the results of zeta-potential distribution measurement and energy profile calculated using extended DLVO theory, and hence assure the accuracy and reliability of established bubble-particle interaction mechanisms.

References

(1) Chalaturnyk, R. J.; Scott, J. D.; Ozum, B. *Pet. Sci. Technol.* **2002**, *20*, 1025-1046.

(2) Walsh, C. Canada's Oil Reserves 2nd Only To Saudi Arabia. http://webcache.googleusercontent.com/search?q=cache:OGy_Gow3hdMJ:www.rense.com/general37/petrol.htm+oil+sand+reserve+walsh&cd=1&hl=en&ct=clnk&gl=ca.

(3) Lerner, I. Black gold in the cold sand. http://www.icis.com/Articles/2010/01/11/9323018/canadas-oil-sands-look-set-to-bounce-back.html.

(4) http://www.nationmaster.com/graph/ene_oil_pro-energy-oil-production.

(5) Masliyah, J.; Zhou, Z.; Xu, Z.; Czarnecki, J.; Hamza, H. *Can. J. Chem. Eng.* **2004**, *82*, 628-654.

(6) Eddy Isaacs. Canadian Oil Sands: Development and Future Outlook, National Academies Workshop on Trends in Oil Supply/Demand and Peaking Coventional Oil Production, **2005**.

(7) Camp, F. W. *Processing Athabasca Tar sands - tailings disposal.* Section Title: Fossil Fuels, Derivatives, and Related Products; **1976**, pp C, 47.

(8) Camp, F. W. **1977**, Improving recovery in the hot water extraction process. Patent Application Country: Application: CA; Patent Country: CA Patent Great Canadian Oil Sands Ltd., Can. 1013695.

(9) Hendrickson, T. A. In *Synthetic fuels data handbook;* Cameron Engineers: Denver, **1975**, pp 308.

(10) Clark, K. A.; Pasternack, D. S. *J. Ind. Eng. Chem. (Washington, D. C.)* **1932**, *24*, 1410-1416.

(11) Ball, M. W. *Am. Assoc. Pet. Geol. Bull.* **1935**, *19*, 153-171.

(12) Clark, K. A. *Trans. - Can. Inst. Min. Metall. Min. Soc. N. S.* **1944**, *47*, 257-274.

(13) Takamura, K. *Can. J. Chem. Eng.* **1982**, *60*, 538-545.

(14) Hall, A. C.; Collins, S. H.; Melrose, J. C. *SPEJ, Soc. Pet. Eng. J.* **1983**, *23*, 249-258.

(15) Fitzgerald, J. J. In *Black Gold with Grit : The Alberta Oil Sands;* Gray's Publishing: Sidney, **1978**, pp 264.

(16) Masliyah, J. H.; Gray, M. R. In *Oil Sands Extraction and Upgrading-Intensive Short Course;* **2008**.

(17) Liu, J.; Xu, Z.; Masliyah, J. *Energy Fuels* **2005**, *19*, 2056-2063.

(18) Smith, P. W. **1994**, Extractor and process for extracting one material (oil) from a multiphase feed material (oil sand). Patent Application Country: Application: CA; Patent Country: CA Patent Can. 2098656.

(19) Sury, K. N. **1990**, Low temperature bitumen recovery process, United States Patent Esso Resources Canada Limited (Calgary, CA). 4,946,597.

(20) Gu, G.; Xu, Z.; Nandakumar, K.; Masliyah, J. *Int. J. Miner. Process.* **2003**, *69*, 235-250.

(21) Gu, G.; Sanders, R. S.; Nandakumar, K.; Xu, Z.; Masliyah, J. H. *Int. J. Miner. Process.* **2004**, *74*, 15-29.

(22) Wang, W.; Zhou, Z.; Nandakumar, K.; Masliyah, J. H.; Xu, Z. *Int. J. Miner. Process.* **2005**, *75*, 69-82.

(23) Liu, J.; Xu, Z.; Masliyah, J. *AIChE J.* **2004**, *50*, 1917-1927.

(24) Liu, J.; Xu, Z.; Masliyah, J. *Can. J. Chem. Eng.* **2004**, *82*, 655-666.

(25) Liu, J. Role of colloidal interactions in bitumen recovery from oil sands, University of Alberta (Canada), Canada, **2004**.

(26) Liu, J.; Zhou, Z.; Xu, Z.; Masliyah, J. *J. Colloid Interface Sci.* **2002**, *252*, 409-418.

(27) Liu, J.; Zhou, Z.; Xu, Z. *Industrial and Engineering Chemistry Research* **2002**, *41*, 52-57.

(28) Long, J.; Xu, Z.; Masliyah, J. H. *Energy Fuels* **2005**, *19*, 1440-1446.

(29) Repka, C. Bitumen-montmorillonite interactions in aqueous media, University of Alberta (Canada), Canada, **2007**.

(30) Yount, D. E. *J. Colloid Interface Sci.* **1997**, *193*, 50-59.

(31) Cho, S.; Kim, J.; Chun, J.; Kim, J. *Colloids Surf. Physicochem. Eng. Aspects* **2005**, *269*, 28-34.

(32) Najafi, A. S.; Drelich, J.; Yeung, A.; Xu, Z.; Masliyah, J. *J. Colloid Interface Sci.* **2007**, *308*, 344-350.

(33) Cameron, R. *ACCJ Journal* **2005**, 36-37.

(34) Zimmerman, W. B. J.; Tesar, V. **2008**, Bubble generation for aeration and other purposes. Patent Application Country: Application: GB; Patent Country: GB Patent The University of Sheffield, UK. 2443396.

(35) Moran, K.; Yeung, A.; Masliyah, J. *Can. J. Chem. Eng.* **2000**, *78*, 625-634.

(36) Flynn, M.; Bara, B.; Czarnecki, J.; Masliyah, J. *Can. J. Chem. Eng.* **2001**, *79*, 468-470.

(37) Liu, J.; Xu, Z.; Masliyah, J. *J. Colloid Interface Sci.* **2005**, *287*, 507-520.

(38) Arnold, B. J.; Aplan, F. F. *Int. J. Miner. Process.* **1986**, *17*, 225-242.

(39) Attia, Y. A.; Deason, D. M. *Colloids and Surfaces* **1989**, *39*, 227-238.

(40) Okada, K.; Akagi, Y.; Kogure, M.; Yoshioka, N. *Can. J. Chem. Eng.* **1990**, *68*, 393-399.

(41) Okada, K.; Akagi, Y.; Kogure, M.; Yoshioka, N. *Can. J. Chem. Eng.* **1990**, *68*, 614-621.

(42) Zhou, Z. A.; Xu, Z.; Finch, J. A. *J. Colloid Interface Sci.* **1996**, *179*, 311-311.

(43) Krasowska, M.; Zawala, J.; Malysa, K. *Adv. Colloid Interface Sci.* **2009**, *147-148*, 155-169.

(44) Mulleneers, H. A. E.; Koopal, L. K.; Bruning, H.; Rulkens, W. H. *Sep. Sci. Technol.* **2002**, *37*, 2097-2112.

(45) Yoon, R.; Mao, L. *J. Colloid Interface Sci.* **1996**, *181*, 613-626.

(46) Yoon, R.; Flinn, D. H.; Rabinovich, Y. I. *J. Colloid Interface Sci.* **1997**, *185*, 363-370.

(47) Yoon, R.; Aksoy, B. S. *J. Colloid Interface Sci.* **1999**, *211*, 1-10.

(48) Nguyen, A. V.; Nalaskowski, J.; Miller, J. D.; Butt, H. *Int. J. Miner. Process.* **2003**, *72*, 215-225.

(49) Liu, J.; Xu, Z.; Masliyah, J. *J. Colloid Interface Sci.* **2005**, *287*, 507-520.

(50) Bower, M. J. D.; Bank, T. L.; Giese, R. F.; van Oss, C. J. *Colloids Surf. Physicochem. Eng. Aspects* **2010**, *362*, 90-96.

(51) Zhou, Z. A.; Xu, Z.; Finch, J. A. *Industrial and Engineering Chemistry Research* **1998**, *37*, 1998-2004.

(52) Ding, X.; Repka, C.; Xu, Z.; Masliyah, J. *Can. J. Chem. Eng.* **2006**, *84*, 643-650.

(53) Zhao, H.; Long, J.; Masliyah, J. H.; Xu, Z. *Ind. Eng. Chem. Res.* **2006**, *45*, 7482-7490.

(54) Hardy, R. M.; Hemstock, R. A. In *Shearing strength characteristics of Athabasca oil sands;* Research Council of Alberta Information Series No.45; **1963**, Vol. K.A. Clark, pp 109-122.

(55) Bichard, J. A. In *Oil sands composition and behaviour research: the research papers of John A. Bichard, 1957-1965;* Edmonton, Alta., Canada : Alberta Oil Sands Technology and Research Authority: **1987**.

(56) Jowett, A. *Formation and disruption of particle-bubble aggregates in flotation.* Section Title: Extractive Metallurgy; **1980**, Vol. 1 pp 720-754.

(57) Yoon, R. -.; Yordan, J. L. *J. Colloid Interface Sci.* **1991**, *146*, 565-572.

(58) Zhou, Z. A.; Xu, Z.; Finch, J. A.; Hu, H.; Rao, S. R. *Int. J. Miner. Process.* **1997**, *51*, 139-149.

(59) Zhou, Z. A.; Xu, Z.; Finch, J. A.; Masliyah, J. H.; Chow, R. S. *Minerals Eng* **2009**, *22*, 419-433.

(60) Hampton, M. A.; Nguyen, A. V. *Adv. Colloid Interface Sci.* **2010**, *154*, 30-55.

(61) Kasongo, T.; Zhou, Z.; Xu, Z.; Masliyah, J. *Can. J. Chem. Eng.* **2000**, *78*, 674-681.

(62) Masliyah, J.; Xu, Z.; Czarnecki, J. *Role of electrokinetics and interfacial phenomena in bitumen recovery from oil sands.* **2003**, pp COLL-505.

(63) Ng, S.; Warszynski, P.; Zembala, M.; Malysa, K. *Minerals Eng* **2000**, *13*, 1519-1532.

(64) Zhou, Z.; Xu, Z.; Masliyah, J. *Can. J. Chem. Eng.* **2000**, *78*, 617-624.

174

(65) Skvarla, J.; Kmet, S. *Colloids Surf. Physicochem. Eng. Aspects* **1993**, *79*, 89-89.

(66) Ralston, J.; Fornasiero, D.; Hayes, R. *Int. J. Miner. Process.* **1999**, *56*, 133-164.

(67) Mishchuk, N. A.; Koopal, L. K.; Dukhin, S. S. *J. Colloid Interface Sci.* **2001**, *237*, 208-223.

(68) Bournival, G.; Ata, S. *Minerals Eng* **2010**, *23*, 111-116.

(69) Miettinen, T.; Ralston, J.; Fornasiero, D. *Minerals Eng* **2010**, *23*, 420-437.

(70) Xu, Z.; Choung, J.; Sun, W.; Cui, Z. *Visualization of Fine Bubbles and Their Role in Fine Pariticle Flotation*, Ottawa, **2006**.

(71) Tao, D.; Yu, S.; Zhou, X.; Honaker, R. Q.; Parekh, B. K. *Int. J. Coal Prep. Util.* **2008**, *28*, 1-14.

(72) Read, A. D.; Kitchener, J. A. *J. Colloid Interface Sci.* **1969**, *30*, 391-398.

(73) Yang, C.; Dabros, T.; Li, D.; Czarnecki, J.; Masliyah, J. H. *A visualizing method for study of micron bubble attachment onto a solid surface under varying physicochemical conditions,* American Chemical Society: **2000**, Vol. 39 pp 4949-4955.

(74) King, R. P. In *Priciples of Flotation;* South African Institute of Mining and Metallurgy: Cape Town, **1982**, pp 268.

(75) Li, C.; Somasundaran, P. *J. Colloid Interface Sci.* **1991**, *146*, 215-218.

(76) Shaw, D. J. In *Introduction to Colloid and Surface Chemistry;* Butterworth-Heinemann: Oxford, **1992**, pp 320.

(77) Nguyen, A. V.; Schultze, H. J. In *Colloidal science of flotation;* Surfactant science series; Marcel Dekker, Inc.: New York, **2004**, Vol. 118, pp 850.

(78) Han, M. Y.; Ahn, H. J.; Shin, M. S.; Kim, S. R. *Water Science and Technology* **2004**, *50*, 49-56.

(79) Okada, K.; Akagi, Y. *J. Chem. Eng. Japan* **1987**, *20*, 11-15.

(80) Chernoberezhskii, Y. M.; Golikova, E. V.; Malkes, E. V.; Kuchuk, V. I.; Shaiovich, Y. L. *Relation of the zeta-potential of particles of crystalline and amorphous modifications of silicon dioxide to the time of their presence in solution.* Section Title: Surface Chemistry and Colloids; **1983**, pp 117-125.

(81) Kuo, J. F.; Yen, T. F. *Proc. Intersoc. Energy Convers. Eng. Conf.* **1986**, *21st*, 251-256.

(82) Kubota, K.; Jameson, G. J. *J. Chem. Eng. Jpn.* **1993**, *26*, 7-12.

(83) Kosmulski, M. *J. Colloid Interface Sci.* **1998**, *208*, 543-545.

(84) Lindberg, R.; Sundholm, G.; Sjoblom, J.; Ahonen, P.; Kauppinen, E. I. *J. Dispersion Sci. Technol.* **1999**, *20*, 715-722.

(85) Elmahdy, A. M.; Mirnezami, M.; Finch, J. A. *Int. J. Miner. Process.* **2008**, *89*, 40-43.

(86) Preuss, M.; Butt, H. *Langmuir* **1998**, *14*, 3164-3174.

(87) Ishida, N.; Yotsumoto, H. *AIST* **2004**, *120*, 400-405.

(88) Ishida, N.; Yotsumoto, H. *AIST* **2004**, *120*, 395-399.

(89) Ishida, N. *Colloids Surf. Physicochem. Eng. Aspects* **2007**, *300*, 293-299.

(90) Englert, A. H.; Krasowska, M.; Fornasiero, D.; Ralston, J.; Rubio, J. *Int. J. Miner. Process.* **2009**, *92*, 121-127.

(91) Saulnier, P.; Lachaise, J.; Morel, G.; Graciaa, A. *J. Colloid Interface Sci.* **1996**, *182*, 395-399.

(92) Creux, P.; Lachaise, J.; Graciaa, A.; Beattie, J. K. *Journal of Physical Chemistry C* **2007**, *111*, 3753-5.

(93) Plotnichenko, V. G.; Sokolov, V. O.; Dianov, E. M. *Inorg. Mater.* **2000**, *36*, 404-410.

(94) Fan, X.; Zhang, Z.; Li, G.; Rowson, N. A. *Chemical Engineering Science* **2004**, *59*, 2639-2645.

(95) Wan, J.; Tokunaga, T. K. **2002**, *247*, 54-61.

(96) Klassen, V. I.; Mokrousov, V. A. In *An Introduction to the Theory of Flotation;* Butterworth: London, **1963**, pp 493.

(97) Prakash, A.; Margaritis, A.; Li, H.; Bergougnou, M. A. *Biochem. Eng. J.* **2001**, *9*, 155-163.

(98) Divinis, N.; Karapantsios, T. D.; Kostoglou, M.; Panoutsos, C. S.; Bontozoglou, V.; Michels, A. C.; Sneep, M. C.; De Bruijn, R.; Lotz, H. *AICHE J.* **2004**, *50*, 2369-2382.

(99) Zimmerman, W. B.; Tesar, V.; Butler, S.; Bandulasena, H. H. **2008**, *2*, 1-8.

(100) Jeong, J.; Wu, C.; Murthy, H. N.; Hahn, E.; Paek, K. *Biotechnol. Bioprocess Eng.* **2009**, *14*, 91-98.

(101) Zhang, Y.; Chen, T.; Liu, S. *Shengwu Yixue Gongchengxue Zazhi* **2009**, *26*, 1129-1132.

(102) Woo, G. J.; Kim, Y. G.; Kwak, G. W.; Kim, M. G. **2010**, Advanced water treatment method with sintered multifunctional fine bubble generator for aeration as well as filtration. Patent Application Country: Application: KR; Patent Country: KR Patent Daewoong ENS Co., Ltd., S. Korea. 2010102567.

(103) Nguyen, A. V.; George, P.; Jameson, G. J. *Chemical Engineering Science* **2006**, *61*, 2494-2509.

(104) Matsumoto, Y.; Aoki, M. *Nippon Kikai Gakkai Ronbunshu, B-hen* **1983**, *49*, 2265-2272.

(105) S. Gowing. Dissolving of Bubbles in Liquids, **1987**.

(106) Ata, S.; Jameson, G. J. *Int. J. Miner. Process.* **2005**, *76*, 123-139.

(107) Martin, M.; Montes, F. J.; Galan, M. A. *Industrial and Engineering Chemistry Research* **2008**, *47*, 6251-6263.

(108) Martin, M.; Montes, F. J.; Galan, M. A. *Chemical Engineering Science* **2008**, *63*, 3223-3234.

(109) Washio, S.; Takahashi, S.; Murakami, K.; Tada, T.; Deguchi, S. *Nihon Kikai Gakkai Ronbunshu, B Hen/Transactions of the Japan Society of Mechanical Engineers, Part B* **2008**, *74*, 1376-1385.

(110) TAMURA, Y.; MATSUMOTO, Y. *Journal of Hydrodynamics, Ser.B* **2009**, *21*, 41-46.

(111) Levich, V. G. In *Physicochemical Hydrodynamics;* Prentice-Hall international series in the physical and chemical engineering sciences; Prentice-Hall: Englewood Cliffs, N.J, **1962**, pp 700.

(112) Brennen, C. E. In *Cavitaion and bubble dynamics;* Oxford University Press: New York, **1995**, pp 294.

(113) MØRCH, K. A. *Journal of Hydrodynamics, Ser.B* **2009**, *21*, 176-189.

(114) Attard, P.; Moody, M. P.; Tyrrell, J. W. G. *Physica A: Statistical Mechanics and its Applications* **2002**, *314*, 696-705.

(115) Aogaki, R.; Miura, M.; Oshikiri, Y. *Origin of nanobubble - Formation of stable vacancy in electrolyte solution,* Nanotechnology - General - 214th ECS Meeting/PRiME 2008, October 12, 2008 - October 17; Electrochemical Society Inc: Honolulu, HI, United states, **2009**, Vol. 16 pp 181-189.

(116) Lubetkin, S. D. *Langmuir* **2003**, *19*, 2575-2587.

(117) Ushikubo, F. Y.; Furukawa, T.; Nakagawa, R.; Enari, M.; Makino, Y.; Kawagoe, Y.; Shiina, T.; Oshita, S. *Colloids Surf. Physicochem. Eng. Aspects* **2010**, *361*, 31-37.

(118) Millero, F. J. In *The Physical Chemistry of Natural Waters;* Wiley-Interscience: New York, **2001**, pp 654.

(119) Ljunggren, S.; Eriksson, J. C. *Colloids Surf. Physicochem. Eng. Aspects* **1997**, *129-130*, 151-155.

(120) Jones, S. F.; Evans, G. M.; Galvin, K. P. *Adv. Colloid Interface Sci.* **1999**, *80*, 27-50.

(121) Kikuchi, K.; Nagata, S.; Tanaka, Y.; Saihara, Y.; Ogumi, Z. *J Electroanal Chem* **2007**, *600*, 303-310.

(122) Jin, F. Studies on nanobubbles in aqueous solutions, The Chinese University of Hong Kong (Hong Kong), Hong Kong, **2007**.

(123) Moody, M. P.; Attard, P. *J. Chem. Phys.* **2001**, *115*, 8967-8977.

(124) Oxtoby, D. W.; Evans, R. *J. Chem. Phys.* **1988**, *89*, 7521-7530.

(125) Evans, D. R.; Craig, V. S. J.; Senden, T. J. *Physica A: Statistical Mechanics and its Applications* **2004**, *339*, 101-105.

(126) Meagher, L.; Craig, V. S. J. *Langmuir* **1994**, *10*, 2736-2742.

(127) Wood, J.; Sharma, R. **1995**, *11*, 4797-4802.

(128) Ishida, N.; Higashitani, K. *Minerals Eng* **2006**, *19*, 719-725.

(129) Ishida, N.; Inoue, T.; Miyahara, M.; Higashitani, K. *Langmuir* **2000**, *16*, 6377-6380.

(130) FAN, M.; TAO, D.; HONAKER, R.; LUO, Z. *Mining Science and Technology (China)* **2010**, *20*, 1-19.

(131) Kikuchi, K.; Tanaka, Y.; Saihara, Y.; Maeda, M.; Kawamura, M.; Ogumi, Z. *J. Colloid Interface Sci.* **2006**, *298*, 914-919.

(132) Hemmingsen, E. A. *J. Appl. Phys.* **1975**, *46*, 213-218.

(133) Finkelstein, Y.; Tamir, A. *AICHE J.* **1985**, *31*, 1409-19.

(134) Tuziuti, T.; Yasui, K.; Sivakumar, M.; Iida, Y. *Ultrasonics* **2006**, *44*, e357-e361.

(135) Gupta, A. K.; Banerjee, P. K.; Mishra, A. *Coal Prep. (Philadelphia, PA, U. S.)* **2007**, *27*, 107-125.

(136) Azgomi, F.; Gomez, C. O.; Finch, J. A. *Int. J. Miner. Process.* **2007**, *83*, 1-11.

(137) Yang, S.; Dammer, S. M.; Bremond, N.; Zandvliet, H. J. W.; Kooij, E. S.; Lohse, D. *Langmuir* **2007**, *23*, 7072-7077.

(138) Bunkin, N. F.; Suyazov, N. V.; Shkirin, A. V.; Ignat'Ev, P. S.; Indukaev, K. V. *Journal of Experimental and Theoretical Physics* **2009**, *108*, 800-816.

(139) Eddington, R. I.; Kenning, D. B. R. *Int. J. Heat Mass Transfer* **1979**, *22*, 1231-1236.

(140) Borkent, B. M.; Dammer, S. M.; Schonherr, H.; Vancso, G. J.; Lohse, D. *Phys. Rev. Lett.* **2007**, *98*, 204502/1-204502/4.

(141) Gerth, W. A.; Hemmingsen, E. A. *J. Colloid Interface Sci.* **1980**, *74*, 80-89.

(142) FAN, M.; TAO, D.; HONAKER, R.; LUO, Z. *Mining Science and Technology (China)* **2010**, *20*, 159-177.

(143) Chodankar, S.; Aswal, V. K.; Hassan, P. A.; Wagh, A. G. *Physica B: Condensed Matter* **2007**, *398*, 112-117.

(144) Kim, J.; Song, M.; Kim, J. *J. Colloid Interface Sci.* **2000**, *223*, 285-291.

(145) Yoon, R.; Yordan, J. L. *J. Colloid Interface Sci.* **1986**, *113*, 430-438.

(146) Conway, B. E. **1975**, *65*, 491-504.

(147) Paluch, M. *Adv. Colloid Interface Sci.* **2000**, *84*, 27-45.

(148) Harvey, E. N.; Whiteley, A. H.; McElroy, W. D.; Pease, D. C.; Barnes, D. K. **1944**, *24*, 23-24.

(149) Fox, F. E.; Herzfeld, K. F. *J. Acoust. Soc. Am.* **1954**, *26*, 984-989.

(150) Ducker, W. A. *Langmuir* **2009**, *25*, 8907-8910.

(151) Simonsen, A. C.; Hansen, P. L.; Klösgen, B. *J. Colloid Interface Sci.* **2004**, *273*, 291-299.

(152) Krzan, M.; Malysa, K. *Physicochem. Probl. Miner. Process.* **2002**, *36*, 65-76.

(153) Malysa, K.; Krasowska, M.; Krzan, M. *Adv. Colloid Interface Sci.* **2005**, *114-115*, 205-225.

(154) Finch, J. A.; Nesset, J. E.; Acuña, C. *Minerals Eng* **2008**, *21*, 949-957.

(155) Cho, Y. S.; Laskowski, J. S. *Int. J. Miner. Process.* **2002**, *64*, 69-80.

(156) Grau, R. A.; Laskowski, J. S.; Heiskanen, K. *Int. J. Miner. Process.* **2005**, *76*, 225-233.

(157) Finch, J. A.; Gelinas, S.; Moyo, P. *Minerals Eng* **2006**, *19*, 726-733.

(158) Aldrich, C.; Feng, D. *Minerals Eng* **2000**, *13*, 1049-1057.

(159) Grau, R. A.; Laskowski, J. S. *Can. J. Chem. Eng.* **2006**, *84*, 170-182.

(160) Laskowski, J. S.; Tlhone, T.; Williams, P.; Ding, K. *Int. J. Miner. Process.* **2003**, *72*, 289-299.

(161) Saulnier, P.; Bouriat, P.; Morel, G.; Lachaise, J.; Graciaa, A. *J. Colloid Interface Sci.* **1998**, *200*, 81-85.

(162) Gélinas, S.; Finch, J. A.; Gouet-Kaplan, M. *J. Colloid Interface Sci.* **2005**, *291*, 187-191.

(163) Karraker, K. A.; Radke, C. J. *Adv. Colloid Interface Sci.* **2002**, *96*, 231-264.

(164) Levine, I. N. In *Physical Chemistry;* McGraw-Hill College: Boston, **2001**.

(165) Masliyah, J. H.; Bhattacharjee, S. In *Electrokinetic and Colloid Transport Phenomena;* Wiley-Interscience: Hoboken, **2006**, pp 736.

(166) McNaught, A. D.; Wilkinson, A. In *Compendium of Chemical Terminology, (the "Gold Book")*. Blackwell Scientific Publications: Oxford, **1997**.

(167) Hunter, R. J. In *Introduction to Modern Colloid;* Oxford University Press: New York, **1994**, pp 338.

(168) Grabbe, A.; Horn, R. G. *J. Colloid Interface Sci.* **1993**, *157*, 375-383.

(169) Kar, G.; Chander, S.; Mika, T. S. *J. Colloid Interface Sci.* **1973**, *44*, 347-355.

(170) Xu, Z.; Yoon, R. *J. Colloid Interface Sci.* **1989**, *132*, 532-541.

(171) Xu, Z.; Yoon, R. *J. Colloid Interface Sci.* **1990**, *134*, 427-434.

(172) Yotsumoto, H.; Yoon, R. *J. Colloid Interface Sci.* **1993**, *157*, 434-441.

(173) Yotsumoto, H.; Yoon, R. *J. Colloid Interface Sci.* **1993**, *157*, 426-433.

(174) Pashley, R. M. *J. Colloid Interface Sci.* **1981**, *80*, 153-162.

(175) Pashley, R. M. *J. Colloid Interface Sci.* **1981**, *83*, 531-546.

(176) Meagher, L. *J. Colloid Interface Sci.* **1992**, *152*, 293-295.

(177) Ducker, W. A.; Senden, T. J.; Pashley, R. M. *Nature* **1991**, *353*, 239-241.

(178) Ducker, W. A.; Xu, Z.; Clarke, D. R.; Israelachvili, J. N. *J. Am. Ceram. Soc.* **1994**, *77*, 437-443.

(179) Nishimura, S.; Kodama, M.; Noma, H.; Inoue, K.; Tateyama, H. *Colloids Surf. Physicochem. Eng. Aspects* **1998**, *143*, 1-16.

(180) Teschke, O.; De Souza, E. F. *Langmuir* **2003**, *19*, 5357-5365.

(181) Israelachvili, J.; Pashley, R. *Nature* **1982**, *300*, 341-342.

(182) Pashley, R. M.; McGuiggan, P. M.; Ninham, B. W.; Evans, D. F. *Science (Washington, D. C. , 1883-)* **1985**, *229*, 1088-1089.

(183) Claesson, P. M.; Blom, C. E.; Herder, P. C.; Ninham, B. W. *J. Colloid Interface Sci.* **1986**, *114*, 234-242.

(184) Rabinovich, Y. I.; Yoon, R. -. *Colloids Surf. Physicochem. Eng. Aspects* **1994**, *93*, 263-273.

(185) Craig, V. S. J.; Ninham, B. W.; Pashley, R. M. *Langmuir* **1999**, *15*, 1562-1569.

(186) Hunter, R. J. In *Foundations of colloid science;* Oxford University Press: Oxford ; New York, **2001**, pp 806.

(187) Gulicovski, J. J.; Cerovic, L. S.; Milonjic, S. K. *Mater. Manuf. Processes* **2008**, *23*, 615-619.

(188) Hackley, V. A.; Patton, J.; Lum, L. H.; Wasche, R. J.; Naito, M.; Abe, H.; Hotta, Y.; Pendse, H. *J. Dispersion Sci. Technol.* **2002**, *23*, 601-617.

(189) Kotlyar, L. S.; Sparks, B. D.; LePage, Y.; Woods, J. R. *Clay Miner.* **1998**, *33*, 103-107.

(190) Xu, Y.; Cymerman, G. *Flocculation of fine oil sand tails.* Section Title: Waste Treatment and Disposal; **1999**, pp 591-604.

(191) Kaminsky, H.; Etsell, T.; Ivey, D. G.; Omotoso, O. *Clay Sci.* **2006**, *12*, 217-222.

(192) Adeyinka, O. B.; Samiei, S.; Xu, Z.; Masliyah, J. H. *Can. J. Chem. Eng.* **2009**, *87*, 422-434.

(193) Zhou, Z. A.; Xu, Z.; Finch, J. A. *Fundamental study of cavitation in flotation.* Section Title: Extractive Metallurgy; **1995**, Vol. 3 pp 93-97.

(194) Anonymous Zeta Potential An Introduction in 30 Minutes, Zetasizer Nano series technical note, .

(195) Singh, B. P.; Menchavez, R.; Takai, C.; Fuji, M.; Takahashi, M. *J. Colloid Interface Sci.* **2005**, *291*, 181-186.

(196) Ribeiro, J.,Cláudio P.; Mewes, D. *Chemical Engineering Science* **2006**, *61*, 5704-5716.

(197) Yang, C.; Dabros, T.; Li, D.; Czarnecki, J.; Masliyah, J. H. *J. Colloid Interface Sci.* **2001**, *243*, 128-135.

(198) McShea, J. A.; Callaghan, I. C. *Colloid Polym. Sci.* **1983**, *261*, 757-766.

(199) Neppiras, E. A.; Noltingk, B. E. *Proc. Phys. Soc. , London* **1951**, *64B*, 1032-1038.

(200) Mishchuk, N.; Ralston, J.; Fornasiero, D. *J. Colloid Interface Sci.* **2006**, *301*, 168-175.

(201) Tan, S. Y.; Whitby, C. P.; Ralston, J.; Fornasiero, D. *Advanced Powder Technology* **2009**, *20*, 262-266.

(202) Esumi, K.; Asano, Y.; Sakamoto, Y.; Meguro, K. *Bull. Chem. Soc. Jpn.* **1989**, *62*, 1037-1041.

(203) Vanjara, A. K.; Dixit, S. G. *Langmuir* **1995**, *11*, 2504-2507.

(204) Esumi, K.; Iitaka, M.; Torigoe, K. *J. Colloid Interface Sci.* **2000**, *232*, 71-75.

(205) Xu, Z.; Ducker W.; Israelachvili J. *Langmuir* **1996**, *12*, 2263-2270.

(206) Williams, E. J.; Smolen, V. F. *J Pharm Sci* **1972**, *61*, 639-641.

(207) Cases, J.; Mielczarski, J.; Mielczarska, E.; Michot, L. J.; Villieras, F.; Thomas, F. *C. R. Geosci.* **2002**, *334*, 675-688.

(208) Somasundaran, P. In *Encyclopedia of surface and colloid science;* Somasundaran, P., Hubbard, A., Eds.; Taylor & Francis: London, **2006**, pp 8032.

(209) Laskowski, J. S. *Physicochem. Probl. Miner. Process.* **2004**, *38*, 13-22.

(210) Chibowski, E.; Delgado, A. V.; Rudzka, K.; Szcześ, A.; Hołysz, L. *J. Colloid Interface Sci.* **2011**, *353*, 281-289.

(211) Bruil, H. G.; Van Aartsen, J. J. *Colloid Polym. Sci.* **1974**, *252*, 32-38.

(212) Bunkin, N. F.; Indukaev, K. V.; Ignat'ev, P. S. *Journal of Experimental & Theoretical Physics* **2007**, *104*, 486-498.

(213) Bunkin, N. F.; Suyazov, N. V.; Shkirin, A. V.; Ignat'ev, P. S.; Indukaev, K. V. *Physics of Wave Phenomena* **2008**, *16*, 243-260.

(214) Ohgaki, K.; Khanh, N. Q.; Joden, Y.; Tsuji, A.; Nakagawa, T. *Chemical Engineering Science* **2010**, *65*, 1296-1300.

(215) Atkinson, R.J. *J.Colloid Interface Sci.* **1973**, *42*, *3*, 624-628.

Appendix I: Bubble-Carbon Black Interactions in 0.1 mM DF250 + 1 mM KCl Solutions as a Function of pH

It was our original aim to establish effect of hydrophobic force on bubble-particle interactions by investigation of interaction of submicron size bubbles with highly hydrophobic carbon black particles in 0.1 mM DF250 + 1 mM KCl solutions as a function of pH. However, due to limitations of the investigation technique, this goal was not successfully achieved in this work.
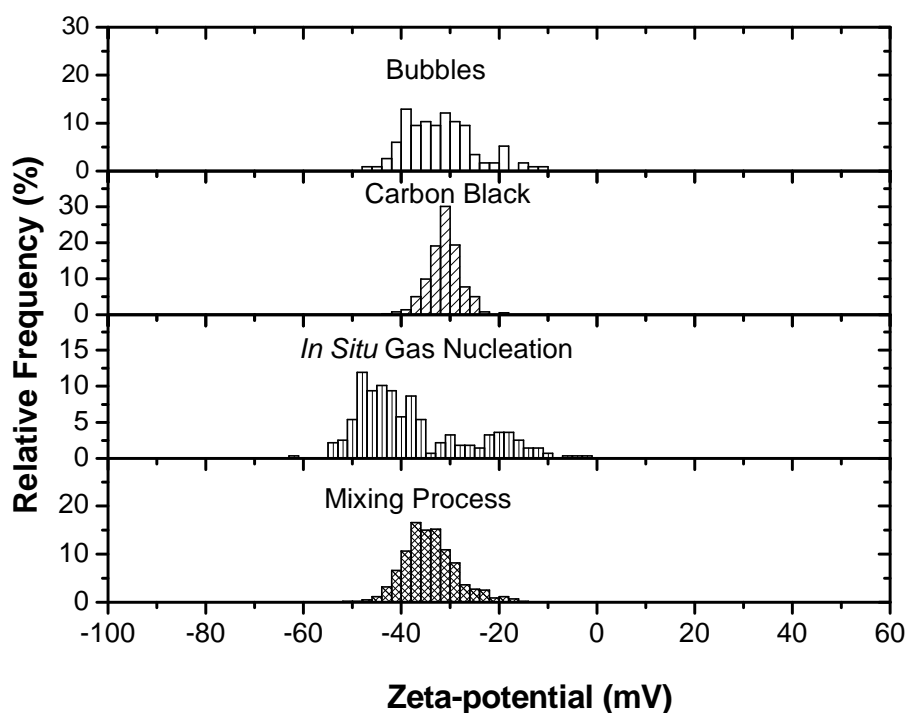

Figure AI- 1: Zeta-potential distributions of submicron size bubbles and carbon black particles in 0.1 mM DF250 + 1 mM KCl solutions at pH 6.5, measured individually or in a binary mixture.

184
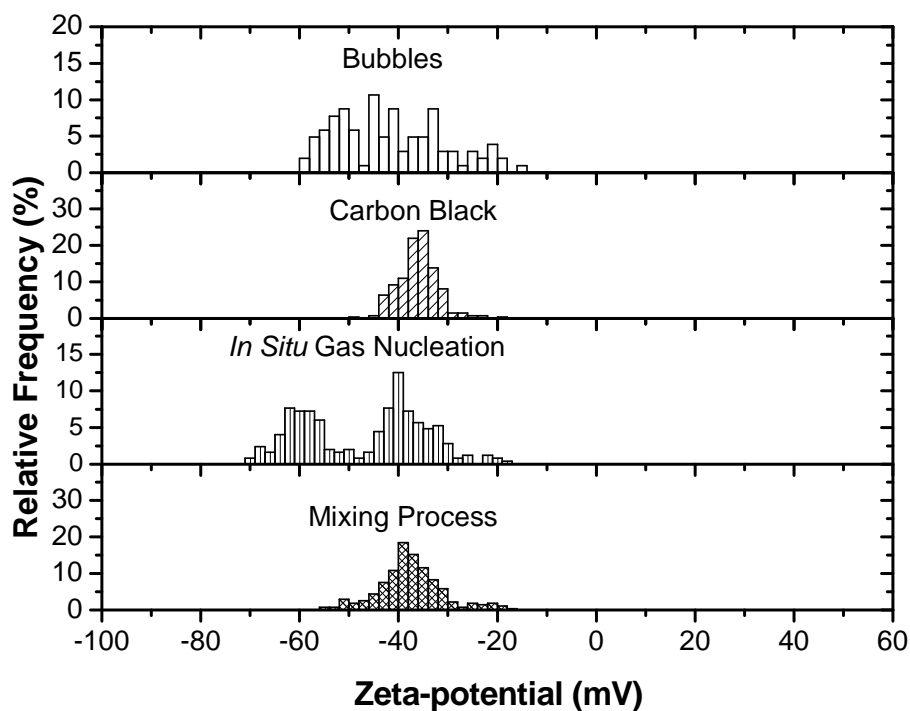
Figure AI- 2: Zeta-potential distributions of submicron size bubbles and carbon black particles in 0.1 mM DF250 + 1 mM KCl solutions at pH 8.5, measured individually or in a binary mixture.

Basing on the graphs in Figure AI- 1, at pH 6.5, both bubbles and carbon black had negative zeta-potential distributions which centered around -35mV, except that the bubble distribution was flat and wide while the carbon distribution was spiky and narrow. When the two materials were mixed together, the zeta-potential distribution of mixing process was single-peaked and looked the same as the carbon distribution. The zeta-potential distribution of *in situ* gas nucleation obviously spread through a much broader range of -54 mV ~ 0 mV, and had two peaks. The individual distributions of bubbles and carbon black were overlapping, thus it would be difficult to judge whether there was an attachment. However,

185

according to the bimodal *in situ* distribution, it is likely that there was no

attachment between bubbles and carbon black particles as the sever shear during

in situ gas nucleation helped to differentiate the mobility of the not attached

bubbles and carbon black particles. Figure AI- 2 tells a similar story when the pH

of the solution was increased to 8.5. Compared to those at pH 6.5, the bubble

distribution and carbon distribution was both more negative (peaks at around -42

mV and -37 mV respectively), and the bubble distribution was still extensive

while the carbon distribution was sharp. The zeta-potential distributions of mixing

process and *in situ* gas nucleation had almost the same appearance as those at pH

6.5 except that the two distribution peaks of the *in situ* distributions at pH 8.5

were much more outstanding. Again, such results provide us with a hint that

bubbles and carbon black did not attach to each other due to electrostatic

repulsive force. It is shown here that as the electrostatic repulsive force increased

with decreasing (more negative) zeta-potential of bubbles and carbon black, the

overlapping distribution peaks were differentiated from each other possibly as an

effect of excessive shear on bubble/particle electrophoretic mobility. However,

this was contradictory to the expectation that strong attachment would occurred

among the components as a result of strong hydrophobic force. The reason for this

contradiction probably lay in the high concentration of DF250, which was three

times its ccc, used in the experiments. It is possible here that both surfaces of

bubbles and carbon black were fully covered by DF250, thus both surfaces

changed from hydrophobic to hydrophilic. In this way, due to lack of hydrophobic

force and presence of strong electrostatic repulsion, bubble and carbon black particles would definitely not attach, which agrees with our findings here.
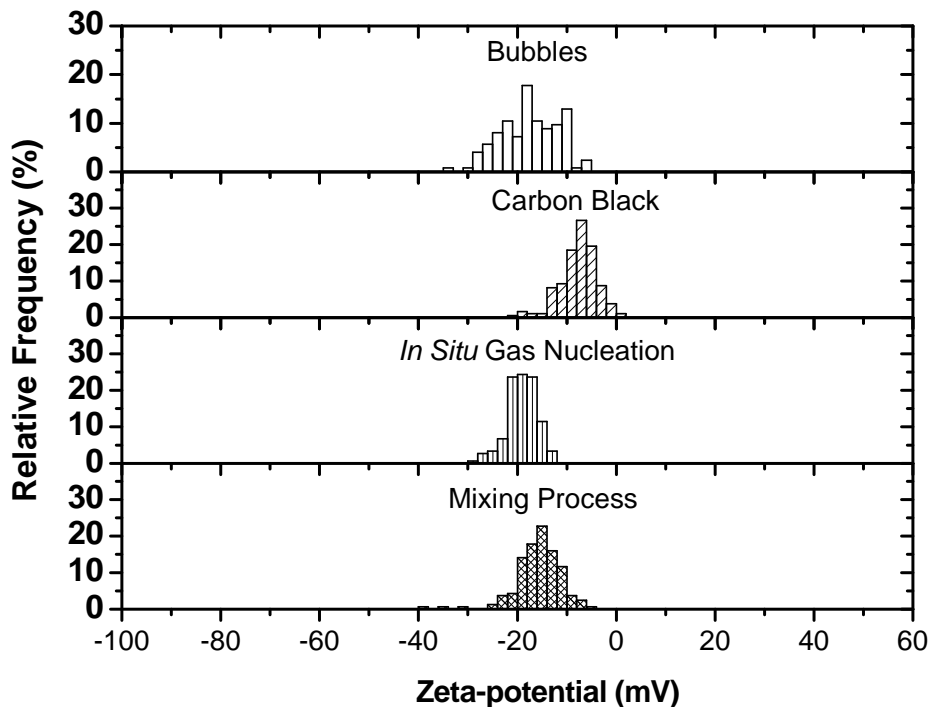

Figure AI- 3: Zeta-potential distributions of submicron size bubbles and carbon black particles in 0.1 mM DF250 + 1 mM KCl solutions at pH 4.0, measured individually or in a binary mixture.

When pH reduced to pH 4.0 (Figure AI- 3), both the bubbles and carbon black was still negatively charged but very small in magnitude (corresponding distribution peaks at -15 mV and -7 mV). In the case of pH 2.1 (Figure AI- 4), bubbles were slightly negatively charged (about -9 mV) while the charges of carbon black was reversed to becoming positive (about 16 mV). All the four interaction distributions shown in the two figures had only one and distinct peak indicating strong attachment of bubbles and carbon black particles. At pH 4.0, the

187

bubble-carbon black attachment was possibly that of an unstable colloidal system, where Van der Waals attractive force contributed to attachment of the two components when electrostatic force was not strong enough to keep them stably suspended. The strong bubble-carbon black attachment at pH 2.1 was obviously the result of electrostatic attractive force. Although results here in some way agreed with our former conclusion of the effect of electrostatic double layer force in bubble-particle interactions, cases of pH 8.5, 6.5 and 4.0 need to be further confirmed.
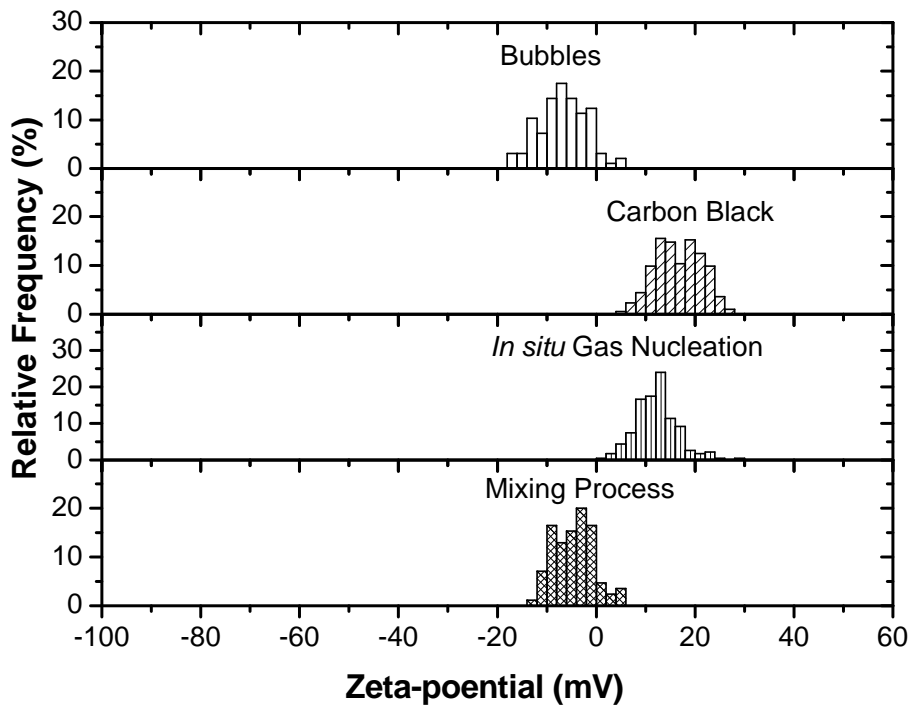

Figure AI- 4: Zeta-potential distributions of submicron size bubbles and carbon black particles in 0.1 mM DF250 + 1 mM KCl solutions at pH 2.1, measured individually or in a binary mixture.

Appendix II: Calculations

1.   Comparison of Zeta-Potential Values Calculated from the

Smoluchowski Equation and Henry's Equation

As mentioned previously in the thesis, the zeta-potential values gained

from both the Zetaphoremeter and ZetaPALS were based on the Helmholtz –

Smoluchowski equation, of which κa << 1. It is also important to point out that

Helmholtz – Smoluchowski equation is independent of particle size, and thus its

calculated values would remain stable despite the changes in the size of particles.

However, neither of these characters seems to fit our current circumstances of the

bubble-solid interaction system where κa was within an intermediate range and

particle size was not fixed. Hereby, it would be more appropriate for this study to

use Henry's solution, which meets both of our mentioned considerations, instead.

By recalculating the current zeta-potential values with Henry's solution, taking

into consideration the effect of particle size, one may expect to see a noticeable

shift in position of the zeta-potential distributions achieved earlier and thus it may

affect the applicability of the zeta-potential distribution analysis by varying the

distance between two distributions. Figure AII- 1 is a plot of the actual

zeta-potential values calculated by using the Helmholtz – Smoluchowski equation

and Henry's solution as a function of particle size. The inequality of the resulting

values form the two equations shown here would indicate how big a shift we

would expect in the distribution positions. The mobility used to plot Figure AII- 1

189

was fixed to be -3 μm/s/v/cm and viscosity of water was used here as the viscosity

of the media.
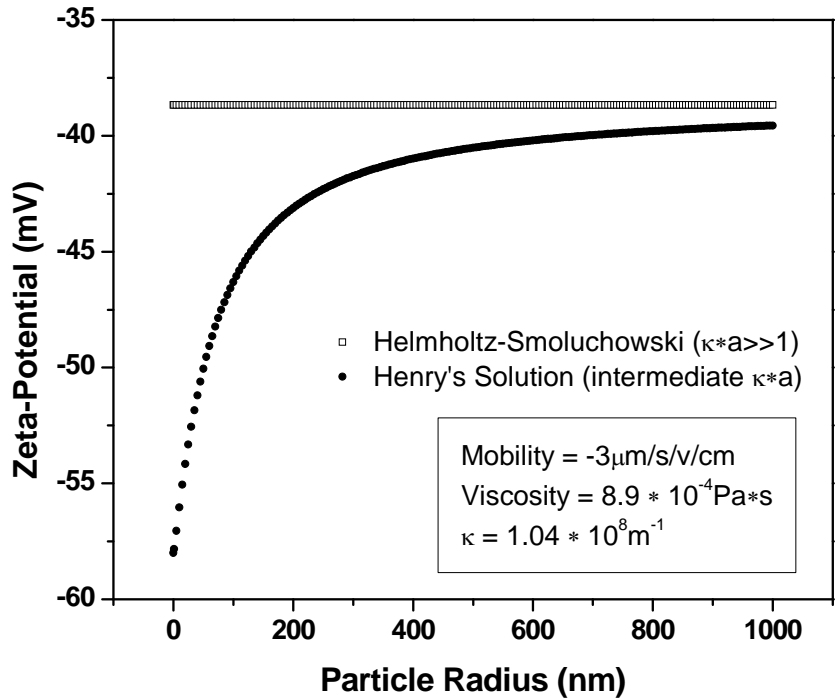
Figure AII- 1: Effect of particle size on zeta-potential calculated by Helmholtz –

Smoluchowski Equation and Henry's Solution at a constant electrophoretic

mobility of -3 μm/s/v/cm

Shown in the figure, the calculated zeta-potential values stayed constantly

at -38.6 mV when applying Helmholtz-Smoluchowski equation, but when using

Henry's solution the zeta-potential values declined increasingly with a decrease in

the particle radius (size). When the particle radius was 1000 nm, Henry's solution

provided us with a value of -39.6 mV which is pretty much the same as that of

Helmholtz – Smoluchowski equation; but when it comes to the size of the

submicron size bubbles and nano size alumina and silica particles whose radius

was about 200 nm ~ 300 nm, a larger difference was observed between the given values by the two different equations where Henry's solution had a values between -43.1 mV ~ -41.7 mV. Thus, it is quite obvious that when referring to a system containing particles of much smaller size, the effect of the size on the zeta-potential values, and hence the interaction energy should be considered and taken into account. And for the case of our study, in most experiments, the size of bubbles and nano particles were almost the same and thus the shift would be counterbalanced. When the materials were mixed together, if aggregation was to occur, the aggregates tent to be larger but not significantly, and therefore the mixture distribution, compared with those of the bubbles and nano particles, tend to be several mV off position. Since none of the substances studied in this work was at a different size range (>> 1 micron), the discrepancy brought in by using different equations is relatively small, regardless of which the zeta-potential distribution analysis remains reliable and, by the large, accurate.

2.   Computational Prediction of the Interaction Energy

The DLVO theory was developed to define the stability of a colloidal system where the Van der Waals forces and electrostatic double layer force are predominant. However, this is never the case in the real world where beside the Van der Waals forces and electrostatic forces, other forces such as hydration forces, hydrophobic forces and steric forces also play a role in influencing the particle interaction. And therefore was the concept of extended DLVO theory, which is a more comprehensive extension of the classic DLVO theory.

According to our current study of the zeta-potential distribution analysis of the bubble-solid interaction system, we believe that besides the Van der Waals forces which could not be measured by this technique but generally admitted and well understood[76, 77, 165], the dominant force governing bubble-solid interactions at this submicron or nano scale is the electrostatic double layer force while the hydrophobic forces tend to play a very supportive role. Energy profiles (Figure AII- 2 ~ Figure AII- 4) for demonstrating the interaction forces in 0.1 mM DF250 + 1 mM KCl solutions at pH 6.5, pH 11.0 and pH 2.1 were made based on previous experimental data of bubble and particle zeta-potentials and fair assumption of the bubble and particle hydrophobicity parameters on account of former researches of bubble-solid interactions to compare with our results of the zeta-potential distribution analysis. Since we lack parameters for the regarding analytical calculation of the hydration forces and steric forces, only the Van der Waals energy (V_A), electrostatic potential energy (V_E) and hydrophobic energy (V_H) were included in the interaction energy calculations in this study. The total interaction energy V_T is given by:

$$V_T = V_A + V_E + V_H \tag{A2.1}$$

The Van der Waals energy between submicron size bubbles and solid particles was calculated by using Eq. (A2.1) for two macroscopic spherical bodies:

$$V_A = -\frac{A}{6h}\frac{R_1 R_2}{R_1 + R_2} \tag{A2.2}$$

where A is the Hamaker constant of the interaction between bubbles and solid particles immersed in DF250 solutions, h is the shortest separation distance

between the bubble and solid surfaces, while R_1 and R_2 are the radii of bubbles and solid particles, respectively.

When calculating the electrostatic potential energy, in order to accommodate the situation of constant potential and constant charge as well as to approach a more realistic condition, an electrostatic potential energy for the mixed case was hereby applied and expressed as follow[169],

$$V_E = \frac{\varepsilon R_1 R_2}{4(R_1 + R_2)} \left\{ 2\psi_1 \psi_2 \left(\frac{\pi}{2} - \tan^{-1} \sinh \kappa h \right) - \left(\psi_2^2 - \psi_1^2 \right) \ln[1 + \exp(-2\kappa h)] \right\} \quad \text{(A2.3)}$$

The Ψ_1 and Ψ_2 here stands for the surface potential of bubbles and solid particles which are approximated by the zeta-potential of the two materials, ζ_1 and ζ_2, ε stands for the dielectric constant of the medium, κ stands for the Debye constant and h again stands for the closest separation distance between the two spheres.

The hydrophobic energy is the most difficult to calculate as well as the most argumentative among the three energies in consideration. Massive effort has been devoted to the issue by former researchers[170, 184]. One approach to analytically calculate hydrophobic energy (V_H) is Eq. (A2.4)[45] provided as follow,

$$V_H = -\frac{R_1 R_2}{6(R_1 + R_2)} \frac{K_{132}}{h} \quad \text{(A2.4)}$$

The only parameter left to be figured out in Eq. (A2.4) is K_{132}, the hydrophobic constant of a hydrophobic interaction between two macroscopic spheres 1 and 2 in a medium 3. K_{132} is generally difficult to be determined experimentally[45], but normally known as a function of the contact angles of the two surfaces θ_1 and θ_2 and described as[77]:

$$K_{132} = -\exp\left(a\frac{\cos\theta_1 + \cos\theta_2}{2} + b\right)$$ (A2.5)

where a and b were obtained from the best fit to experimental data as $a = -7.0$ and

$b = -18.0$ when the force constant is expressed in joules. When the case comes to

a symmetric interaction between two solid surfaces of the same hydrophobicity,

K_{131} is obtained by setting $\theta_1 = \theta_2 = \theta$, yielding

$$K_{131} = -\exp(a\cos\theta + b)$$ (A2.6)

However, it is unlikely that K_{131} can be used as a direct substitute for K_{132},

especially when applying to bubble-particle interactions[45]. But on the other hand

it is still highly likely that some kind of relation ship might lie between the two

parameters,

$$K_{132} = fK_{131}$$ (A2.7)

where f is a multiplication factor larger than 1 and is dependent of particle

hydrophobicity and the amount of surfactant in the system[45]. The multiplication

factor f can be acquired via a back-calculated process and various experimental

data generated by Yoon and his coworkers[45]. It was also found in their work that

for the fact of bubbles being much more hydrophobic than most solid particles,

the K_{132} values are approximately two orders of magnitudes larger than those of

K_{131}, and a probable value for f is around 30 for bubble-particle interaction in

solutions of low surfactant concentration[45]. For our purpose of simulating the

energy profile of bubble-particle interactions in 0.1 mM DF250 + 1 mM KCl

solutions, Eq. (A2.6) was used to calculated the K_{131} of solid particles by applying

rough values of the contact angles of alumina, silica and carbon black which are

respectively 20º, 20º and 75º, basing on reported laboratorial data and fair assumptions[210, 211]. In subsequence, K_{132} was gained from Eq. (A2.7) by fixing $f = 30^{45}$, and finally Eq. (A2.4) was used for estimating the V_H value.

*2.1   Energy Profile of Bubble-Alumina Interactions in 0.1 mM DF250 + 1 mM KCl Solutions*
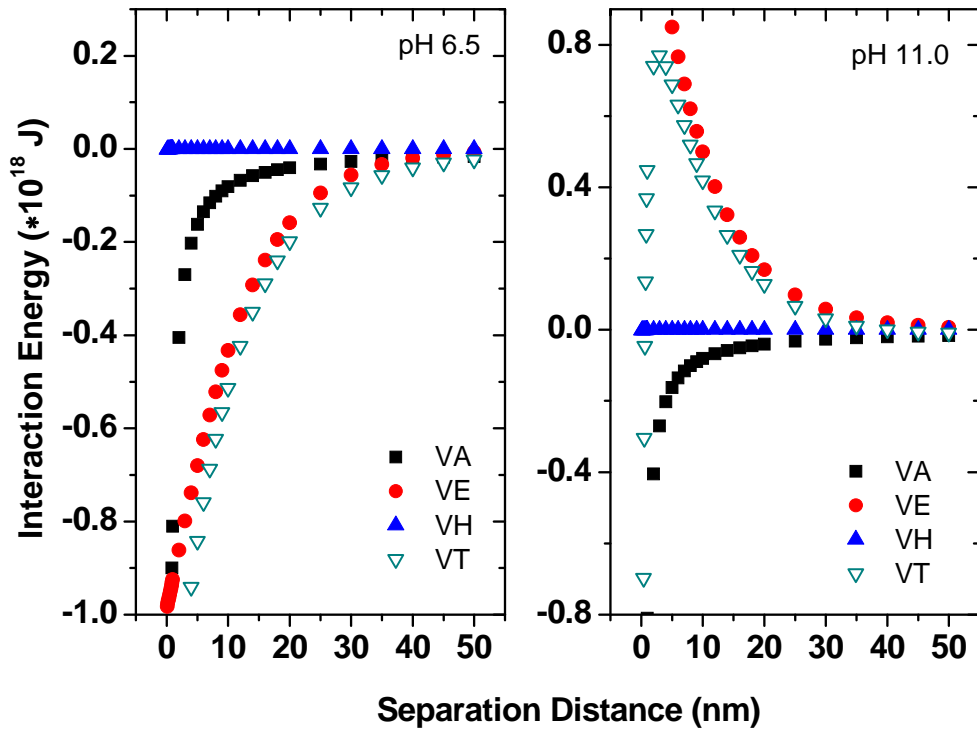
Figure AII- 2: XDLVO energies calculated for bubble-alumina interactions in 0.1 mM DF250 + 1 mM KCl at pH 6.5 and pH 11.0 using Rb = 200 nm, Ra = 300 nm, ζb = -36.0 mV and ζa = 34.3 mV at pH 6.5, ζb = -50.9 mV and ζa = -24.4 mV at pH 11.0, $\theta = 20º$, $\kappa = 1.04 \times 10^8$, $k_{132} = 7.9 \times 10^{-24}$ J, $A_{132} = 4.05 \times 10^{-20}$ J.

Given in Figure AII- 2, in 0.1mM DF250 + 1mM KCl solutions at pH 6.5 where the zeta-potential of alumina was positive and the zeta-potential of bubbles was negative, both the Van der Waals energy (V_A) and electrostatic potential energy (V_E) turned out to be attractive while the repulsive energy due to hydrophobic force (V_H) was almost ignorable. Therefore, the total energy (V_T) by summing up the three individual energies was shown to be strongly attractive with no energy barrier at all. At pH 11.0, as the zeta-potential of alumina reversed from positive to negative, V_E also reversed from attractive to repulsive due to surface charge of like signs and relatively large magnitude. V_A and V_H, in this case, remained their former state, both attractive and yet V_H barely effective. So as a result, a huge energy barrier was revealed in V_T, suggesting no attachment of bubbles with alumina particles unless the enormous barrier was overcome by other supporting exterior energies of some kind. Here, results of the energy profile agree perfectly with our former results of zeta-potential distribution analysis, confirming the more dominant role of the electrostatic double layer force when both V_E and V_H are present.

2.2 *Energy Profile of Bubble-Silica Interactions in 0.1 mM DF250 + 1 mM KCl Solutions*

The energy profiles of bubble-silica interactions in the same DF250 solution at pH 6.5 and pH 2.1 are shown in Figure AII- 3. At both pHs, V_A was attractive and V_H again was hardly influential; V_E was always repulsive except that repulsion was much stronger at pH 6.5 where the zeta-potential values of both the bubbles and silica particles were very negative. The resulting V_T at pH 6.5

possessed an energy barrier, but that at pH 2.1 was purely attractive. Recalling the zeta-potential distributions of bubble-silica interactions in the same environment—the mixing and *in situ* distributions at pH 6.5 showed a repelling behaviour of the individual bubbles and silica particles while the mixture distributions at pH 2.1 presented adhesive interaction among the two substances regardless of their uni-sign charges, which was possibly the result of the instability of the electrostatic double layer force and energies involved in nano bubble precipitation on rough solid surfaces during the *in situ* gas nucleation. The energy profiles in Figure AII- 3 tend to tell the exact same story where the electrostatic energy or electrostatic double layer forces take full control of the interaction process when it was so strong that no other forces was competitive; and once the repulsive electrostatic forces was crippled and unstabilized due to decrease in the charge density at bubble and particle surfaces, impact of other forces (or energies) on the interaction become evident. The profile also explains why attachment of bubbles and silica was more distinct during *in situ* gas nucleation, as during such an *in situ* process energies involved are much more complicated and most of which tend to make V_T more adhesive.
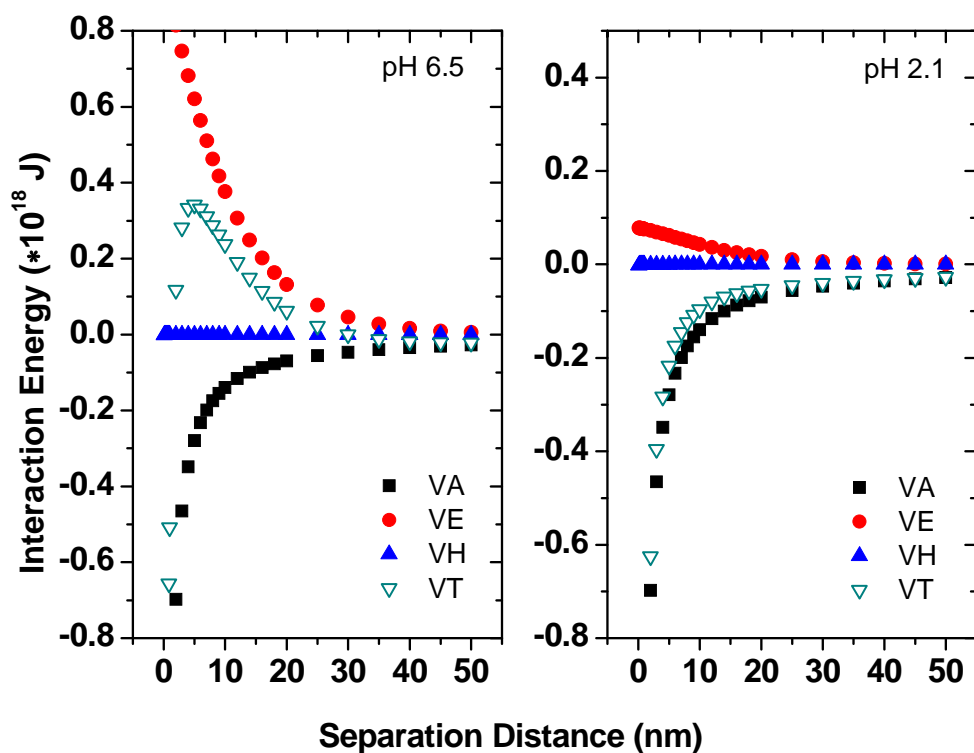
Figure AII- 3: XDLVO energies calculated for bubble-silica interactions in 0.1 mM DF250 + 1 mM KCl at pH 6.5 and pH 2.1 using Rb = 200 nm, Rs = 300 nm, ζb = -38.5 mV and ζs = -25.9 mV at pH 6.5, ζb = -8.5 mV and ζs = -16.3 mV at pH 2.1, θ = 20º, κ = 1.04×10^8, k_{132} = 7.9×10^{-24} J, A_{132} = 6.98×10^{-20} J.

2.3   *Energy Profile of Bubble-Carbon Black Interactions in 0.1 mM DF250 + 1 mM KCl Solutions*

For both cases shown in Figure AII- 2 and Figure AII- 3, the hydrophobicity of alumina and silica was extraordinarily low, so the hydrophobic force was barely noticeable not to say of great significance. But if the hydrophobicity of the solid particles were to increase to a certain extent, then it is

anticipated that it would have critical impact on bubble-particle interactions. Carbon black (Sigma-Aldrich) was observed to be highly hydrophobic and the estimated contact angle was set to be75º for calculation. The energy profiles shown in Figure AII- 4 proved that the increase in the hydrophobicity of the particle led to an increase in the magnitude of V_H as it increased form almost 0 to apparently attractive. Even though at both pH 6.5 and pH 2.1 the repulsive electrostatic potential energy was obvious, the hydrophobic energy was not only able to conquer the effect but define the total interaction energy as attractive. These results show high compatibility with what was proven by the zeta-potential distribution analysis as well, as shown in both methods, bubbles and carbon black particles tend to come close to one another and form aggregates. However, the only unexpected uncertainty was the case of *in situ* gas nucleation at pH 6.5 where the distribution was magnificently broad and scattered. This was formerly explained by the demolishment of the bubble-carbon black attachment by severe hydrodynamic shear force as a result of unknown modification of the bubble and carbon black surfaces at a higher frother relative concentration. Nevertheless, direct evidence is to be found as to support the assumption and make the ground firm.
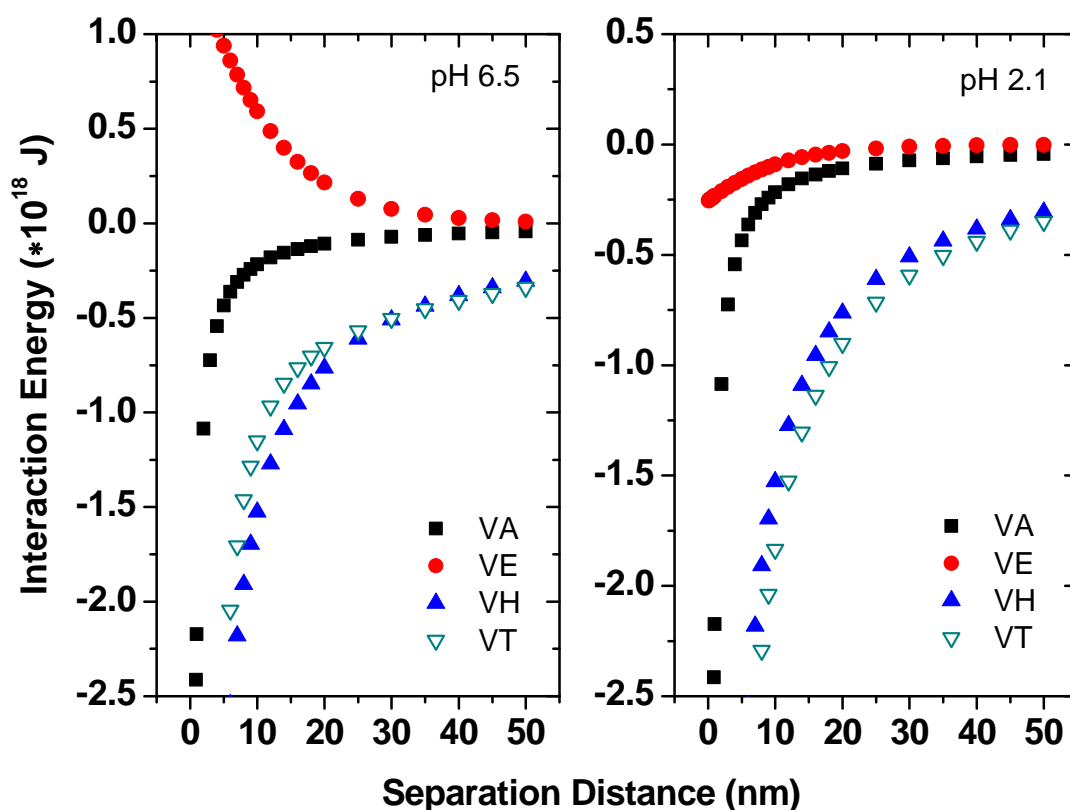
Figure AII- 4: XDLVO energies calculated for bubble-carbon black interaction in 0.1 mM DF250 + 1 mM KCl at pH 6.5 and pH 2.1 using $Rb = Rc = 200$ nm, $\zeta b = -32.1$ mV and $\zeta c = -31.2$ mV at pH 6.5, $\zeta b = -7.6$ mV and $\zeta c = 17.5$ mV at pH 2.1, $\theta = 75°$, $\kappa = 1.04 \times 10^8$, $k_{132} = 4.58 \times 10^{-19}$ J, $A_{132} = 6.52 \times 10^{-20}$ J.

All in all, the energy profiles showed great consistency with the zeta-potential distribution analysis results, and thus the efficiency and preciseness of the zeta-potential distribution analysis technique was assured, and the role of electrostatic force and hydrophobic force on bubble-particle interactions tend to be more trenchant and understandable as described in this study.